

1-1-2018

# From anionic porous organic frameworks with phosphate functional groups to a mesoporous aluminosilica material with crystalline pore walls

Yiqun Liu

Lehigh University, yiqunliu0714@gmail.com

Follow this and additional works at: <https://preserve.lehigh.edu/etd>

 Part of the [Organic Chemistry Commons](#)

---

## Recommended Citation

Liu, Yiqun, "From anionic porous organic frameworks with phosphate functional groups to a mesoporous aluminosilica material with crystalline pore walls" (2018). *Theses and Dissertations*. 4303.  
<https://preserve.lehigh.edu/etd/4303>

This Dissertation is brought to you for free and open access by Lehigh Preserve. It has been accepted for inclusion in Theses and Dissertations by an authorized administrator of Lehigh Preserve. For more information, please contact [preserve@lehigh.edu](mailto:preserve@lehigh.edu).

From anionic porous organic frameworks with phosphate  
functional groups to a mesoporous aluminosilica material with  
crystalline pore walls

by

Yiqun Liu

A Dissertation

Presented to the Graduate and Research Committee

of Lehigh University

in Candidacy for the Degree of

Doctor of Philosophy

in

Chemistry

Lehigh University

Jan. 2018

© 2018 Copyright  
Yiqun Liu

Approved and recommended for acceptance as a dissertation in partial fulfillment of the requirements for the degree of Doctor of Philosophy

Yiqun Liu

From anionic porous organic frameworks with phosphate functional groups to a mesoporous aluminosilica material with crystalline pore walls

---

Defense Date

---

Approved Date

---

Dissertation Director  
Dr. Kai Landskron

Committee Members:

---

Dr. David Vacic

---

Dr. James Roberts

---

Dr. H. Daniel Ou-Yang

## ACKNOWLEDGMENTS

The path towards this dissertation has been circuitous. The completion of this dissertation thanks to all the people who helped me, supported me, challenged me, and entertained me alongside the way.

First and foremost, I would like to express my appreciation to my dear advisor Professor Kai Landskron, for his knowledge, guidance, and constructive suggestions during my studies at Lehigh. Without his guidance and exceptionally helpful comments, this dissertation would not have been possible.

The members in my group have contributed tremendously to my personal and professional time at Lehigh. Dr. Cong Liu, Dr. Berenika Kokoszka, Dr. Manik Mandal, Dr. Damian Paliwoda and Dr. Shan Zhu are wonderful friends and teachers in my research and life. I am especially grateful for the friendship we built as well as good advice and collaboration during my stay at Lehigh.

I would like to give my special thanks to Prof. James Roberts, not only for his guidance and inspiration in academic research, but also for his suggestions in my life and career. I would also like to thank my committee members, Professor Daniel Ouyang and Prof. Dave Vicic for serving in my committee, for letting my defense be an enjoyable moment, and for their wise and beneficial comments and suggestions.

My time at Lehigh was pleasant and memorable in large part due to the friends that have become a part of my life. I am grateful for the time spent with many friends in the wild, on the basketball court, in the restaurants, and in their homes, drunk and sober. I will never forget those moments. I would like to thank LeBron James, for always giving me power, even at hard times.

At last, the most special and deepest thanks to my lovely family. I would like to thank them for their love and encouragement. For my parents who raised me with knowledge and supported me in all my pursuits. For my elder brother who looked after my back so that I never need to worry about anything in the family. For my dearest wife, Yue Li, who faithfully supported and accompanied me in the brightest sunlight and darkest night. Without you, I am not who I am. Thank you.

Yiqun Liu

12/02/2017

# Table of Contents

List of Figures.....	vii
List of Tables.....	xii
Abstract.....	1
1 Introduction.....	2
1.1 Overview of porous materials .....	2
1.2 Synthesis of porous organic frameworks .....	9
1.2.1 Synthetic methodology of porous organic frameworks .....	9
1.2.2 Synthesis of weakly coordinating anionic porous organic frameworks .....	16
1.3 Synthesis of mesoporous silica materials.....	20
1.3.1 Synthesis of mesoporous silica materials.....	20
1.3.2 Synthesis of mesoporous aluminosilica materials.....	23
1.3.3 Synthesis of mesoporous aluminosilica materials with crystalline pore channel walls .....	26
1.4 References .....	28
2 Synthesis of anionic porous organic frameworks with phosphate functional groups (PA-POFs) .....	33
2.1 Design of phosphorus-based anionic porous organic frameworks.....	33
2.2 Synthesis of TTBP and LTBP.....	39
2.3 Synthesis of P-WCA-POFs and PA-POFs.....	43
2.4 Characterization of PA-POFs.....	62
2.5 References .....	73
3 CO <sub>2</sub> adsorption properties of PA-POFs .....	74
3.1 Introduction.....	74
3.2 CO <sub>2</sub> adsorption properties of PA-POFs.....	78
3.3 References .....	83
4 Rapid adsorption of organic pollutants from water by PA-POFs.....	85
4.1 Introduction.....	85
4.2 Methods and materials.....	87

4.3	Adsorption of bisphenol A from water by PA-POFs.....	88
4.4	Adsorption of various organic micropollutants from water by PA-POFs....	102
4.5	Summary and discussion.....	105
4.6	References.....	108
5	Synthesis of a periodic mesoporous crystalline aluminosilicate material.....	110
5.1	Experimental methods and procedures .....	111
5.1.1	Materials and methods.....	111
5.1.2	Synthesis of mesoporous aluminosilica material (Al-SBA-15).....	112
5.1.3	Li induced crystallization of Al-SBA-15.....	113
5.2	Results and Discussions.....	114
5.2.1	Characterization of mesoporous aluminosilica material (Al-SBA-15) .....	114
5.2.2	Characterization of lithium aluminosilicate (LAS) .....	116
5.2.3	Treatment of LAS in acids.....	127
5.2.4	Acidity study of LAS material.....	133
5.3	Conclusions.....	137
5.4	References.....	138
	VITA.....	139

# List of Figures

Figure 1-1. Examples of porous materials. (a) zeolite, (b) mesoporous silica, (c) nanoporous carbon, (d) metal-organic framework (MOF), (e) covalent organic framework (COF), and (f) porous organic framework (POF).....	4
Figure 1-2. Synthesis scheme of a PAF-1 with ultrahigh surface area by the Yamamoto-type Ullmann cross-coupling reaction. Ref. 27.....	10
Figure 1-3. Representative molecular structures for CMP-0 to CMP-5. Ref. 42.....	14
Figure 1-4. (a) N <sub>2</sub> adsorption-desorption isotherms measured at 77.3 K. For clarity, the isotherms of CMP-0, CMP-1, CMP-2, and CMP-3 were shifted vertically by 400, 300, 200, and 100 cm <sup>3</sup> g <sup>-1</sup> , respectively. (b) NL-DFT pore size distribution curves. (c) Cumulative pore volume curves calculated by application of NL-DFT. Ref. 42.....	15
Figure 1-5. Synthesis of ICOF-1 and ICOF-2. Ref. 52.....	18
Figure 1-6. Synthesis of Li-ABN. Ref. 50.....	19
Figure 1-7. Schematic synthesis pathways of self-assembly of surfactant for the formation of MCM-41: (a) liquid crystal phase initiated, and (b) silicate initiated. Ref. 55. ....	21
Figure 1-8. Phase sequence of surfactant-water binary system. CMC = critical micellization concentration. Ref. 56.....	22
Figure 1-9. Preparation of a single-crystalline mesoporous quartz superlattice by crystallization of amorphous silica, which constitutes a colloidal crystal, by using a Li <sup>+</sup> flux and a reinforcing carbon framework. Ref. 85.....	27
Figure 2-1. Selection of hexacoordinated phosphate anions. Ref. 4–12.....	34
Figure 2-2. Schematic synthesis of hexacoordinated phosphorus species. A <sup>+</sup> represents the cation to balance the negative charge on the WCA.....	35
Figure 2-3. Proposed synthesis of 1,2,4,5-tetrahydroxy benzene and PCl <sub>5</sub> for the construction of a two-dimensional porous framework.....	36
Figure 2-4. Representative N <sub>2</sub> sorption isotherm of the products from the reaction between 1,2,4,5-tetrahydroxy benzene and PCl <sub>5</sub> .....	37
Figure 2-5. Representative <sup>31</sup> P solid state NMR spectrum of the products from the reaction between 1,2,4,5-tetrahydroxy benzene and PCl <sub>5</sub> .....	38
Figure 2-6. Synthesis scheme of TTBP and LTBP.....	39
Figure 2-7. <sup>1</sup> H NMR spectrum of TTBP.....	41
Figure 2-8. <sup>13</sup> C NMR spectrum of TTBP.....	41
Figure 2-9. <sup>31</sup> P NMR spectrum of TTBP.....	42
Figure 2-10. <sup>7</sup> Li NMR spectrum of LTBP.....	42



Figure 2-11. $^{31}\text{P}$ NMR spectrum of LTBP.....	43
Figure 2-12. $^{31}\text{P}$ solid state NMR spectrum of polymerized TTBP. Asterisks (*) indicate peaks arising from spinning side bands.....	44
Figure 2-13. Nitrogen adsorption (red squares) and desorption (black squares) isotherms of polymerized TTBP measured at 77K.....	45
Figure 2-14. EDX spectrum of polymerized TTBP after ion exchange in NaCl solution. No Na can be found in the EDX spectrum shows that the cation was not exchangeable.....	45
Figure 2-15. Synthesis of P-WCA-POFs and PA-POFs through Ni-promoted Yamamoto coupling reactions.....	46
Figure 2-16. Nitrogen adsorption (red squares) and desorption (black squares) isotherms of P-WCA-POF-1 [1:1] measured at 77K.....	47
Figure 2-17. $^{31}\text{P}$ solid state NMR spectrum of P-WCA-POF-1 [1:1]. Asterisks (*) indicate peaks arising from spinning side bands.....	48
Figure 2-18. EDX spectrum of P-WCA-POF-1 [1:1].....	48
Figure 2-19. EDX spectrum of P-WCA-POF-1 [1:1] after treatment of concentrated HCl.....	49
Figure 2-20. $^{31}\text{P}$ solid state NMR spectrum of PA-POF-1s. Asterisks (*) indicate peaks arising from spinning side bands.....	49
Figure 2-21. Nitrogen sorption isotherms of PA-POF-1s. The curves are offset for better visualization.....	50
Figure 2-22. EDX spectrum of PA-POF-1s after ion exchange in NaCl solution.....	51
Figure 2-23. $^{31}\text{P}$ solid state NMR spectrum of P-WCA-POF-2 [1:1]. Asterisks (*) indicate peaks arising from spinning side bands.....	53
Figure 2-24. Nitrogen adsorption (red squares) and desorption (black squares) isotherms of P-WCA-POF-2 [1:1] measured at 77K.....	53
Figure 2-25. EDX spectrum of P-WCA-POF-2 [1:1] after ion exchange in NaCl solution. No Na can be found in the EDX spectrum shows that the cation was not exchangeable.....	54
Figure 2-26. EDX spectrum of P-WCA-POF-2 [1:1] after treatment of concentrated HCl. ....	55
Figure 2-27. $^{31}\text{P}$ solid state NMR spectrum of PA-POF-2s.....	56
Figure 2-28. Nitrogen sorption isotherms of PA-POF-2s.....	57
Figure 2-29. EDX spectrum of PA-POF-2s after ion exchange in NaCl solution.....	58
Figure 2-30. SEM images of PA-POF-1s. A: PA-POF-1 [1:1]; B: PA-POF-1 [0.6:1]; C: PA-POF-1 [0.3:1].....	65

Figure 2-31. SEM images of PA-POF-2s. (A) PA-POF-2 [2:1]; (B) PA-POF-2 [1:1]; (C) PA-POF-2 [0.8:1]; (D) PA-POF-2 [0.6:1]; (E) PA-POF-2 [0.4:1]; and (F) PA-POF-2 [0.2:1].....	66
Figure 2-32. XRD patterns of PA-POF-1s and PA-POF-2s. Patterns are offset for clarification.....	67
Figure 2-33. (A) PA-POF-1s and (B) PA-POF-2s thermograms measured in air.....	68
Figure 2-34. (A) PA-POF-1s and (B) PA-POF-2s thermograms measured in nitrogen.....	69
Figure 2-35: FTIR spectra of (A) PA-POF-1s and (B) PA-POF-2s. The FTIR spectrum of PAF-1 was inserted in each figure for comparison. Spectra are labeled by compound names. Because of the low content of phosphorus, P-O stretching is not obvious in the spectra.....	70
Figure 2-36. Pore size distribution of (a) PA-POF-1s and (b) PA-POF-2s calculated from CO <sub>2</sub> sorption isotherms collected at 273 K by NLDFT method (carbon slit pore model).....	71
Figure 3-1. Global greenhouse gas emission sources in 2004. Ref. 5.....	75
Figure 3-2. Projected growth in CO <sub>2</sub> emissions until 2040 by U.S. Energy Information Administration. Ref. 7.....	78
Figure 3-3. CO <sub>2</sub> adsorption isotherms of PA-POF-1s at (a) 258 K, (b) 273 K, and (c) 298 K; CO <sub>2</sub> adsorption isotherms of PA-POF-2s at (d) 258 K, (e) 273 K, and (f) 298 K.....	81
Figure 3-4. (A) CO <sub>2</sub> uptakes at 273K and 1 bar and (B) isosteric heats of CO <sub>2</sub> adsorption (Q <sub>st</sub> ) of PAFs. Ref. 10.....	82
Figure 3-5. Isosteric heats of CO <sub>2</sub> adsorption (Q <sub>st</sub> ) of (a) PA-POF-1s and (b) PA-POF-2s.....	83
Figure 4-1. Time dependent adsorption of 0.1 mM aqueous bisphenol A (1 mL mg <sup>-1</sup> ) by each adsorbent. P-CDP: porous β-cyclodextrin polymer (S <sub>BET</sub> = 263 m <sup>2</sup> g <sup>-1</sup> ); NP-CDP: nonporous β-cyclodextrin polymer (S <sub>BET</sub> = 6 m <sup>2</sup> g <sup>-1</sup> ); EPI-CDP: a non-porous β-cyclodextrin polymer crosslinked with epichlorohydrin (S <sub>BET</sub> = 23 m <sup>2</sup> g <sup>-1</sup> ); NAC: Norit RO 0.8 activated carbon (S <sub>BET</sub> = 984 m <sup>2</sup> g <sup>-1</sup> ); GAC: DARCO granular activated carbon (S <sub>BET</sub> = 612 m <sup>2</sup> g <sup>-1</sup> ); Brita AC: the hybrid AC/ion exchange resin used in commercial Brita point-of-use filters (S <sub>BET</sub> = 507 m <sup>2</sup> g <sup>-1</sup> ). Ref. 11.....	87
Figure 4-2. UV-vis spectra of BPA solutions after 100 mL mg <sup>-1</sup> adsorption studies for one hour by PA-POFs and PAF-1.....	90
Figure 4-3. Bisphenol A removal efficiency of PA-POFs and PAF-1 from 100 mL mg <sup>-1</sup> 0.1 mM BPA solution.....	90
Figure 4-4. UV-vis spectra of BPA solutions after 40-140 mL mg <sup>-1</sup> adsorption studies for one hour by PA-POF-2 [0.8:1].....	91

Figure 4-5. Bisphenol A removal efficiency of PA-POF-2 [0.8:1] from 40-140 mL mg <sup>-1</sup> 0.1 mM BPA solution.....	92
Figure 4-6. Langmuir (red) and Freundlich (blue) adsorption isotherms of BPA by PA-POF-2 [0.8:1].....	94
Figure 4-7. UV-vis spectra of the filtrates as a function of contact times for PA-POF-2 [0.8:1].....	96
Figure 4-8. Effect of contact time on the adsorption of 10 mL mg <sup>-1</sup> BPA by PA-POF-2 [0.8:1] and Brita AC.....	97
Figure 4-9. Pseudo-second-order plot of the PA-POF-2 [0.8:1] kinetics study ( $q_e = 222 \text{ mg g}^{-1}$ , $k_{\text{obs}} = 0.15 \text{ g mg}^{-1} \text{ min}^{-1}$ ).....	98
Figure 4-10. The average percentage BPA removal efficiency by PA-POF-2 [0.8:1] and Brita AC after regeneration cycles.....	99
Figure 4-11. The UV-vis spectra of the filtrate after adsorption and the redissolved BPA solution recovered by extraction with MeOH.....	101
Figure 4-12. UV-vis spectra recorded at different contact time and time dependent removal efficiency of 10 mL mg <sup>-1</sup> (a) 0.1 mM 2-naphthol, (b) 0.1 mM 1-naphthyl amine, and (c) 0.1 mM bisphenol S.....	103
Figure 4-13. UV-vis spectra recorded at different contact time and time dependent removal efficiency of 10 mL mg <sup>-1</sup> (a) 0.09 mM propranolol hydrochloride, (b) 0.1 mM metolachlor, (c) 0.04 mM ethinyl oestradiol, and (d) 0.1 mM 2,4-dichlorophenol.....	104
Figure 5-1. Nitrogen adsorption isotherm of Al-SBA-15.....	114
Figure 5-2. Pore size distribution of Al-SBA-15 calculated by BJH method from the adsorption branch.....	115
Figure 5-3. Top: TEM image of Al-SBA-15 (inset shows corresponding SAED pattern collected from the encircled area). Bottom: EDS spectrum of Al-SBA-15.....	116
Figure 5-4. XRD pattern of as-synthesized LAS material, compared with hexagonal spodumene, Li <sub>2</sub> SiO <sub>3</sub> , and Li <sub>4</sub> SiO <sub>4</sub> .....	118
Figure 5-5. Quantitative analysis (WPPF method) of as-synthesized LAS material. Relative percentages of crystalline phases are shown in the upper-right corner. The blue line is the original pattern; the red line is the calculated pattern using crystal information from JCPDS cards listed in the graph; the purple line in the lower box shows the errors.....	119
Figure 5-6. Nitrogen adsorption isotherm of as-synthesized LAS material.....	121
Figure 5-7. BJH pore size distribution of as-synthesized LAS calculated from the adsorption branch.....	121
Figure 5-8. SAXS patterns of Al-SBA-15 and as-synthesized LAS material.....	122
Figure 5-9. TEM image of as-synthesized LAS (inset shows corresponding SAED pattern collected from the encircled area).....	122

Figure 5-10. $^{29}\text{Si}$ solid state NMR spectra of Al-SBA-15 and as-synthesized LAS.....	124
Figure 5-11. $^{27}\text{Al}$ solid state NMR spectra of Al-SBA-15 and as-synthesized LAS.....	125
Figure 5-12. $^7\text{Li}$ solid state NMR spectrum of as-synthesized LAS.....	126
Figure 5-13. Raman spectrum of as-synthesized LAS material.....	126
Figure 5-14. Rietveld refinement plot of LAS-HCl. The blue line is the original pattern; the red line is the calculated pattern using crystal information from JCPDS cards listed in the graph; the purple line in the lower box shows the errors. The $R_{\text{wp}}$ value for the refinement is shown in the upper right corner.....	128
Figure 5-15. Nitrogen adsorption isotherm of the acid treated material, LAS-HCl.....	129
Figure 5-16. BJH pore size distribution of LAS-HCl calculated from the adsorption branch.....	129
Figure 5-17. SAXS patterns of LAS-HCl as compared with Al-SBA-15 and as-synthesized LAS material.....	130
Figure 5-18. TEM image of LAS-HCl (inset shows corresponding SAED pattern collected from the encircled area).....	130
Figure 5-19. $^{27}\text{Al}$ solid state NMR spectra of LAS-HCl in comparison with Al-SBA-15 and as-synthesized LAS.....	131
Figure 5-20. Nitrogen adsorption isotherm of LAS-H <sub>2</sub> SO <sub>4</sub> .....	132
Figure 5-21. TEM image of LAS-H <sub>2</sub> SO <sub>4</sub> .....	133
Figure 5-22. Ammonia TPD of LAS-NH <sub>4</sub> .....	135
Figure 5-23. EDS spectrum of LAS-Na.....	136

## List of Tables

Table 1-1. Summary of Representative Chemical Reactions for the synthesis of POF.....	11
Table 2-1. Summary of apparent BET surface area and pore volume of PA-POFs.....	72
Table 3-1. Summary of BET surface areas, pore volumes, CO <sub>2</sub> uptakes, and heats of CO <sub>2</sub> adsorption of PA-POFs.....	79
Table 4-1. Langmuir and Freundlich adsorption isotherm parameters for the adsorption of BPA by PA-POF-2 [0.8:1].....	94
Table 4-2. The comparison of removal performance of several adsorbents used for BPA removal.....	95

# Abstract

Porous materials are of expanding scientific interest because of their ability to interact with atoms, ions, and molecules at their large interior pore surfaces at nanoscale throughout the bulk of the material. In this dissertation, a series of microporous materials and a mesoporous material are discussed.

In the first part, the synthesis of new anionic porous organic frameworks with phosphate groups (PA-POFs) through Yamamoto coupling reactions is presented. These materials have high adsorption capacity and exceptional adsorption kinetics towards bisphenol A (BPA) in water, a wide-spread organic pollutant and a known endocrine disruptor. The maximum adsorption capacity of BPA at equilibrium is found as high as 3,366 mg g<sup>-1</sup> by Langmuir adsorption model, which is more than ten times greater than peer materials. The polymer also rapidly removes various other organic micropollutants with more than 90% removal efficiencies. In addition, the PA-POF material can be regenerated at least five times by mild washing using methanol without significant loss in removal efficiency. The CO<sub>2</sub> adsorption capacity of these materials were also studied. The carbon dioxide uptake capacities of the PA-POFs reach up to 103 cc g<sup>-1</sup> (1.0 bar and 273 K), making them promising candidates for CO<sub>2</sub> capture.

In the second part, the crystallization of an amorphous Al-SBA-15 material under a strong flux of Li<sup>+</sup> with the retention of mesostructure is discussed. The crystalline lithium aluminosilicate (LAS) material was fully characterized by XRD, solid state NMR, TEM, SAXS, ICP-OES and EDS. The acidity and ion-exchange properties are studied.

# Chapter 1

## Introduction

### 1.1 Overview of porous materials

Porous materials exist widely in nature such as soil, sponges, zeolites, honeycombs, biological tissues such as bones and wood, and man-made materials such as activated carbons and porous ceramics. Porosity plays an important role in the properties of a material, yet whether it is beneficial or harmful depends on its purposes. For example, pores are treated as structural defects in super-hard materials because porosity weakens the strength and hardness. On the other hand, porosity in materials is of great value in many fields such as gas storage, materials separation, catalysis, and drug delivery.<sup>1</sup>

According to the International Union of Pure and Applied Chemistry (IUPAC), porous materials can be classified into three categories based on the pore sizes: pore sizes less than 2 nm are called micropores, those in the range of 2 nm to 50 nm are mesopores, and those above 50 nm are denoted macropores. The term “nanoporous” is frequently used to describe porous materials if the pore size falls in the range of nanometer scale, despite they are micropores, mesopores, or macropores. The development of nanoporous materials began from the study of zeolites. Zeolites are a class of crystalline microporous aluminosilicates, and the discovery of the first zeolite mineral, stilbite, dates back to 1756, by Swedish mineralogist A.F. Cronsted.<sup>2</sup> The word “zeolite” is derived from two Greek words, zeo and lithos, meaning “to boil” and “stone”. From 1777 through about the 1800s

various authors described the properties of zeolite minerals, including adsorption properties and reversible cation exchange and dehydration properties.<sup>2</sup> In 1862, the first hydrothermal synthesis of a zeolite, levynite, was reported by St. Claire Deville.<sup>2</sup> By the mid-1930s, the synthesis of a number of zeolites as well as the ion exchange, adsorption, molecular sieving and structural properties of zeolite minerals are described.<sup>2</sup> The early synthetic work remains unsubstantiated because of incomplete characterization and the difficulty in experimental reproducibility.<sup>2</sup> In 1948, Richard M. Barr reported the first definitive synthesis of the zeolitic mineral mordenite and its sorption and molecular sieve properties.<sup>3-5</sup> Between 1949 and 1959, R. M. Milton, D. W. Breck, T.B. Reed and D.W. Breck, *et al.* discovered a number of commercially significant zeolites, types A, X and Y.<sup>2,6</sup> Union Carbide also commercialized synthetic zeolites as a new class of industrial materials for separation, purification, and catalysis.<sup>6,7</sup> In 1962 Mobil Oil introduced the use of synthetic zeolite X as a hydrocarbon cracking catalyst. Later between 1967 and 1969 Mobil Oil reported the synthesis of the high silica zeolites beta and ZSM-5, which was soon used widely as a catalyst for several reactions carried out in the petrochemical industry.<sup>8</sup>

Today, millions of kilograms of synthetic zeolites are produced throughout the world using revised synthesis recipes that were initially discovered by the early pioneers. Zeolites have made great contributions to human society, with major applications as catalyst, detergent, deodorant, molecular sieves, *etc.*, and the field is still developing rapidly. Zeolites are not the only class of porous materials that practically benefit human society, other porous materials have also stepped onto the stage during the past three decades, such as porous carbons, mesoporous silicas, metal-organic frameworks (MOFs), covalent organic frameworks (COFs), and porous organic frameworks (POFs).



In this dissertation, a series of microporous anionic POFs with terminal phosphate functional groups with fully characterized structures are described in Chapter 2 to 4. The CO<sub>2</sub> adsorption properties of these anionic POFs are studied, and the results show that these materials have much higher CO<sub>2</sub> uptakes than their structurally related POF material. In addition, the massive and fast adsorption towards organic pollutants by these materials are investigated in Chapter 4, with a maximum bisphenol A adsorption capacity of 3,366 mg g<sup>-1</sup>. In Chapter 5, a mesoporous aluminosilica material is crystallized using a novel flux-grown technique.

Figure 1-1 presents examples of a variety of porous materials, roughly classified as zeolites, mesoporous silicas, nanoporous carbons (NPCs), metal-organic frameworks (MOFs), covalent organic frameworks (COFs), and porous organic frameworks (POFs).

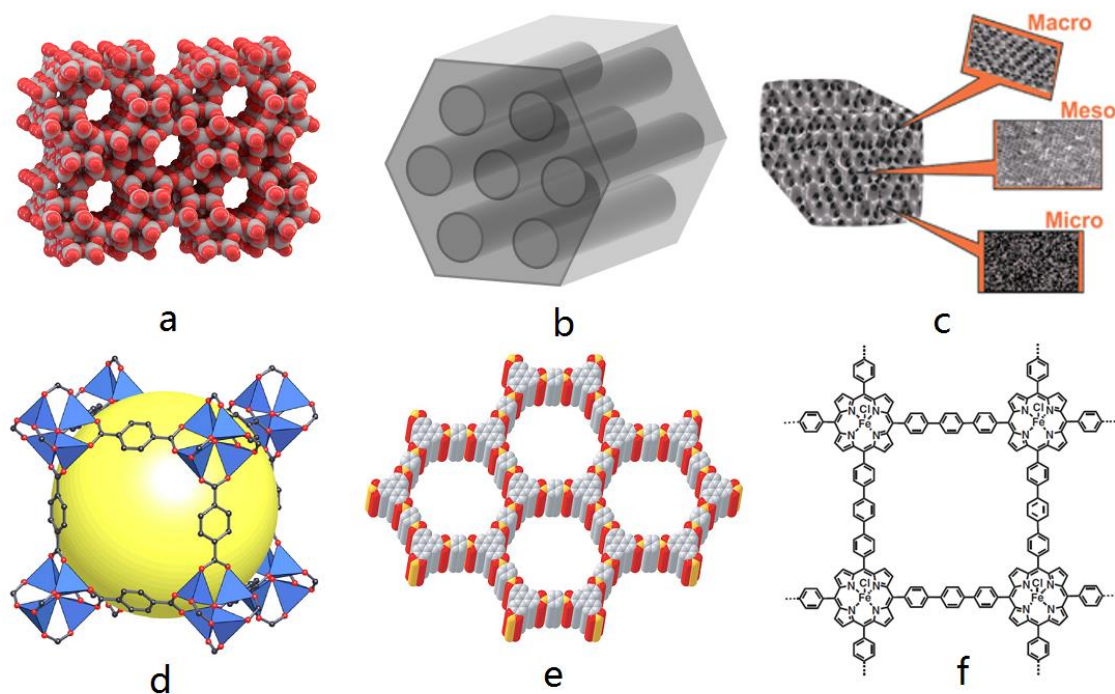


Figure 1-1. Examples of porous materials. (a) zeolite, (b) mesoporous silica, (c) nanoporous carbon, (d) metal-organic framework (MOF), (e) covalent organic framework (COF), and (f) porous organic framework (POF).

The history of zeolites has been briefly discussed in the beginning of this chapter. The building units of zeolites are  $\text{SiO}_4$  and  $\text{AlO}_4$  tetrahedra. The interconnected tetrahedra linked by corner-sharing O atoms therefore form an inorganic polymer. It is obvious from this building principle that negative charges reside at each  $\text{AlO}_4$  tetrahedron, so cations are needed to balance the overall charges. Thus when  $\text{H}^+$  ions are exchanged into the framework, Brønsted acid sites are created in the form of bridging OH groups. The Brønsted acid sites are very important to zeolites because the surface acidity enables the application of zeolites as catalysts. Among all the applications of zeolites, catalysis in petroleum industry is one of the most important applications of zeolites with an estimated annual market value of more than 1 billion USD by 2020.<sup>9</sup>

However, catalytic performance of zeolites is limited by their pore sizes. In general, zeolites are microporous materials, which restricts the transport of large organic molecules into the pores for catalytic reactions. Ordered mesoporous silicas were discovered in 1991 by ExxonMobil, and it was believed that they would soon replace zeolites in long chain hydrocarbon cracking because of their larger pore sizes. The pore size of mesoporous silicas can be tuned up to 30 nm.<sup>10</sup> The synthesis of mesoporous silicas is discussed in detail later in Section 1.3. Despite the much larger pore sizes in mesoporous silicas, the replacement of zeolites as catalysts was not successful mainly because of two reasons. First, there are inferior surface acidity in the mesoporous silicas. Secondly, the amorphous pore channel walls are not hydrothermally stable under the catalyst regeneration conditions in the petroleum cracking industry. To address the first problem, researchers have developed several strategies to introduce heteroatoms into the pore walls to give the materials potential surface acidity. To address the second problem, a novel method for the

production of a crystalline mesoporous aluminosilicate is presented as the second part of this dissertation in Chapter 5.

Nanoporous carbon materials (NPCs) are usually classified as ordered mesoporous carbons and disordered porous carbons based on the periodicity of the pore structures. Ordered mesoporous carbons can be synthesized by either the soft-templating method or hard-templating method, producing mesoporous carbon materials with certain pore structures including cubic, body centered cubic, gyroid, and hexagonal structures. Compared with ordered mesoporous carbons, disordered activated carbons (ACs) can be produced in fewer steps and in larger scale, and are less expensive because of the much cheaper carbon sources, e.g. charcoal. Recently, an increasing number of researchers have prepared ACs from agricultural by-products such as hazelnut shell, durian shell, almond shell, olive bagasse, palm shell, coconut shell, and so on.<sup>11-14</sup>

Zeolites, mesoporous silicas and nanoporous carbons are the three largest classes of inorganic nanoporous materials. The surface areas of zeolites, mesoporous silicas and ordered mesoporous carbons are usually not larger than  $1,500 \text{ m}^2 \text{ g}^{-1}$ , while the surface areas of disordered ACs could reach to more than  $3,000 \text{ m}^2 \text{ g}^{-1}$ , which are mostly contributed by interconnected micropores smaller than 2 nm.<sup>15</sup> These materials have been widely employed in industry because of their relatively low cost and high physicochemical stability. However, generally speaking, the surface functionalization of the pores in these materials cannot be easily controlled because of the relatively inert nature of the materials compared with organic nanoporous materials including metal-organic frameworks (MOFs), covalent organic frameworks (COFs), and porous organic frameworks (POFs). Besides, organic nanoporous materials are generally more porous than inorganic porous

materials, with surface areas as large as more than  $6,000 \text{ m}^2 \text{ g}^{-1}$ , making them more promising for applications such as gas adsorption and storage.

Metal-organic frameworks (MOFs) are a class of highly crystalline porous materials connected by dative bonds between metal nodes and organic linkers.<sup>16</sup> A large variety of MOFs with desirable functionalities and pore structures are synthesized by the selection from a tremendous choice of metal centers and organic building blocks. Developed from the construction of MOFs, Yaghi et. al. established a method called reticular chemistry which is now widely used in the design of periodic nanoporous materials by assembling molecular building blocks into pre-designed structures.<sup>17</sup> This chemistry has led to the design and synthesis of new crystalline porous organic materials for which the composition, structure, metrics, and functionality can be systematically adjusted. The last 15 years have witnessed a tremendous development of MOFs, with more than 20,000 papers and more than 15,000 structures reported.<sup>18</sup> A number of review articles give comprehensive description and detailed explanation of MOFs in regard to their design, synthesis, modification, processing, and applications.<sup>19-22</sup>

Covalent organic frameworks (COFs) are another class of crystalline organic porous polymers which are two-dimensional or three-dimensional frameworks linked by bi-, tri- or tetravalent organic ligands. The crystallinity of the COFs is due to the reversibility of the covalent bond formation in the polymerization reactions, which favors the production of thermodynamically controlled polymers. The first work on COFs was reported in 2005 by the Yaghi group.<sup>23</sup> They reported the synthesis of COF-1 and COF-5 through the self-condensation reaction of 1,4-benzenediboronic acid (boroxine anhydride formation reaction) and the co-condensation reaction of 1,4-benzenediboronic acid with

2,3,6,7,10,11-hexahydroxytriphenylene (boronate ester formation reaction), respectively.<sup>23</sup> Similar to MOFs, the variety of molecular building blocks and customized functionalization have made it possible for the synthesis of COFs with pre-designed pore structures and a wide range of properties including gas adsorption and storage, catalysis, energy storage, *etc.*<sup>24</sup>

Porous organic frameworks (POFs), or porous organic polymers (POPs), include many kinds of porous polymers such as microporous organic polymers (MOPs), porous coordination polymers (PCPs), covalent triazine frameworks (CTFs), conjugated microporous polymers (CMPs), hypercrosslinked polymers (HCPs), microporous polymer networks (MPNs), porous polymer networks (PPNs), porous aromatic frameworks (PAFs), *etc.* These materials are a big family of amorphous polymers that possess high surface areas and tunable pore structures. Usually POFs are covalently connected by simple organic ligands with light elements such as C, H, O, N, S. The complicated post-synthetic modifications with certain functional groups or metal/non-metal ions further enrich the diversity of POFs and their functions. For example, lithiation imparts conjugated microporous polymers (CMPs) with competence for H<sub>2</sub> storage (6.1 wt % at 1 bar and 77 K), thereby making them useful for clean fuel applications.<sup>25</sup> The applications of POFs include molecular adsorption, catalysis, and separation. Moreover, carefully chosen building blocks produce POF materials with special properties. Taking CMPs as an example, CMPs are built up from aromatic linkers that have alternating single and multiple bonds.<sup>26</sup> The overlapping p orbitals (or d orbitals) create a system of delocalized  $\pi$  electrons, which allows high capability for optical and electronic applications.

Among organic nanoporous materials, MOFs and COFs are superior in terms of

crystallinity compared with POFs, from which a better understanding of their structures at both atomic and nanometer scales is attained. However, due to the relatively weak strength of metal-nonmetal dative bonds in MOFs and the reversibility in the formation of the covalent bonds in COFs, these two kinds of materials are generally not as thermally and/or hydrothermally stable as POFs. In addition, COFs are so far only produced through condensation reactions, while the reaction pathways for producing POFs are highly diverse and ranging from not only condensation reactions such as metal-catalyzed coupling reactions and metal-free imide-formation reaction, but also addition polymerization reactions such as ethynyl cyclo-trimerization. A detailed discussion for the synthesis of POFs is presented below in section 1.2.

## 1.2 Synthesis of porous organic frameworks

### 1.2.1 Synthetic methodology for porous organic frameworks

The past years have witnessed an expansion of synthetic methodologies for preparing porous organic frameworks (POFs). Generally, polymerizable monomers are used for the production of POFs using various chemical reactions. Two key issues are required to be addressed for the successful preparation of POFs. First, it is necessary to judiciously choose the correct monomer to ensure that the resultant frameworks have sufficient mechanical stability. The monomers are generally needed to have multiple reaction sites and rigid structures to form a framework or a distorted linear polymer. Secondly, effective chemical synthesis reactions are required to link the monomer building blocks together. Moreover, with the help of efficient synthetic protocols, incorporating certain key components into the polymeric scaffold plays an important role in giving rise to porous polymers with

fascinating properties.

The representative chemical synthetic routes for POFs are summarized in Table 1.1. A typical example of POFs is PAF-1, which is formed through nickel-promoted Yamamoto coupling reaction (Figure 1-2).<sup>27</sup> The strategy of the design of PAF-1 is to mimic the stable structure of diamond, in which each carbon atom is tetrahedrally connected to four neighboring atoms by covalent bonds. In PAF-1, tetrakis(4-bromophenyl) methane was used as monomer in order to replace the C-C covalent bonds of diamond with rigid phenyl rings.<sup>27</sup>

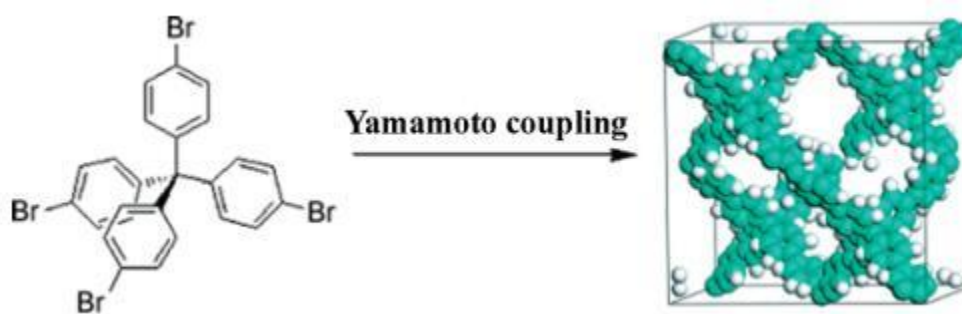
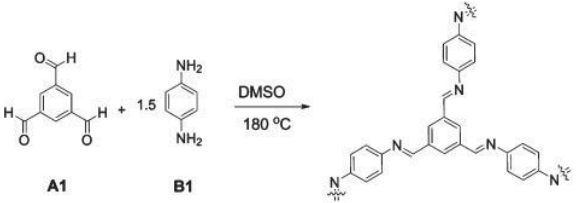
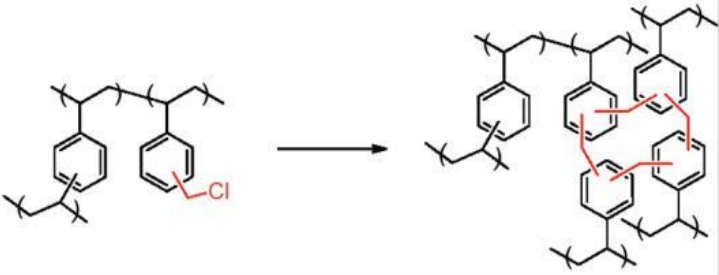
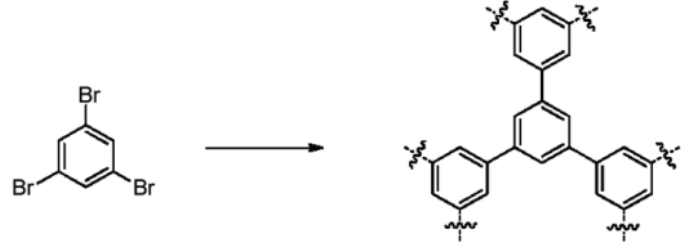
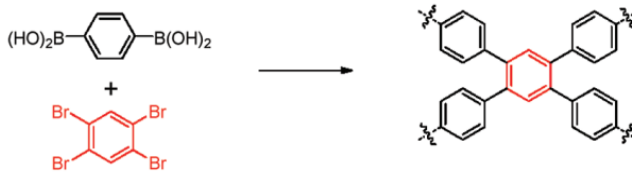
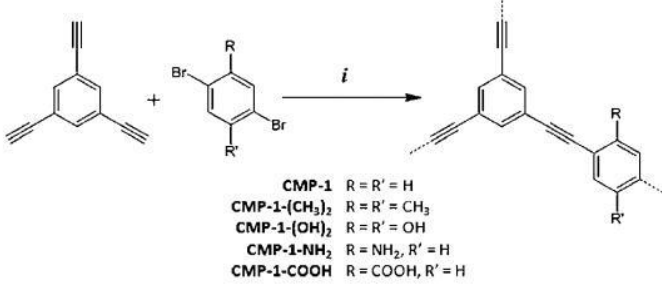
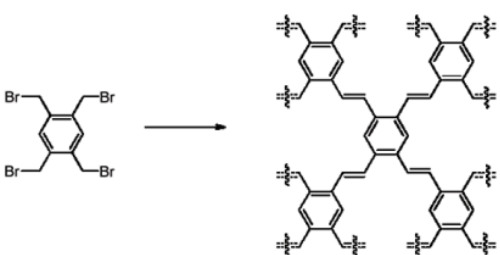


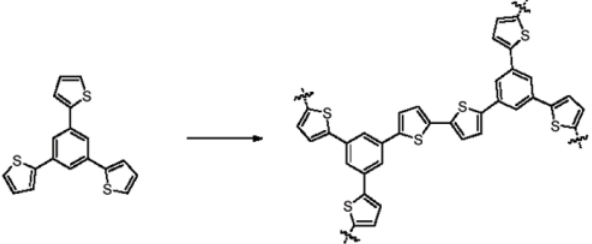
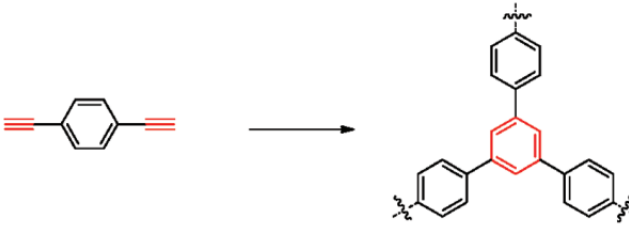
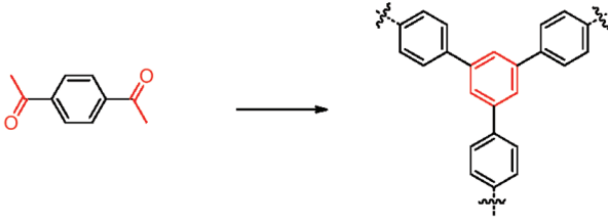
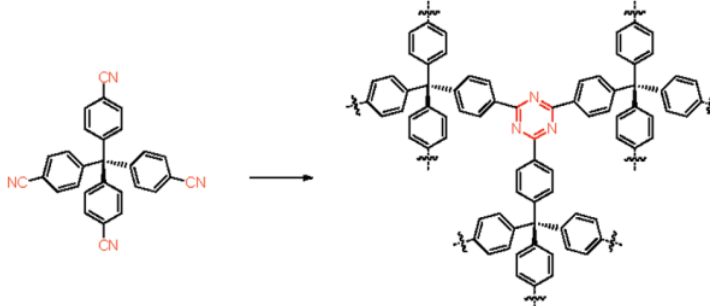
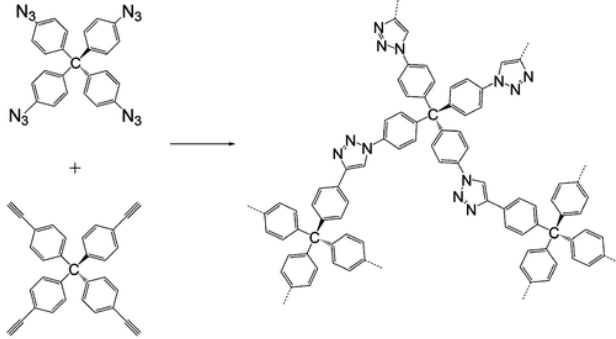
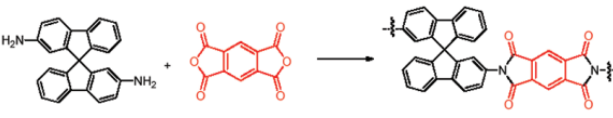
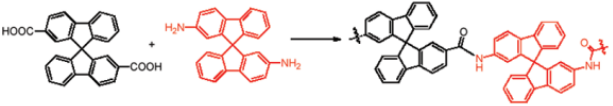
Figure 1-2. Synthesis scheme of a PAF-1 with ultrahigh surface area by the Yamamoto-type Ullmann cross-coupling reaction. Ref. 27.

PAF-1 shows an ultrahigh BET surface area,  $5,600 \text{ m}^2 \text{ g}^{-1}$ .<sup>27</sup> It also shows high thermal and hydrothermal stability, retained its structure in air up to  $520 \text{ }^\circ\text{C}$  and in boiling water for 7 days.<sup>27</sup> By replacing the monomer tetrakis(4-bromophenyl) methane with tetrakis(4-bromophenyl) silane, PPN-4 was synthesized with an even higher BET surface area of  $6,461 \text{ m}^2 \text{ g}^{-1}$  and Langmuir surface area of  $10,063 \text{ m}^2 \text{ g}^{-1}$ .<sup>28</sup> The material showed excellent gas adsorption properties including hydrogen, methane, and  $\text{CO}_2$  because of its exceptionally large surface area and pore volume.<sup>28</sup>

Table 1-1. Summary of Representative Chemical Reactions for the synthesis of POFs.

#	Reaction Type	Reaction	Ref.
1	Schiff-base Reaction	 <p style="text-align: center;"> <math>\text{A1} + 1.5 \text{ B1} \xrightarrow[180\text{ }^\circ\text{C}]{\text{DMSO}}</math> </p>	29
2	Friedel-Crafts Alkylation		30
3	Yamamoto Coupling Reaction		27,28
4	Suzuki Coupling Reaction		31
5	Sonogshira Coupling Reaction	 <p style="text-align: center;"> <math>\text{CMP-1} \quad \text{R} = \text{R}' = \text{H}</math>  <math>\text{CMP-1-(CH}_3)_2 \quad \text{R} = \text{R}' = \text{CH}_3</math>  <math>\text{CMP-1-(OH)}_2 \quad \text{R} = \text{R}' = \text{OH}</math>  <math>\text{CMP-1-NH}_2 \quad \text{R} = \text{NH}_2, \text{R}' = \text{H}</math>  <math>\text{CMP-1-COOH} \quad \text{R} = \text{COOH}, \text{R}' = \text{H}</math> </p>	32
6	Gilch Coupling Reaction		33



7	Oxidative Coupling		34
8	Ethynyl Cyclo-trimerization		35
9	Acetyl Cyclo-trimerization		36
10	Cyano Cyclo-trimerization		37
11	Click Chemistry		38
12	Imidization		39
13	Amidization		40

In addition to Yamamoto coupling, other coupling reactions such as Suzuki coupling,<sup>31</sup> Sonogashira coupling,<sup>32</sup> Gilch Coupling,<sup>33</sup> and Buchwald–Hartwig (BH) coupling reactions<sup>41</sup> for generating strong C-C or C-N covalent bonds are also used in the preparation of POFs. Control over pore size, surface area, and gas uptake of the POFs could be enabled by the change of the lengths, rigidities, and functionalities of the building blocks. For example, as shown in Figure 1-3 and 1-4, the BET surface area decreases from 1,018 to 512 m<sup>2</sup> g<sup>-1</sup> from CMP-0 (conjugated microporous polymer-0) to CMP-5, as the length of monomer strut increases.<sup>42</sup> The pore size distribution is systematically shifted to larger pore diameters (Figure 1-4 b), and the overall micropore volume falls from 0.38 to 0.16 cm<sup>3</sup> g<sup>-1</sup> over the series.<sup>42</sup> This work represents an important step towards the fine control of the structure of the micropores in POFs. These conjugated frameworks can be further functionalized by attaching pendant functional substituents such as methyl, hydroxyl, carboxyl and amine groups onto the building blocks.<sup>32,43</sup> This combination of changes in lengths of the linkers and functional groups variates the properties of the POFs such as pore structure, hydrophobicity, and incorporation of surface functional groups for applications such as CO<sub>2</sub> capture and catalysis.

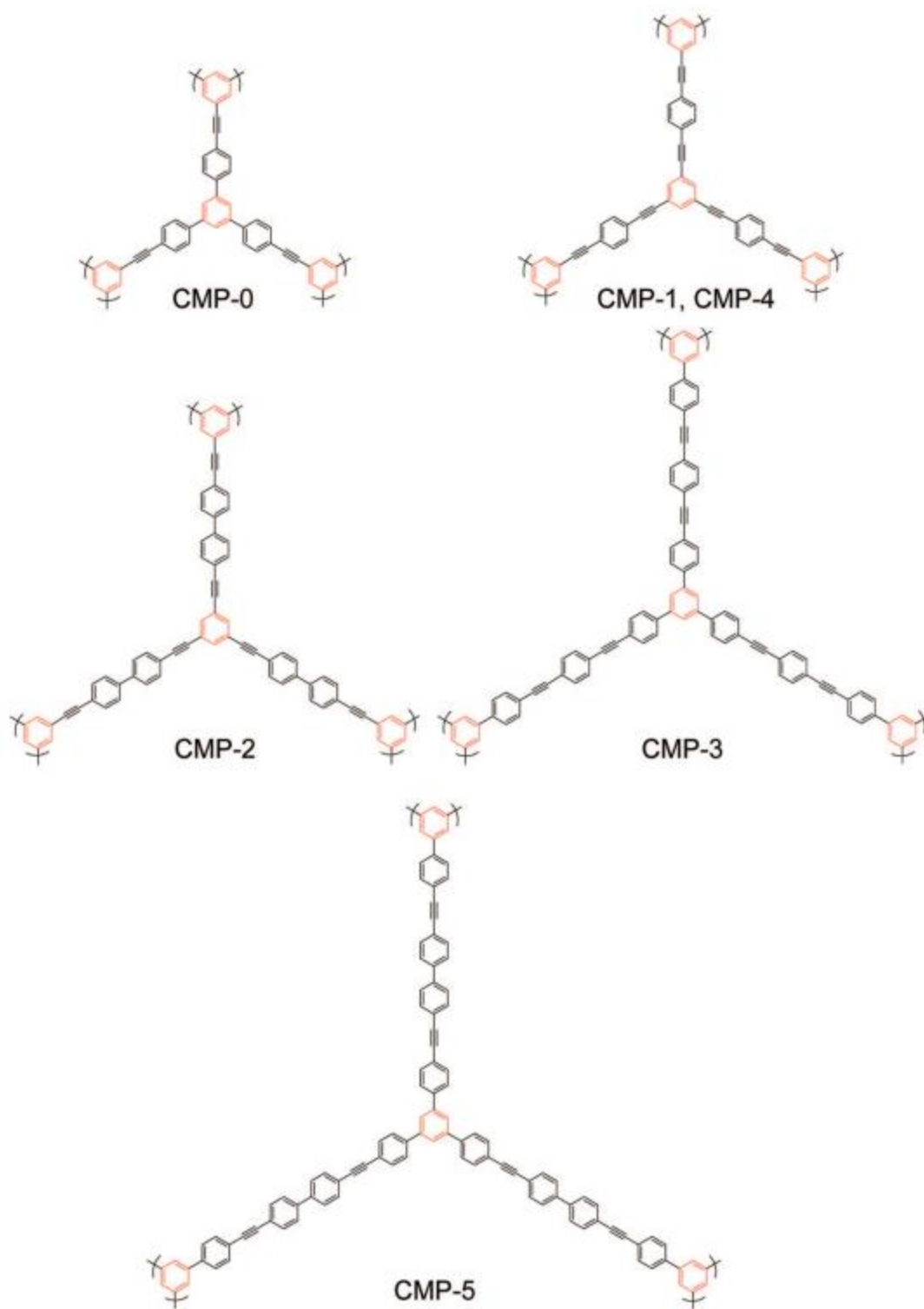


Figure 1-3. Representative molecular structures for CMP-0 to CMP-5. Ref. 42.

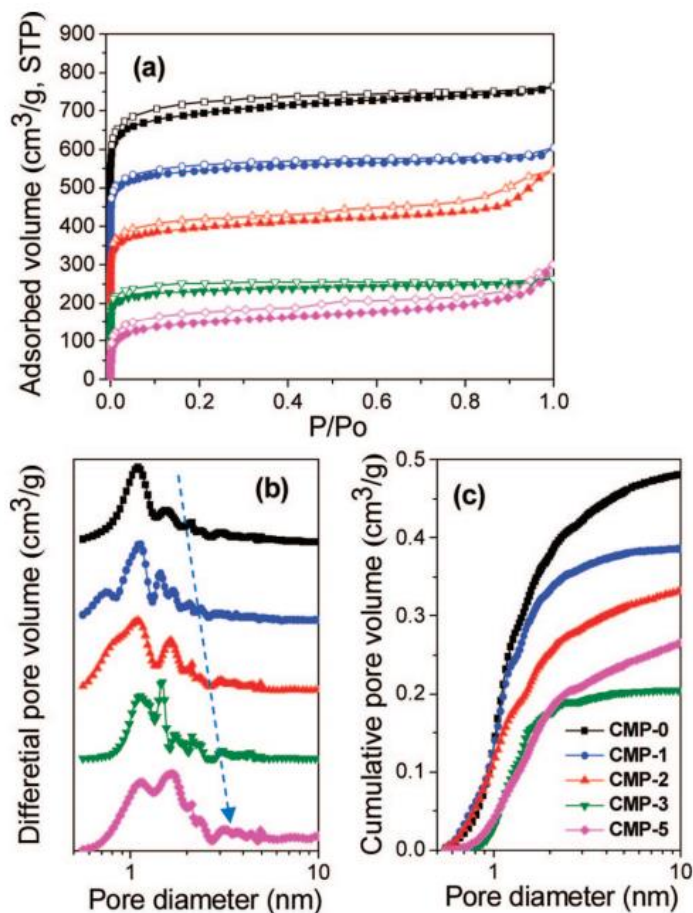


Figure 1-4. (a) N<sub>2</sub> adsorption-desorption isotherms measured at 77.3 K. For clarity, the isotherms of CMP-0, CMP-1, CMP-2, and CMP-3 were shifted vertically by 400, 300, 200, and 100 cm<sup>3</sup> g<sup>-1</sup>, respectively. (b) NL-DFT pore size distribution curves. (c) Cumulative pore volume curves calculated by application of NL-DFT. Ref. 42.

There are a lot more reactions that can be used to fabricate POFs other than the coupling reactions mentioned above, such as hyper-cross-linked styrenic polymers formed through Friedel–Crafts alkylation reaction,<sup>30</sup> microporous polymers formed through cyclotrimerization reactions among ethynyl, acetyl or cyano groups,<sup>35–37</sup> the POFs formed through the formation of amides or imides,<sup>39,40</sup> polyphenylene networks with surface areas above 2,000 m<sup>2</sup> g<sup>-1</sup> through one step AlCl<sub>3</sub>-mediated coupling of aromatic hydrocarbons,<sup>44</sup> *etc.* Different POFs with a great variety of properties through chemical processes are

produced by careful selection of building blocks in the molecular design. In addition to the direct synthesis for the assembly of functional groups, a diverse range of chemical functionalities can also be precisely incorporated into the surface or interior of the polymeric frameworks by post-synthetic modification. The functional groups can provide additional interesting properties to the porous polymers, including responding selectively and reversibly to external stimuli such as pH, temperature, and applied electrical fields, which are often impossible for inorganic porous materials such as zeolites and activated carbons.<sup>45</sup> Furthermore, with the rapid development in synthetic chemistry, new tools are available for the design and construction of POFs, providing unprecedented opportunities for creating novel POFs with uniform or hierarchical porous structures and site-specific functionalities.

### 1.2.2 Synthesis of weakly coordinating anionic porous organic frameworks (WCA-POFs)

Weakly coordinating anions (WCAs) are a class of anions that interact weakly with cations.<sup>46</sup> This type of anions should have low overall charge and more importantly, a high degree of charge delocalization. In most cases, weakly coordinating anions have a -1 charge (e.g.  $\text{ClO}_4^-$ ), but in some cases a species with a -2 charge (e.g.  $\text{SiO}_6^{2-}$ ) can also exist. The charge is widely delocalized over the entire anion usually because of the stronger electron negativity on the periphery atoms or group of atoms, so that no individual moiety bears a high concentration of charge density. This spread of the negative charge over the entire ion further suggests a larger anion may have more delocalized charge and therefore be more

weakly coordinating. In addition, the central atom of a WCA is usually in its highest coordination state, therefore direct coordination between the central atom and the cation is forbidden. Weakly coordinated ion pairs are of fundamental importance to a variety of chemistries. For example, anionic  $[\text{HB}(\text{C}_6\text{F}_5)_3]^-$  ion weakly coordinates with catalytically active Zr complexes in olefin polymerization, because the boron center is surrounded by highly electronegative functional groups, and is resistant to electrophilic attack of metal complexes.<sup>47</sup> Due to the very low tendency of WCAs to interact with cations, highly electrophilic and strong oxidative cations such as  $[\text{NO}_2]^+$  can be stabilized by WCAs.<sup>48</sup> George A. Olah prepared the so-called magic acids that show the ability to protonate hydrocarbons to produce carbocations, which fundamentally are WCAs with protons as the cations.<sup>49</sup>

In most cases, POFs/COFs are constructed with neutral ligands or linkers. Recently, weakly coordinating anionic porous organic frameworks and covalent organic frameworks were reported in which a suitably functionalized organic WCA was polymerized to form a porous network.<sup>50-53</sup> In these materials, the combination of porous polymers with anions provides these materials with novel properties. For example, Figure 1-5 shows the synthesis of an anionic framework, ICOFs.<sup>52</sup> In ICOFs, spiroborate linkages are directly synthesized through the slow condensation of polyols with trimethyl borate under basic condition. The anionic centers form in the reaction and link the monomers together. The presence of immobilized anion centers in ICOFs enables the transportation of cations. ICOF-2, where lithium ions exist as cations in the polymer, shows room-temperature lithium-ion conductivity of  $3.05 \times 10^{-5} \text{ S cm}^{-1}$  and an average  $\text{Li}^+$  transference number value of  $0.80 \pm 0.02$ . The ICOFs enable the transportation of lithium ions, suggesting their

potential applications as solid electrolytes.<sup>52</sup>

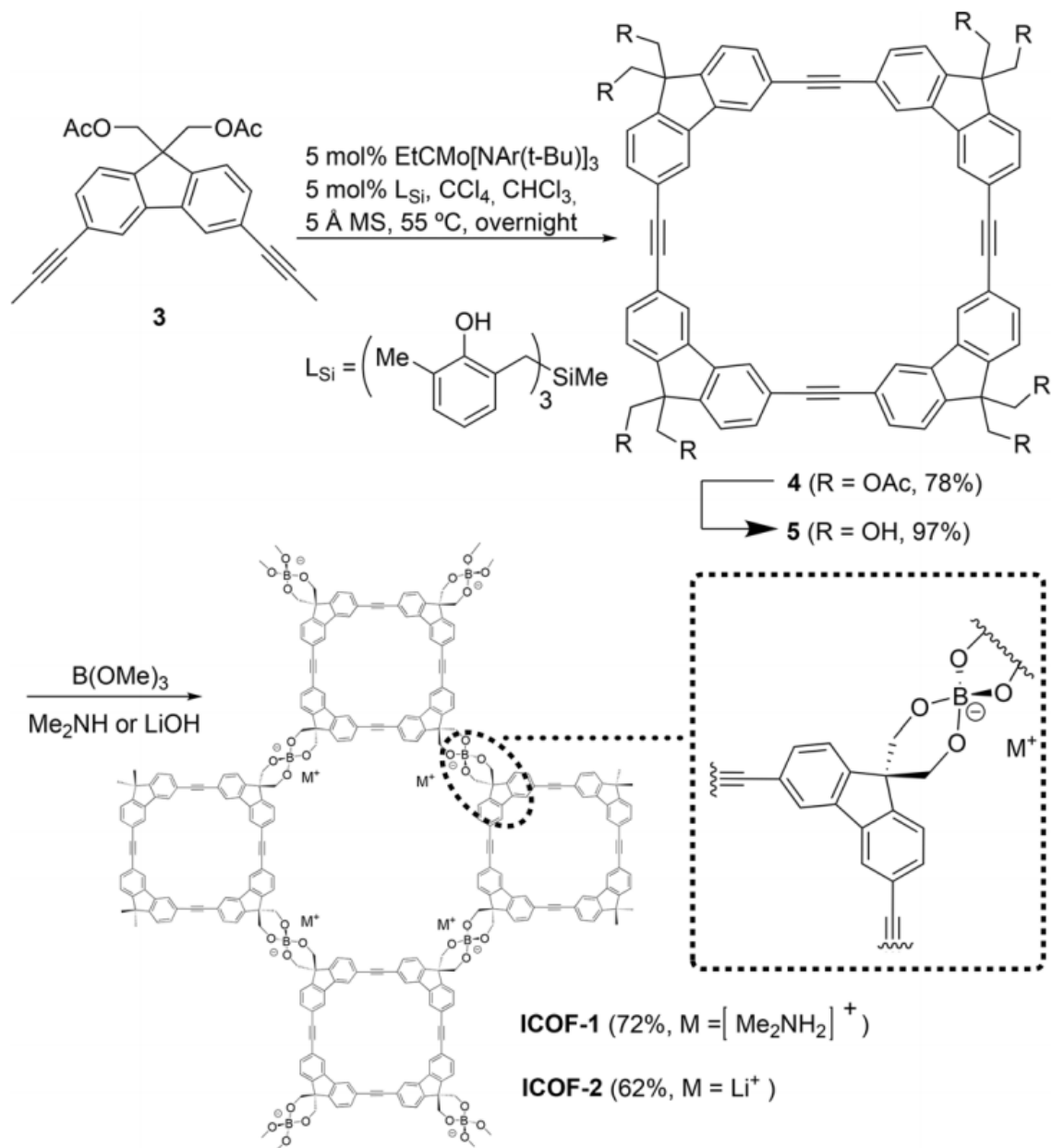


Figure 1-5. Synthesis of ICOF-1 and ICOF-2. Ref. 52.

As opposed to the above mentioned one-pot synthesis in which anionic centers form in the polymerization reaction, WCAs can also be synthesized as monomers before polymerization. As shown in Fig. 1-6, the tetra-coordinated borate anion (lithium tetrakis(4-bromo-2,3,5,6-tetrafluorophenyl)borate ( $\text{Li}[\text{B}(\text{C}_6\text{F}_4\text{Br})_4]$ )) was firstly synthesized, bearing Ph-Br functional groups for later polymerization.<sup>50</sup> Then the authors copolymerize the borate anions with 1,3,5-triethynylbenzene through Sonogashira coupling between bromobenzene and ethynyl functional groups. The network Li-ABN showed a surface area of  $890 \text{ m}^2 \text{ g}^{-1}$  and a pore volume of  $0.61 \text{ cm}^3 \text{ g}^{-1}$ . After Li ions were exchanged by Na ions in the networks by stirring in saturated sodium chloride solution, a slightly reduced surface area of  $731 \text{ m}^2 \text{ g}^{-1}$  and pore volume of  $0.48 \text{ cm}^3 \text{ g}^{-1}$  were observed, which could be explained by the higher molecular mass and larger size of the sodium ions compared to lithium ions. This work confirmed another novel property of WCA-POF: pore size and pore volume of WCA POFs/COFs can be simply adjusted by exchanging cations with different sizes.

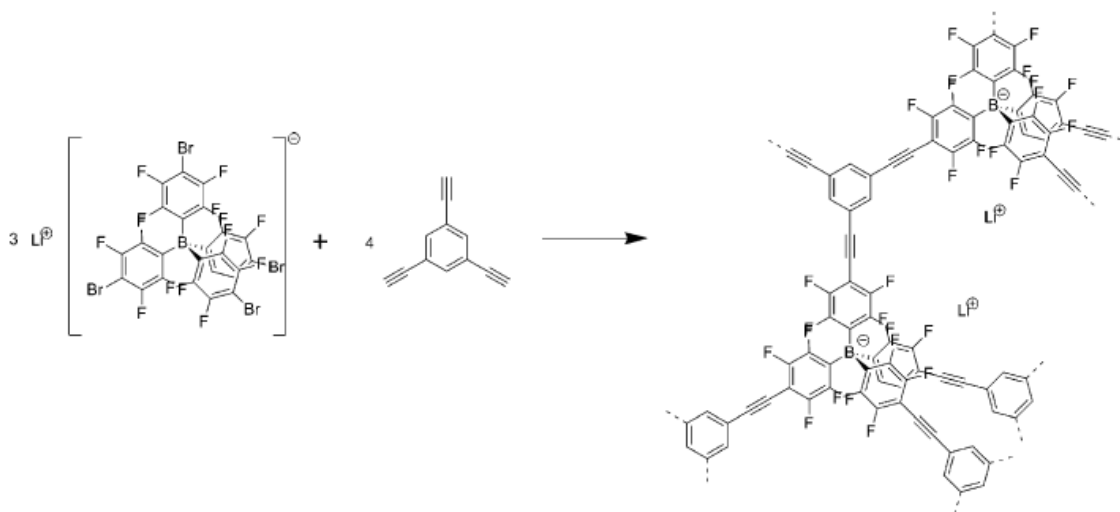


Figure 1-6. Synthesis of Li-ABN. Ref. 50.



The structure and properties of WCA-POFs are distinct from neutral POFs because of their weakly coordinating character towards cations. Solid super acid may be realized by exchanging protons into the framework. Since the framework only weakly interacts with cations, high cation mobility is expected, and therefore WCA-POFs may also be used as solid electrolytes, whose eligibility has already been proved in Ref. 52. Opportunities for heterogeneous catalysis could be realized in WCA-POFs if catalytically active cationic metal complexes are introduced into the framework. The large surface areas in WCA-POFs enable much more catalytically active sites compared with nonporous catalysts. The specific pore size may be beneficial for size and shape selectivity in catalytic reactions. In all of the very few WCA-POF materials known to date, tetra-coordinated boron and hexa-coordinated silicon are the carriers of the formal negative charge. It is expected to expand the scope of WCA-POFs to other central elements such as hexa-coordinated phosphorus, and the synthesis of such materials is introduced in Chapter 2.

## 1.3 Synthesis of mesoporous silica materials

### 1.3.1 Synthesis of mesoporous silica materials

The first examples of mesoporous silicas, M41S, are discovered by Mobil in 1992.<sup>54</sup> These mesoporous materials are formed by a mechanism in which surfactant liquid crystal phases serve as soft templates (Figure 1-7).<sup>55</sup>

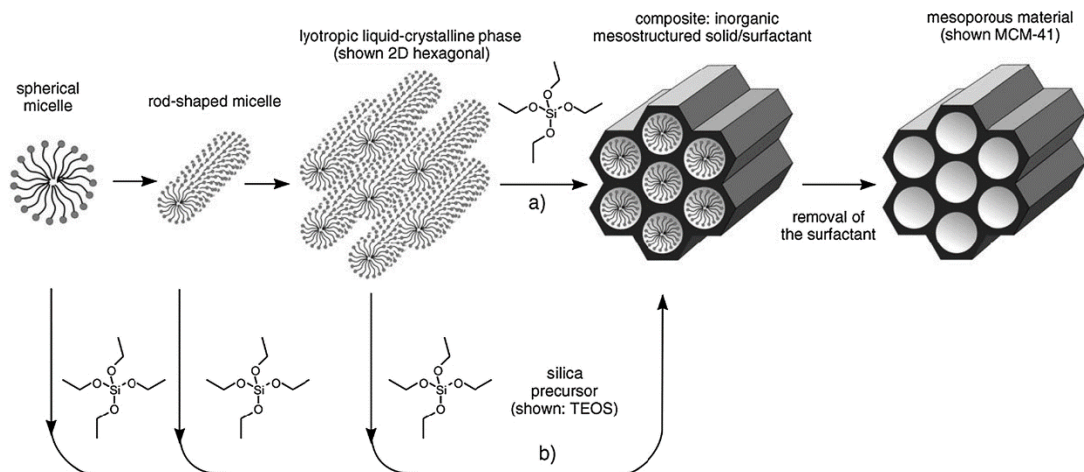


Figure 1-7. Schematic synthesis pathways of self-assembly of surfactant for the formation of MCM-41: (a) liquid crystal phase initiated, and (b) silicate initiated. Ref. 55.

It is well known that self-assembly occurs when molecules spontaneously organize through a balance of attractive and repulsive interactions. These interactions are generally weak and noncovalent, e.g. van der Waals interactions,  $\pi$ - $\pi$  interactions, and hydrogen bonds. In the formation of the M41S family, silica precursors and the surfactant molecules self-assemble to form hexagonal, lamellar, or cubic structures. As shown in Figure 1-7, the composite hexagonal mesostructure could be formed in two ways: 1. by condensation of silicate precursor around the pre-organized hexagonal surfactant liquid crystals, or 2. by adsorption of silicate species onto the external surfaces of randomly ordered rod-like micelles through coulombic or other types of interactions, and next these randomly ordered composite species spontaneously pack into a highly ordered mesoporous phase with an energetically favorable hexagonal arrangement, accompanied by silicate condensation.<sup>55</sup> Upon removal of the surfactant micelles, the ordered hexagonal mesoporous structure was retained.

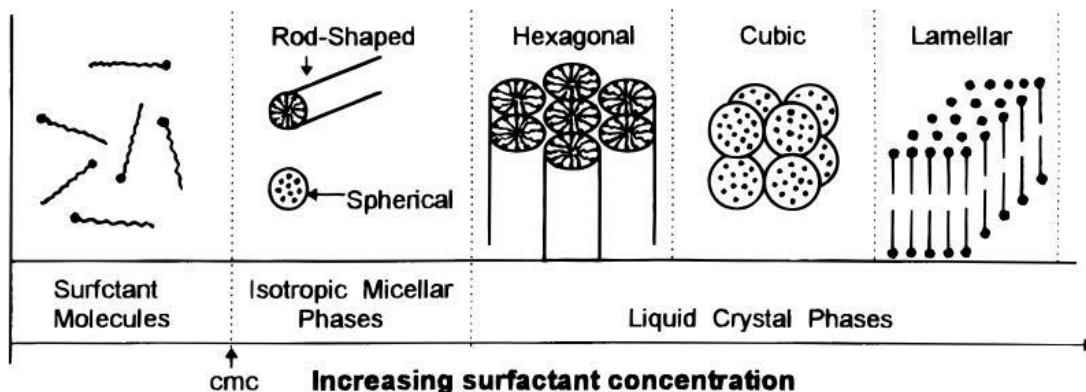


Figure 1-8. Phase sequence of surfactant-water binary system. CMC = critical micellization concentration. Ref. 56.

The pore structures of mesoporous silicas are based on the various structures of surfactant micelle assemblies, and the structures of micelle assemblies rely greatly on the concentration of surfactant molecules in the solution. Figure 1-8 shows the liquid crystal structures that surfactant molecules form with increasing concentrations in a simple water-surfactant binary system.<sup>56</sup> At low concentrations, the surfactants energetically exist as free single molecules. With increasing concentration, surfactant molecules start to form micelles when the critical micellization concentration (CMC) is met. As the concentration continues to increase, rod-shaped micelles start to pack into hexagonal close packed arrays, producing the hexagonal liquid crystal phases. Higher concentration in the process causes the coalescence of the adjacent, mutually parallel cylinders to produce the lamellar phase. In some cases, the cubic phase appears prior to the lamellar phase. According to Myers, the particular liquid crystal phase formed in an aqueous surfactant solution depends not only on the concentration of surfactant but also on the following characteristics of the surfactant and environmental parameters: length of the hydrophobic carbon chain,

hydrophilic head group, counterion, pH, temperature, the ionic strength, and other additives.<sup>57</sup> These parameters are reflected by the effect on the CMC. Generally, the CMC decreases with the increase in the number of carbon atoms in the unbranched chain of a surfactant, the valency of the counterions, and the ion strength in a solution, respectively. On the other hand, CMC changes with different pH, temperature, nature of hydrophilic group, and the nature of the counterion.<sup>57</sup>

To obtain a mesostructure with the soft-templating approach, there are four conditions to fulfill: 1) the soft template must self-assemble into ordered liquid crystals, 2) at least one precursor must interact with the template and form a framework surrounding the micelles, 3) the template must not decompose before the precursors transform to a rigid structure, 4) the precursors must form a highly crosslinked framework that is strong enough to support the porous structure without collapse.<sup>58</sup> According to these rules, a handful of mesoporous silica materials have been produced with different pore structures. To name a few, MCM-48 (Cubic  $Ia\bar{3}d$ ),<sup>54</sup> SBA-15 (Hexagonal  $p6mm$ ),<sup>59</sup> SBA-16 (Cubic  $Im\bar{3}m$ ),<sup>60</sup>[56] and KIT-6 (Cubic  $Ia\bar{3}d$ ),<sup>61</sup> *etc.* have been reported and extensively studied.

### 1.3.2 Synthesis of mesoporous aluminosilica materials

The initial motivation of the development of mesoporous silicas was to replace zeolites for long-chain hydrocarbon cracking in the petroleum industry. However, soon researchers found that mesoporous silicas were not able to accomplish the task because of the lack of acid sites. As known, the active acid sites in zeolites are from heteroatoms. Much attention has therefore been devoted to dope heteroatoms such as Al into the amorphous silica

framework. Generally, direct synthesis and post-synthetic grafting are two typical ways used for the introduction of heteroatoms.

A direct synthesis is very efficient for achieving high aluminum loadings in the silica networks. However, the resulting materials could have many extra-framework aluminum species.<sup>62</sup> The major difficulties of direct synthesis of aluminum-substituted mesoporous materials are: (1) the easy dissociation of Al-O-Si bond under acidic hydrothermal condition which is usually used in mesoporous silica synthesis and (2) the very different hydrolysis rates of siliceous sources and aluminum sources. To address the first problem, a “pH-adjusting” method has been applied to the direct synthesis.<sup>63</sup> In this method, the heteroatom source (Al or Ti) is added into the pre-hydrolyzed silicate sol in strongly acidic media ( $\text{pH} < 0$ ). When the mesostructure is basically formed, the pH value of the system is adjusted from strongly acidic ( $\text{pH} < 0$ ) to neutral ( $\text{pH} \sim 7.5$ ), followed by a hydrothermal treatment, during which a large amount of heteroatoms can be introduced into the mesophase. Based on the pH-adjusting method, Li *et al.* further enhanced the ordering and the hydrothermal stability of Al-SBA-15 material with the help of high aging temperature and the addition of sodium chloride.<sup>64</sup>

In order to incorporate Al atoms in a silica network, an effective method is to bring the hydrolysis and condensation rates of Al and Si precursors close to each other, which is meant to address the second difficulty. This difficulty could be resolved by two strategies: (1) decrease the hydrolysis rate of Al, and (2) accelerating the hydrolysis rate of silicon. Yue and coworkers reported a direct synthesis of an aluminium-incorporated SBA-15 material using aluminum tri-tert-butoxide ( $\text{Al}(\text{OC}(\text{CH}_3)_3)_3$ ) as an aluminum precursor at a pH of 1.5.<sup>62</sup> The hydrolysis rate of Al precursors were considerably slowed down by

complexing them with chelating agents. Zhang and coworkers prepared Ti-SBA-15 by controlling the hydrolysis rate of the siliceous source in the presence of fluoride under strong acidic conditions.<sup>65</sup> In 2004, Li and coworkers directly fabricated Al-SBA-15 materials also by using fluoride in accelerating the hydrolysis of tetraethyl orthosilicate (TEOS).<sup>66</sup> Simply changing the silica precursor from TEOS to tetramethyl orthosilicate (TMOS) could have a similar effect because TMOS hydrolyzes faster than TEOS does, due to the steric hindrance at ethoxide moieties and reduced solvation of the resulting ethanol.<sup>64,67</sup> Other studies suggested that structurally ordered Al-SBA-15 samples can be synthesized at slightly higher pH (2-5) conditions, with the rate of hydrolysis of the silica source and condensation with Al ions controlled by adjusting the H<sub>2</sub>O to HCl molar ratio of the synthesis gel.<sup>68,69</sup>

Post-synthetic grafting is the other commonly used method to introduce Al into the silica framework. Grafting is a post-synthesis method to modify the surface of inorganic mesoporous materials by attachment of functional groups. In this regard, silanol groups on the wall surfaces of mesoporous silica are used for the reaction with the aluminum sources. For example, the grafting with trimethylaluminium (TMA),<sup>70</sup> aluminium chloride,<sup>71</sup> aluminium isopropoxide,<sup>72</sup> and (NH<sub>4</sub>)<sub>3</sub>AlF<sub>6</sub><sup>73</sup> were performed and then followed by calcination. The post-synthetic grafting method normally keeps the mesostructural order intact, however, it limits the amount of incorporated aluminium.

Aluminosilicas obtained by either direct synthesis or grafting have amorphous pore channel walls. The amorphous pore walls of mesoporous aluminosilicas make them less hydrothermally stable during the catalyst regeneration process and hence limits their applications in petrochemical industry compared to microporous zeolites. Therefore,

various efforts were made for the production of periodic mesoporous aluminosilica materials with crystalline pore channel walls.

### 1.3.3 Synthesis of mesoporous aluminosilica materials with crystalline pore channel walls

At ambient pressure, amorphous silica crystallizes at very high temperature (> 1500 °C) through melting. Amorphous silica can also recrystallize through dissolution under hydrothermal conditions at ~300 °C and a pressure of 10-30 MPa.<sup>74,75,76</sup> However, under these conditions, the original ordered mesostructure collapses. The Landskron group has established a method called nanocasting at high pressure.<sup>77</sup> In this technique, the mesoporous silica/aluminosilica-carbon composite starting material is treated with high pressure (2-14 GPa) and temperature (300 – 800 °C). Owing to the high surface area and porous structure of mesoporous silicas/aluminosilica, they usually exhibit higher reaction activity during the high pressure reaction than the bulk materials. Under high pressure, the silica can be transformed into the high-pressure crystalline phase. The mesostructure does not collapse because the pores are supported by the infiltrated carbon. Upon oxidation of the carbon support, a periodic mesoporous high-pressure phase is obtained. Mesoporous coesite,<sup>78</sup> quartz,<sup>79</sup> stishovite,<sup>80</sup> and a mesoporous crystalline aluminosilica material<sup>81</sup> were successfully synthesized using the nanocasting at high pressure technique. However, this technique requires a special high-pressure apparatus which is not very readily available. Besides, the size of the materials synthesized using this technique is usually very small (on the scale of several milligrams), which is not applicable for industrial uses.

A flux-grown technique is used for slow growth of bulk single crystalline materials

such as  $\text{GeO}_2$  and  $\text{GaPO}_4$  under ambient pressure.<sup>82</sup> Compared with the hydrothermal growth method, the single crystals grown from this method have higher quality, less numbers of hydroxyl groups and structural defects. In 2013, Sanchez and coworkers reported the growth of epitaxial thin films of  $\alpha$ -quartz on single crystal silicon substrates from amorphous silica.<sup>83</sup> The key to this process is the combined use of a strontium ( $\text{Sr}^{2+}$ ) or barium ( $\text{Ba}^{2+}$ ) catalyst with an amphiphilic molecular template. The epitaxial growth of quartz on the silicon (100) plane is induced by the low mismatch in the lattice parameters.<sup>83</sup> Later in 2015, the same group reported that hollow mesoporous silica nanoparticles were transformed from amorphous phase into pure polycrystalline  $\alpha$ -quartz using catalytic quantities of alkaline earth metals as devitrifying agent without the use of carbon support.<sup>84</sup>

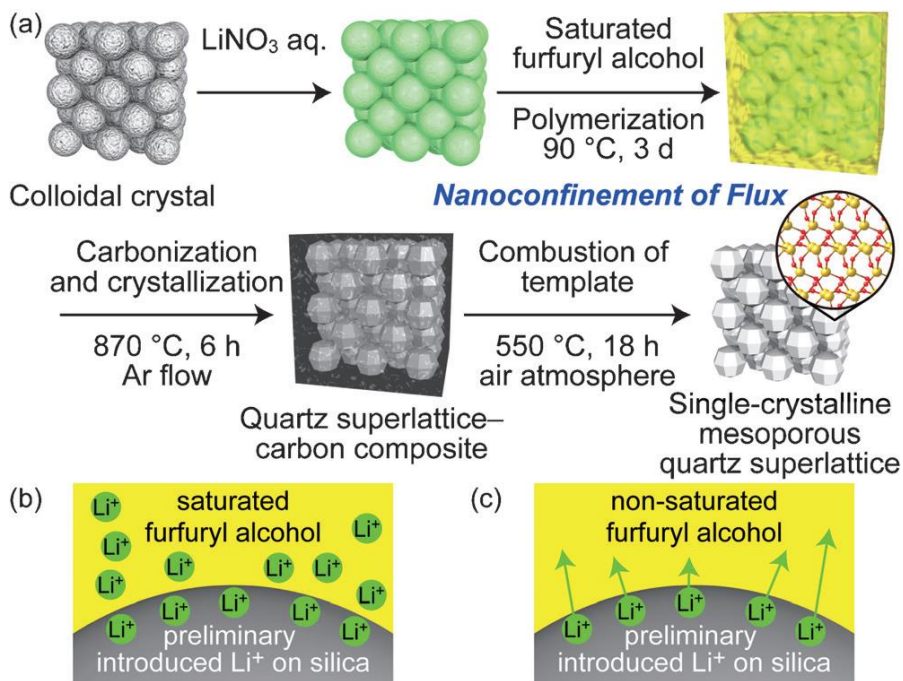


Figure 1-9. Preparation of a single-crystalline mesoporous quartz superlattice by crystallization of amorphous silica, which constitutes a colloidal crystal, by using a  $\text{Li}^+$  flux and a reinforcing carbon framework. Ref. 85.



In 2016, Kuroda and coworkers used a strong flux of  $\text{Li}^+$  to induce the crystallization from silica nanospheres constituting a colloidal crystal to single crystalline mesoporous quartz superlattice (Figure 1-9).<sup>85</sup> The mesopores are supported by a carbonized furfuryl alcohol polymer. The silica nanospheres have an average size of 32 nm, and this thickness of the nanospheres are strong enough from collapse during crystallization. The authors failed to maintain the mesostructure on KIT-6 mesoporous silica using the same method, and claimed that the thinness ( $\sim 2$  nm) and/or low density of the framework were the reason.<sup>85</sup> The work in Chapter 5 was inspired by Kuroda's work and it is believed this method would be effective for the crystallization of mesoporous aluminosilica materials, because the Al-SBA-15 material have relatively thick pore walls ( $\sim 7$  nm), which might be able to be retained with a shorter crystallization time. This work is described in detail in Chapter 5.

## 1.4 References

- 1 D. D. Ganji and S. H. H. Kachapi, *Application of nonlinear systems in nanomechanics and nanofluids : analytical methods and applications*, Elsevier, Oxford, UK, 2015.
- 2 E. M. Flanigen, R. W. Broach and S. T. Wilson, *Zeolites in Industrial Separation and Catalysis*, Wiley-VCH, Weinheim, Germany, 2010.
- 3 R. M. Barrer, *J. Chem. Soc.*, 1948, 2158.
- 4 R. M. Barrer, *J. Chem. Soc.*, 1948, 127.
- 5 R. M. Barrer and D. W. Riley, *J. Chem. Soc.*, 1948, 133.
- 6 T. B. Reed and D. W. Breck, *J. Am. Chem. Soc.*, 1956, **78**, 5972–5977.
- 7 R. M. Milton, American Chemical Society, 1989, pp. 1–10.
- 8 J. V. S. J. R. Anderson, K. Foger, T. Mole, R. A. Rajadhyaksha, *J. Catal.*, 1979, **58**, 114–130.
- 9 *Global Zeolite Market - Industry Analysis, Size, Share, Trends, Segment and Forecast 2014-2020*, 2016.
- 10 D. Kwon, B. G. Cha, Y. Cho, J. Min, E.-B. Park, S.-J. Kang and J. Kim, *Nano Lett.*, 2017, **17**, 2747–2756.

- 11 M. Doğan, H. Abak and M. Alkan, *Water. Air. Soil Pollut.*, 2008, **192**, 141–153.
- 12 T. C. Chandra, M. M. Mirna, Y. Sudaryanto and S. Ismadji, *Chem. Eng. J.*, 2007, **127**, 121–129.
- 13 I. Bautista-Toledo, M. A. Ferro-García, J. Rivera-Utrilla, A. C. Moreno-Castilla and F. J. V. Fernández, *Environ. Sci. Technol.*, 2005, 6246–6250.
- 14 H. Demiral, İ. Demiral, F. Tımsek and B. Karabacakođlu, *Chem. Eng. J.*, 2008, **144**, 188–196.
- 15 J. Wang, S. Kaskel, T. K. Bose, J. E. Fischer, Y. Gogotsi, A. Linares-Solano, A. Celzard, H. Saitoh, A. Celzard, Y. A. Kim, M. Endo, E. A. Stach and R. S. Ruoff, *J. Mater. Chem.*, 2012, **22**, 23710.
- 16 A. Demessence, D. M. D’Alessandro, M. L. Foo and J. R. Long, *J. Am. Chem. Soc.*, 2009, **131**, 8784–8786.
- 17 O. M. Yaghi, M. O’Keeffe, N. W. Ockwig, H. K. Chae, M. Eddaoudi and J. Kim, *Nature*, 2003, **423**, 705–714.
- 18 F.-X. Coudert, *Chem. Mater.*, 2015, **27**, 1905–1916.
- 19 H. Furukawa, K. E. Cordova, M. O’Keeffe and O. M. Yaghi, *Science (80-. )*, 2013, **341**, 1230444.
- 20 K. K. Tanabe and S. M. Cohen, *Chem. Soc. Rev.*, 2011, **40**, 498–519.
- 21 K. Sumida, K. Liang, J. Reboul, I. A. Ibarra, S. Furukawa and P. Falcaro, *Chem. Mater.*, 2017, **29**, 2626–2645.
- 22 S. R. Venna and M. A. Carreon, *Chem. Eng. Sci.*, 2015, **124**, 3–19.
- 23 A. P. Côté, A. I. Benin, N. W. Ockwig, M. O’Keeffe, A. J. Matzger and O. M. Yaghi, *Science (80-. )*, 2005, **310**, 1166–1170.
- 24 S. Das, P. Heasman, T. Ben and S. Qiu, *Chem. Rev.*, 2017, **117**, 1515–1563.
- 25 A. Li, R.-F. Lu, Y. Wang, X. Wang, K.-L. Han and W.-Q. Deng, *Angew. Chemie Int. Ed.*, 2010, **49**, 3330–3333.
- 26 Y. Xu, S. Jin, H. Xu, A. Nagai, D. Jiang, S. Brown, G. M. Veith, H. M. Luo, H. L. Liu, S. Dai, Y. Q. Yang, F. H. Li, S. B. Zhang, F. Huang and Y. G. Ma, *Chem. Soc. Rev.*, 2013, **42**, 8012.
- 27 T. Ben, H. Ren, S. Ma, D. Cao, J. Lan, X. Jing, W. Wang, J. Xu, F. Deng, J. M. Simmons, S. Qiu and G. Zhu, *Angew. Chemie Int. Ed.*, 2009, **48**, 9457–9460.
- 28 D. Yuan, W. Lu, D. Zhao and H.-C. Zhou, *Adv. Mater.*, 2011, **23**, 3723–3725.
- 29 P. Pandey, A. P. Katsoulidis, I. Eryazici, Y. Wu, M. G. Kanatzidis and S. T. Nguyen, *Chem. Mater.*, 2010, **22**, 4974–4979.
- 30 B. Li, X. Huang, L. Liang, B. Tan, J. Cortez, D. C. Sherrington, J. D. F. Ramsay, K. S. W. Sing, K. K. Unger, J. Simmons, S. Qiu, G. Zhu, J. Parker, A. Trewin, J. Bacsá, A. M. Z. Slawin, A. Steiner and A. I. Cooper, *J. Mater. Chem.*, 2010, **20**, 7444.
- 31 L. Chen, Y. Honsho, S. Seki and D. Jiang, *J. Am. Chem. Soc.*, 2010, **132**, 6742–6748.
- 32 R. Dawson, D. J. Adams, A. I. Cooper, S. Sircar, R. A. Pierotti, J. Rouquerol, T. Siemieniewska, A. I. Cooper, D. J. Adams, A. I. Cooper, A. I. Cooper and H.-C. Zhou, *Chem. Sci.*, 2011, **2**, 1173.
- 33 R. Dawson, F. Su, H. Niu, C. D. Wood, J. T. A. Jones, Y. Z. Khimyak and A. I. Cooper, *Macromolecules*, 2008, **41**, 1591–1593.

- 34 Y. Luo, B. Li, W. Wang, K. Wu and B. Tan, *Adv. Mater.*, 2012, **24**, 5703–5707.
- 35 S. Yuan, B. Dorney, D. White, S. Kirklin, P. Zapol, L. Yu, D.-J. Liu, N. L. Campbell, R. Kirk, E. Stockel and A. I. Cooper, *Chem. Commun.*, 2010, **46**, 4547.
- 36 M. Rose, N. Klein, I. Senkovska, C. Schrage, P. Wollmann, W. Böhlmann, B. Böhringer, S. Fichtner, S. Kaskel, J. M. Simmons, S. Qiu and G. Zhu, *J. Mater. Chem.*, 2011, **21**, 711–716.
- 37 H. Ren, T. Ben, E. Wang, X. Jing, M. Xue, B. Liu, Y. Cui, S. Qiu, G. Zhu, J. M. Simmons, S. Qiu and G. Zhu, *Chem. Commun.*, 2010, **46**, 291–293.
- 38 J. R. Holst, E. Stöckel, D. J. Adams and A. I. Cooper, *Macromolecules*, 2010, **43**, 8531–8538.
- 39 J. Weber, Q. Su, M. Antonietti and A. Thomas, *Macromol. Rapid Commun.*, 2007, **28**, 1871–1876.
- 40 J. Weber, M. Antonietti and A. Thomas, *Macromolecules*, 2008, **41**, 2880–2885.
- 41 Y. Liao, J. Weber and C. F. J. Faul, *Chem. Commun.*, 2014, **50**, 8002–8005.
- 42 J.-X. Jiang, F. Su, A. Trewin, C. D. Wood, H. Niu, J. T. A. Jones, Y. Z. Khimyak and A. I. Cooper, *J. Am. Chem. Soc.*, 2008, **130**, 7710–7720.
- 43 R. Dawson, A. Laybourn, R. Clowes, Y. Z. Khimyak, D. J. Adams and A. I. Cooper, *Macromolecules*, 2009, **42**, 8809–8816.
- 44 K. J. Msayib, N. B. McKeown, J. M. Huck, H. Wang, Z. Guo, W. Wang, D. Cao, M. Haranczyk, B. Smit, A. Walton, N. B. McKeown, D. J. Adams, S. G. Kazarian, C. E. Snape, T. C. Drage and A. I. Cooper, *J. Mater. Chem. A*, 2016, **4**, 10110–10113.
- 45 D. Wu, F. Xu, B. Sun, R. Fu, H. He and K. Matyjaszewski, *Chem. Rev.*, 2012, **112**, 3959–4015.
- 46 S. H. Strauss, *Chem. Rev.*, 1993, **93**, 927–942.
- 47 X. Yang, C. L. Stern and T. J. Marks, *J. Am. Chem. Soc.*, 1994, **116**, 10015–10031.
- 48 Z. Mazej and E. Goreshnik, *Eur. J. Inorg. Chem.*, 2015, **2015**, 1453–1456.
- 49 G. A. Olah, *J. Org. Chem.*, 2005, **70**, 2413.
- 50 S. Fischer, J. Schmidt, P. Strauch and A. Thomas, *Angew. Chemie - Int. Ed.*, 2013, **52**, 12174–12178.
- 51 J. F. Van Humbeck, M. L. Aubrey, A. Alsbaiee, R. Ameloot, G. W. Coates, W. R. Dichtel and J. R. Long, *Chem. Sci.*, 2015, **6**, 5499–5505.
- 52 Y. Du, H. Yang, J. M. Whiteley, S. Wan, Y. Jin, S. H. Lee and W. Zhang, *Angew. Chemie - Int. Ed.*, 2016, **55**, 1737–1741.
- 53 J. Roeser, D. Prill, M. J. Bojdys, P. Fayon, A. Trewin, A. N. Fitch, M. U. Schmidt and A. Thomas, *Nat. Chem.*, 2017, doi:10.1038/nchem.2771.
- 54 C. T. Kresge, M. E. Leonowicz, W. J. Roth, J. C. Vartuli and J. S. Beck, *Nature*, 1992, **359**, 710–712.
- 55 J. S. Beck, J. C. Vartuli, W. J. Roth, M. E. Leonowicz, C. T. Kresge, K. D. Schmitt, C. T.-W. Chu, D. H. Olson, E. W. Sheppard, S. B. Mccullen, J. B. Higgins and J. L. Schlenkert, *J. Am. Chem. Soc.*, 1992, **114**, 10834–10843.
- 56 X. Zhao, G. Q. Lu and G. J. Millar, *Ind. Eng. Chem. Res.*, 1996, **35**, 2075–2090.
- 57 D. Myers, *Surfactant Science and Technology. Second Edition*, VCH Weinheim. New York, 1992, vol. 96.
- 58 A. Z. ALOthman, *Materials (Basel)*, 2012, **5**, 2874–2902.

- 59 D. Zhao, J. Feng, Q. Huo, N. Melosh, G. H. Fredrickson, B. F. Chmelka and G. D. Stucky, *Science* (80-. ), 1998, **279**, 548.
- 60 D. Zhao, Q. Huo, J. Feng, B. F. Chmelka and G. D. Stucky, *J. Am. Chem. Soc.*, 1998, **120**, 6024.
- 61 Tae Wan Kim, F. Kleitz, B. Paul and R. Ryoo, *J. Am. Chem. Soc.*, 2005, **127**, 7601–7610.
- 62 Y. Yue, A. Gédéon, J.-L. Bonardet, N. Melosh, J.-B. D ’espinoze and J. Fraissard, *Chem. Commun.*, 1999, 1967–1968.
- 63 S. Wu, Y. Han, Y. C. Zou, J. W. Song, L. Zhao, Y. Di, S. Z. Liu and F. S. Xiao, *Chem. Mater.*, 2004, **16**, 486–492.
- 64 C. Li, Y. Wang, Y. Guo, X. Liu, Y. Guo, Z. Zhang, Y. Wang and Guanzhong Lu, *Chem. Mater.*, 2007, **19**, 173.
- 65 W. H. Zhang, J. Q. Lu, B. Han, M. J. Li, J. H. Xiu, P. L. Ying and C. Li, *Chem. Mater.*, 2002, **14**, 3413–3421.
- 66 Y. Li, W. Zhang, L. Zhang, Q. Yang, Z. Wei, Z. Feng and C. Li, *J. Phys. Chem. B*, 2004, **108**, 9739.
- 67 C. J. Brinker, *J. Non. Cryst. Solids*, 1988, **100**, 31–50.
- 68 A. Vinu, V. Murugesan, Winfried Böhlmann and Martin Hartmann, *J. Phys. Chem. B*, 2004, **108**, 11496.
- 69 P. Bhange, D. S. Bhange, S. Pradhan and V. Ramaswamy, *Appl. Catal. A Gen.*, 2011, **400**, 176–184.
- 70 S. Sumiya, Y. Oumi, T. Uozumi and T. Sano, *J. Mater. Chem.*, 2001, **11**, 1111–1115.
- 71 M. Gómez-Cazalilla, J. M. Mérida-Robles, A. Gurbani, E. Rodríguez-Castellón and A. Jiménez-López, *J. Solid State Chem.*, 2007, **180**, 1130–1140.
- 72 S. Wu, J. Huang, T. Wu, K. Song, H. Wang, L. Xing, H. Xu, L. Xu, J. Guan and Q. Kan, *Chinese J. Catal.*, 2006, **27**, 9–14.
- 73 H.-M. Kao, C.-C. Ting and S.-W. Chao, *J. Mol. Catal. A Chem.*, 2005, **235**, 200–208.
- 74 J. F. Bertone, J. Cizeron, R. K. Wahi, J. K. Bosworth and V. L. Colvin, *Nano Lett.*, 2003, **3**, 655–659.
- 75 M. Hosaka, *J. Cryst. Growth*, 1991, **112**, 291–293.
- 76 X. Jiang, Y. Jiang and C. J. Brinker, *Chem. Commun.*, 2011, **47**, 7524.
- 77 M. Mandal and K. Landskron, *Acc. Chem. Res.*, 2013, **46**, 2536–2544.
- 78 P. Mohanty, Y. Fei and K. Landskron, *J. Am. Chem. Soc.*, 2009, **131**, 9638–9639.
- 79 P. Mohanty, B. Kokoszka, C. Liu, M. Weinberger, M. Mandal, V. Stagno, Y. Fei and K. Landskron, *Microporous Mesoporous Mater.*, 2012, **152**, 214–218.
- 80 P. Mohanty, D. Li, T. Liu, Y. Fei and K. Landskron, *J. Am. Chem. Soc.*, 2009, **131**, 2764–2765.
- 81 M. Mandal, A. S. Manchanda, C. Liu, Y. Fei and K. Landskron, *RSC Adv.*, 2016, **6**, 7396–7402.
- 82 P. Armand, A. Lignie, M. Beaurain and P. Papet, *Crystals*, 2014, **4**, 168–189.
- 83 A. Carretero-Genevriér, M. Gich, L. Picas, J. Gazquez, G. L. Drisko, C. Boissiere, D. Grosso, J. Rodriguez-Carvajal and C. Sanchez, *Science* (80-. ), 2013, **340**, 827.

- 84 G. L. Drisko, A. Carretero-Genevri r, A. Perrot, M. Gich, J. G zquez, J. Rodriguez-Carvajal, L. Favre, D. Grosso, C. Boiss re and C. Sanchez, *Chem. Commun.*, 2015, **51**, 4164–4167.
- 85 T. Matsuno, Y. Kuroda, M. Kitahara, A. Shimojima, H. Wada and K. Kuroda, *Angew. Chemie - Int. Ed.*, 2016, **55**, 6008–6012.

## Chapter 2

# Synthesis of anionic porous organic frameworks with phosphate functional groups (PA-POFs)

## 2.1 Design of phosphorus-based anionic porous organic frameworks

As described in Chapter 1, the term “weakly coordinating anionic porous organic frameworks (WCA-POFs)” combines weakly coordinating anions (WCAs) and porous organic frameworks (POFs). Compared with neutral POFs, WCA-POFs have many novel properties due to the combination of porosity and weakly coordinating character. In order to make weakly coordinated anionic porous organic frameworks, hexa-coordinated phosphorus  $[P(O_2Ar)_3]^-$  (Ar = Aryl) was designed as nodes to be incorporated into the framework. At the outset of the work in WCA-POFs in this dissertation, no such materials were known. A few examples of WCA-POFs were published while the work in this dissertation was underway.<sup>1-3</sup> However, among the published examples, only tetra-coordinated borons are used as the carriers of formal negative charges, which are distinctive from the research in this dissertation.

The chemistry of phosphates with hexacoordinated phosphorus became prosperous since Allcock reported that the reaction of phosphonitrilic chlorides with pyrocatechol led to the unexpected tris(benzenediolato)phosphate anions, in which the central phosphorus

atom was coordinated by six oxygen atoms.<sup>4-7</sup> Figure 2-1 lists a few examples of phosphate ions with hexacoordinated P atoms. Compound 1 is composed of three identical benzenediolato ligands, compound 2 consists of three bidentate bisphenylidene ligands, compounds 3 and 4 are composed of both benzenediolato and bisphenylidene ligands in different ratios, whereas compounds 5 and 6 contain both P-C bonds and P-O bonds on the same chelating ligand. The very different and complicated synthesis strategies for compounds 2-6 are beyond the scope of this dissertation because each compound requires a different order of addition of chelating ligands as well as a proper order of P-C and P-O bond formation.

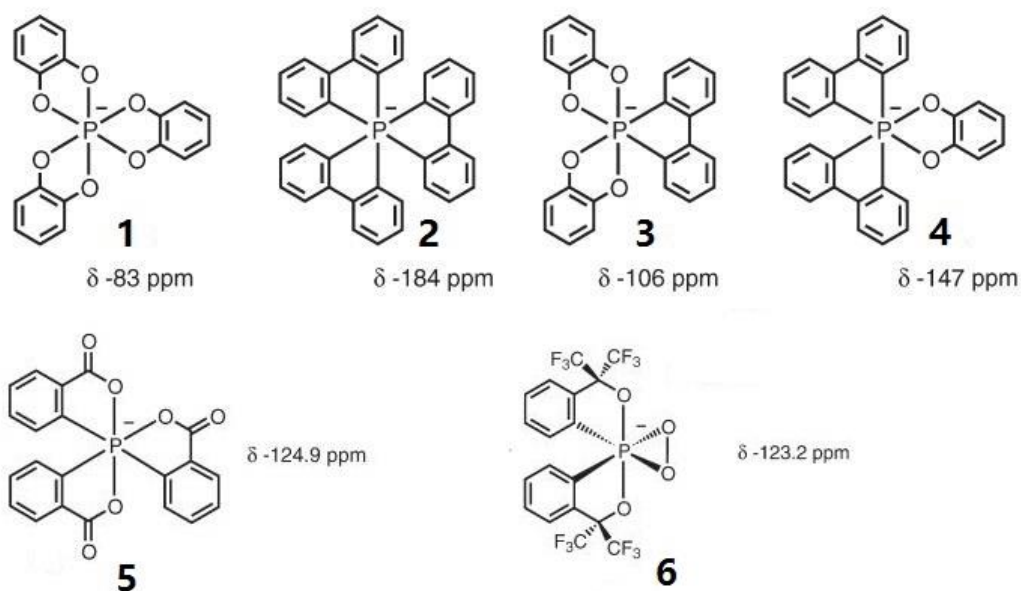


Figure 2-1. Selection of hexacoordinated phosphate anions. Ref. 4–12.

For the synthesis of anionic phosphates containing three identical dioxo ligands around the phosphorus similar to compound 1, a simple synthesis protocol was developed that involved the one-time addition of 3 equivalents of bidentate ligands to  $\text{PCl}_5$  to produce the hexacoordinated phosphate anions.<sup>13</sup> Aromatic 1,2-diols such as catechol are especially

good ligands because the chelate effect can be exploited. The reaction can be easily driven to completion by the addition of a base to the reaction mixture, which promotes the formation of hexa-coordinated P from penta-coordinated P. As shown in Figure 2-2, 3 equivalents of aromatic 1,2-diols are added towards a solution of  $\text{PCl}_5$  to yield a penta-coordinated phosphorus species with the release of five equivalents of  $\text{HCl}$  gas. Later, a base (amine, lithium salts, *etc.*) is added to the reaction mixture to afford a hexa-coordinated phosphate anion.

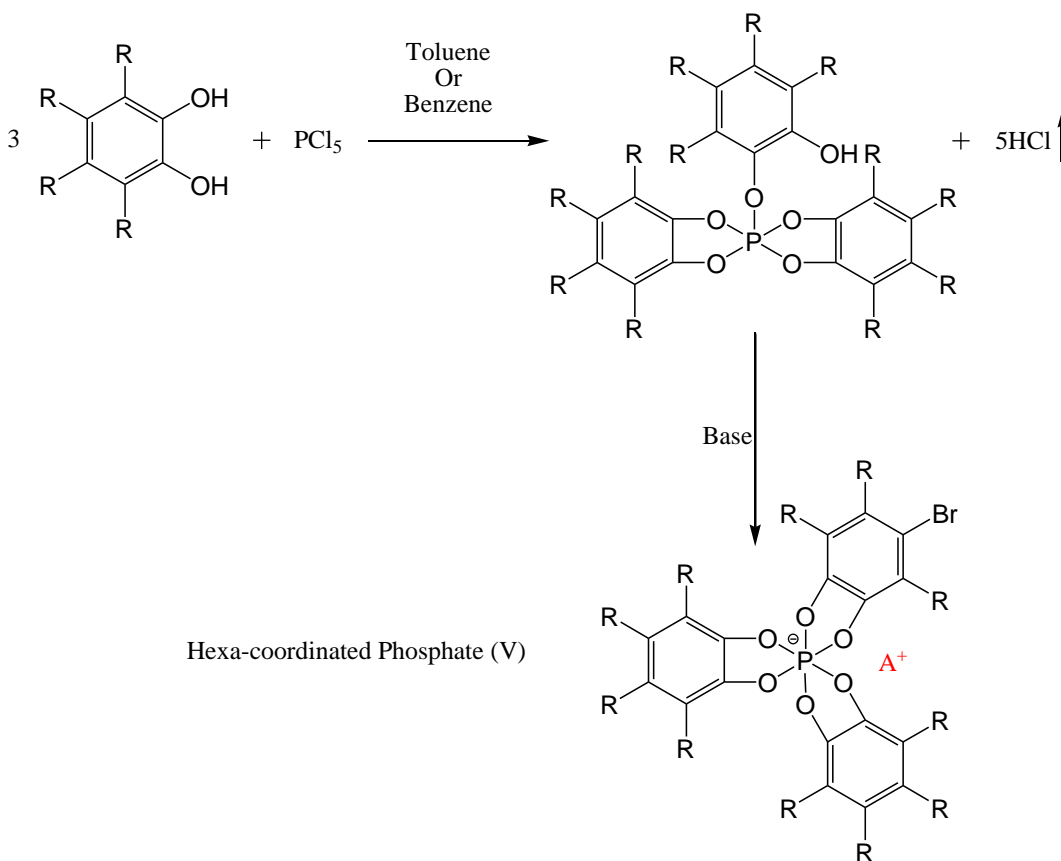


Figure 2-2. Schematic synthesis of hexacoordinated phosphorus species.  $\text{A}^+$  represents the cation to balance the negative charge on the WCA.



As discussed in the first Chapter, one-pot syntheses and two-step syntheses are the two strategies that are currently applied to the synthesis of WCA-POFs. In the one-pot synthesis, the anionic nodes are formed as connections during polymerization.

A direct synthetic route was first proposed between the reaction of  $\text{PCl}_5$  with monomer that has multiple aromatic ortho-diol sites such as 1,2,4,5-tetrahydroxyl benzene or 2,3,6,7,10,11-hexahydroxytriphenylene, hoping to obtain a network of WCA-POF, as shown in Figure 2-3.

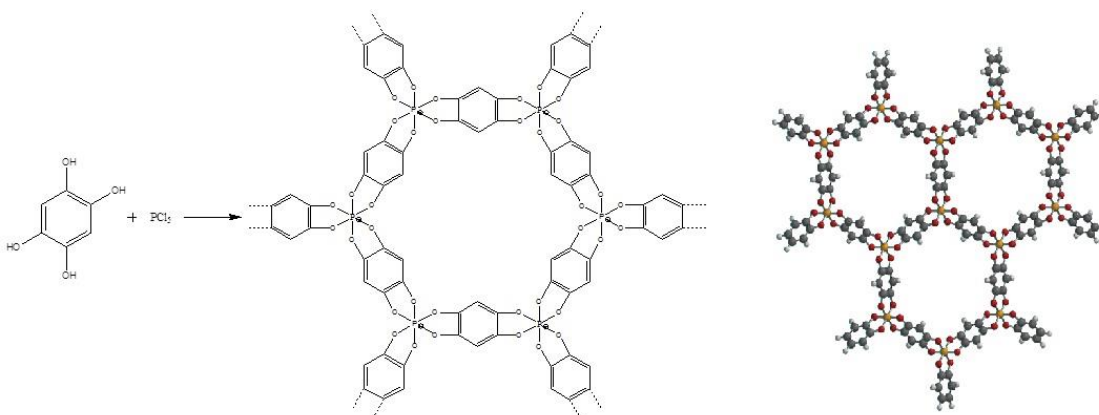


Figure 2-3. Proposed synthesis of 1,2,4,5-tetrahydroxy benzene and  $\text{PCl}_5$  for the construction of a two-dimensional porous framework.

Efforts were made to realize the synthesis shown in Figure 2-3. In this synthesis,  $\text{PCl}_5$  and 1,2,4,5-tetrahydroxy benzene were mixed in a solvent at elevated temperatures. After 1-3 days, a base (triethylamine/n-butyl lithium) was added to the reaction mixture in order to promote the formation of hexa-coordinated phosphorus from penta-coordinated phosphorus complex. The reaction conditions were systematically adjusted with the expectation to yield the desired WCA-POF, which included the use of different solvents such as benzene, toluene or mesitylene; the reaction temperatures that span from room temperature to 150 °C; and the varied composition of the starting materials. However, non-

porous materials were obtained as shown in Figure 2-4. From the  $^{31}\text{P}$  solid state NMR shown in Figure 2-5, only a small amount of P could be assigned to hexa-coordinated phosphorus (-81.3 ppm), while the majority of P existed in the product as tetra-coordinated phosphate (1.3 ppm). Similar results were observed when 2,3,6,7,10,11-hexahydroxytriphenylene reacted with  $\text{PCl}_5$ . The failure of the direct synthesis might be due to the high reactivity of  $\text{PCl}_5$ . Because  $\text{PCl}_5$  reacts with many organic solvents, only very inert solvents such as benzene and toluene could be used, which restricted the solubility of 1,2,4,5-tetrahydroxyl benzene or 2,3,6,7,10,11-hexahydroxytriphenylene, and might not be preferential for the polymerization.

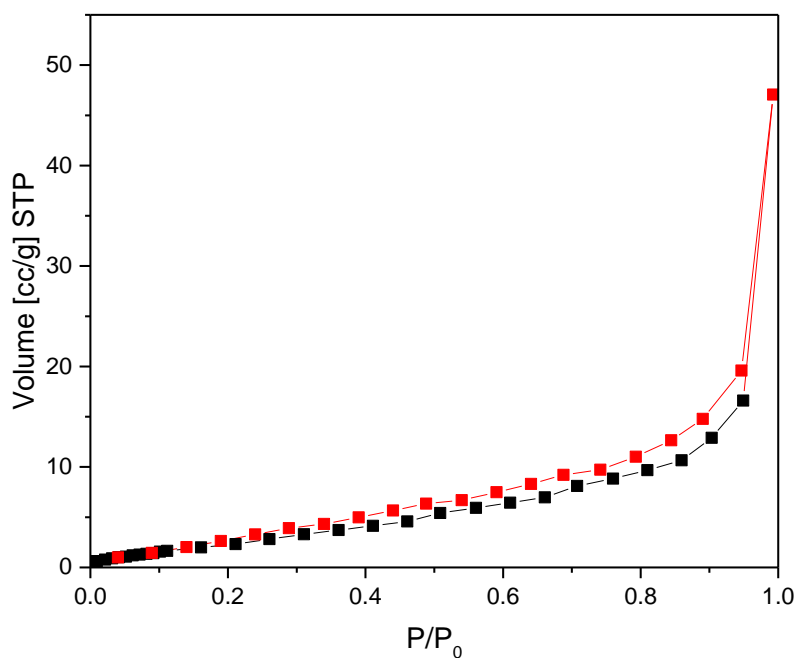


Figure 2-4. Representative  $\text{N}_2$  sorption isotherm of the products from the reaction between 1,2,4,5-tetrahydroxy benzene and  $\text{PCl}_5$ .

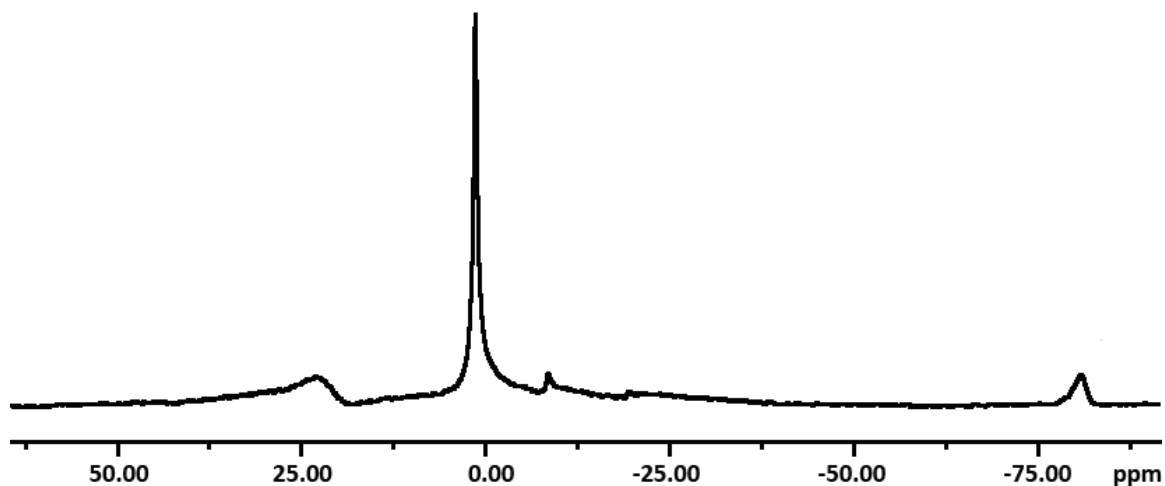


Figure 2-5. Representative  $^{31}\text{P}$  solid state NMR spectrum of the products from the reaction between 1,2,4,5-tetrahydroxy benzene and  $\text{PCl}_5$ .

Therefore, the synthesis was redesigned into a two-step synthesis strategy. In this strategy, a hexa-coordinated phosphorus-based weakly coordinating anion ( $[\text{P}(\text{O}_2\text{Ar})_3]^-$ ) was synthesized from  $\text{PCl}_5$  and a R-catechol as the first step. In the second step, the P-WCA was polymerized with a carefully chosen linker to form a porous structure with the retention of  $[\text{P}(\text{O}_2\text{Ar})_3]^-$  structure. The reaction conditions for the polymerization step are more flexible using this method because  $[\text{P}(\text{O}_2\text{Ar})_3]^-$  ions have reasonable stability and a greater range of solvents can be chosen in the second step.

The following synthetic route was therefore designed. An aryl bromide, 4-bromocatechol, was selected because it had peripheral bromine functional groups on the phenyl ring. Aryl bromides are known to have strong reactivity to cross-couple with other ligands through various reactions, such as through Suzuki cross-coupling reactions with boronic acid, Sonogashira coupling reactions with phenylacetylene, Yamamoto coupling reactions with aryl halide, *etc.* In this work, the Yamamoto coupling reaction was used to

polymerize the  $[P(O_2Ar)_3]$  monomers. The synthesis of the first step and the second step are discussed in sections 2.2 and 2.3.

## 2.2 Synthesis of TTBP and LTBP

The synthesis of the monomers was carried out using the protocol from Ref. 14 with minor changes. Triethylammonium [tris(4-bromocatecholate)] phosphate (V) (TTBP) and lithium [tris(4-bromocatecholate)] phosphate (V) (LTBP) were synthesized as shown in Figure 2-6.

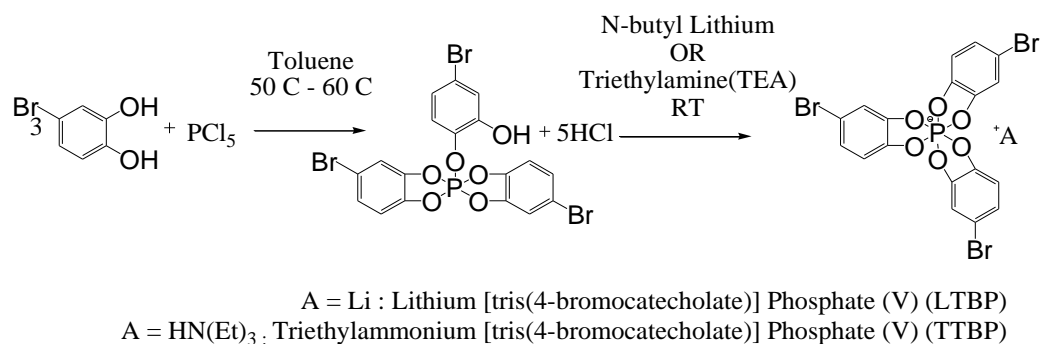


Figure 2-6. Synthesis scheme of TTBP and LTBP.

The experiment details are shown as following.

A solution of phosphorus pentachloride (4.4 mmol, 918 mg, Sigma Aldrich) in anhydrous toluene (30 mL, Acros Organics) was added into a three-neck flask with nitrogen gas flowing. The flask was heated and stirred in an oil bath at 50 °C. Into the flask 4-bromocatechol (13.2 mmol, 2.5 g, TCI) was added while nitrogen flushing. The resulting mixture was kept refluxing and stirring for 24 hours before being cooled gradually to room temperature. Triethylamine (0.5 mL, Fisher Scientific) or n-Butyl lithium (1.6 M in

hexanes) (4.4 mmol, 2.75 mL, Sigma Aldrich) was then added dropwise into the reaction mixture *via* a syringe for the synthesis of TTBP or LTBP, respectively. Upon adding the base, the clear orange solution turned white or grey cloudy immediately, for the synthesis of TTBP or LTBP, respectively. The reaction mixture was stirred for 24 hours after which the mixture was vacuum filtered. The solid was washed several times with toluene.

TTBP was obtained as a white solid powder in 92% yield (2.8 g).  $^1\text{H}$  NMR (acetone- $d_6$ ):  $\delta$  (ppm) = 1.41 (triplet, 9H,  $J = 2.3$  Hz), 2.90 (singlet, 1H), 3.46 (quartet, 6H,  $J = 2.3$  Hz), 6.51 (doublet, 3H,  $J = 7.6$  Hz), 6.74 (doublet, 3H,  $J = 7.6$  Hz), 6.76 (singlet, 3H).  $^{13}\text{C}$  NMR (acetone- $d_6$ ):  $\delta$  (ppm) = 8.1, 46.8, 109.2, 109.8, 111.8, 120.7, 145.0, 146.9.  $^{31}\text{P}$  NMR (acetone- $d_6$ ):  $\delta$  (ppm) = -80.5.

LTBP was obtained as a silver grey solid powder in 87% yield (2.3 g).  $^1\text{H}$  NMR (acetone- $d_6$ ):  $\delta$  (ppm) = 6.50 (doublet, 3H,  $J = 7.7$  Hz), 6.73 (doublet, 3H,  $J = 7.7$  Hz), 6.76 (singlet, 3H).  $^{13}\text{C}$  NMR (acetone- $d_6$ ):  $\delta$  (ppm) = 109.2, 109.8, 111.8, 120.7, 145.1, 147.0.  $^{31}\text{P}$  NMR (acetone- $d_6$ ):  $\delta$  (ppm) = -80.3.  $^7\text{Li}$  NMR (acetone- $d_6$ ):  $\delta$  (ppm) = 0.67.

The liquid state NMR spectra of TTBP and LTBP shown in Figure 2-7 to 2-11 confirm the correct structures of monomers for the copolymerization in the second step. Especially, the clean spectra of  $^{31}\text{P}$  NMR with chemical shifts located at  $\sim -80$  ppm of both TTBP and LTBP are characteristic for  $[\text{P}(\text{O}_2\text{C}_6\text{R}_4)_3]^-$ . The preparation of triethylammonium ion in TTBP is to investigate the influence of a large organic cation on the porosity of the resulting polymer, which is discussed in detail in chapter 2.3.

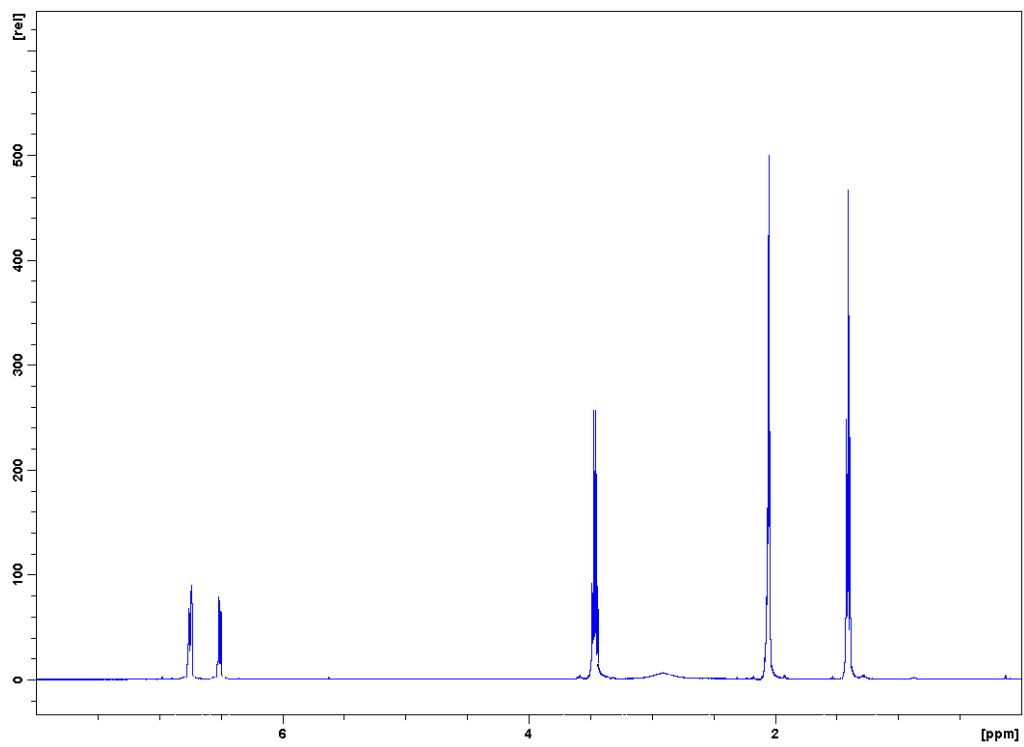


Figure 2-7.  $^1\text{H}$  NMR spectrum of TTBP.

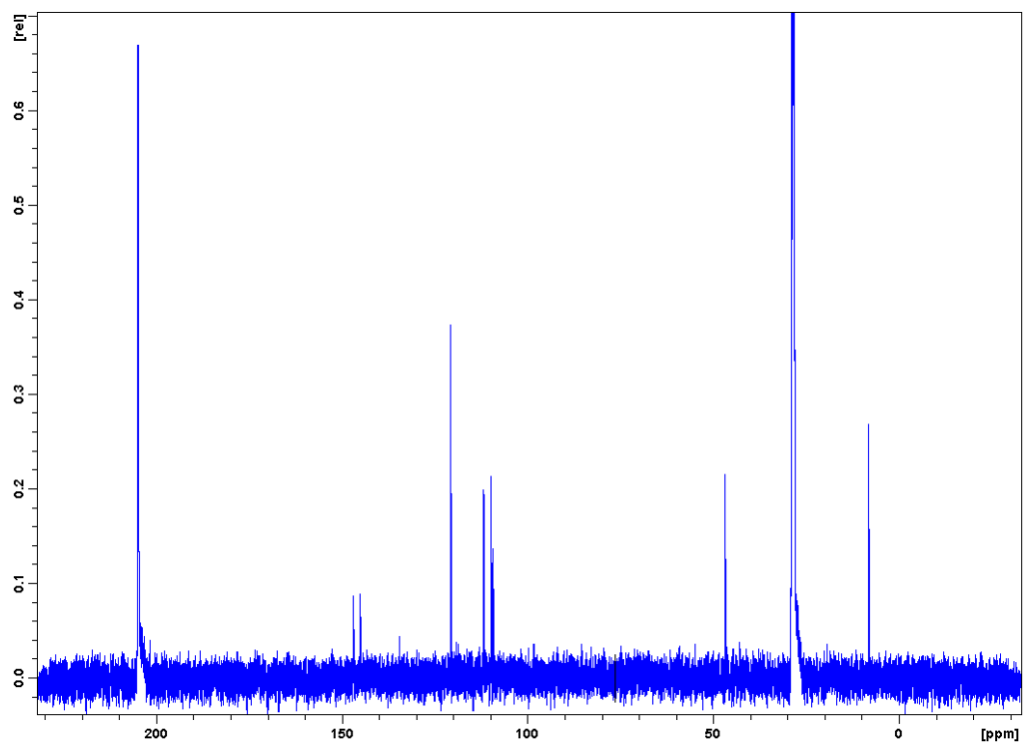


Figure 2-8.  $^{13}\text{C}$  NMR spectrum of TTBP.

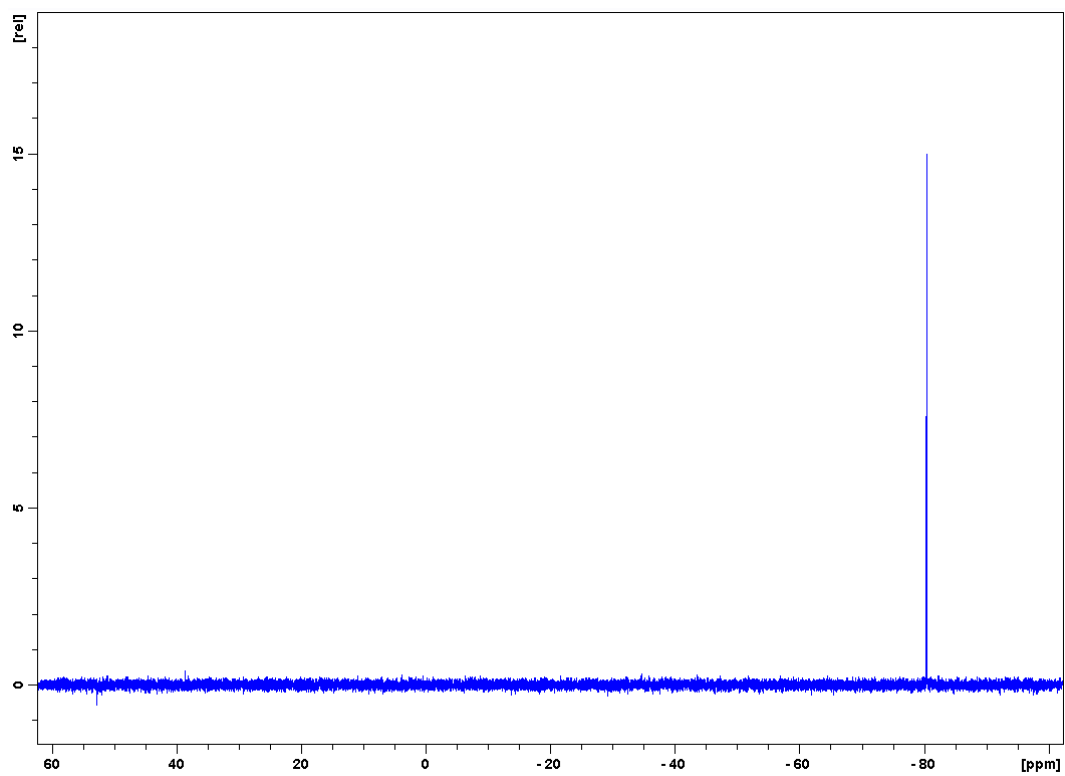


Figure 2-9.  $^{31}\text{P}$  NMR spectrum of TTBP.

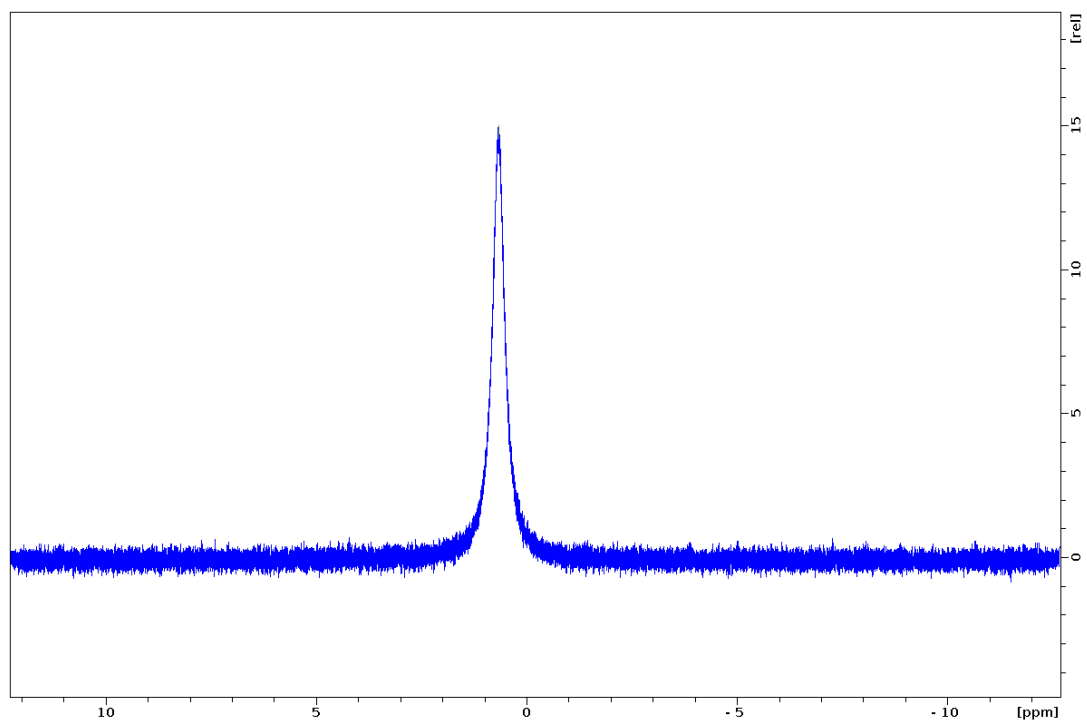


Figure 2-10.  $^7\text{Li}$  NMR spectrum of LTBP.

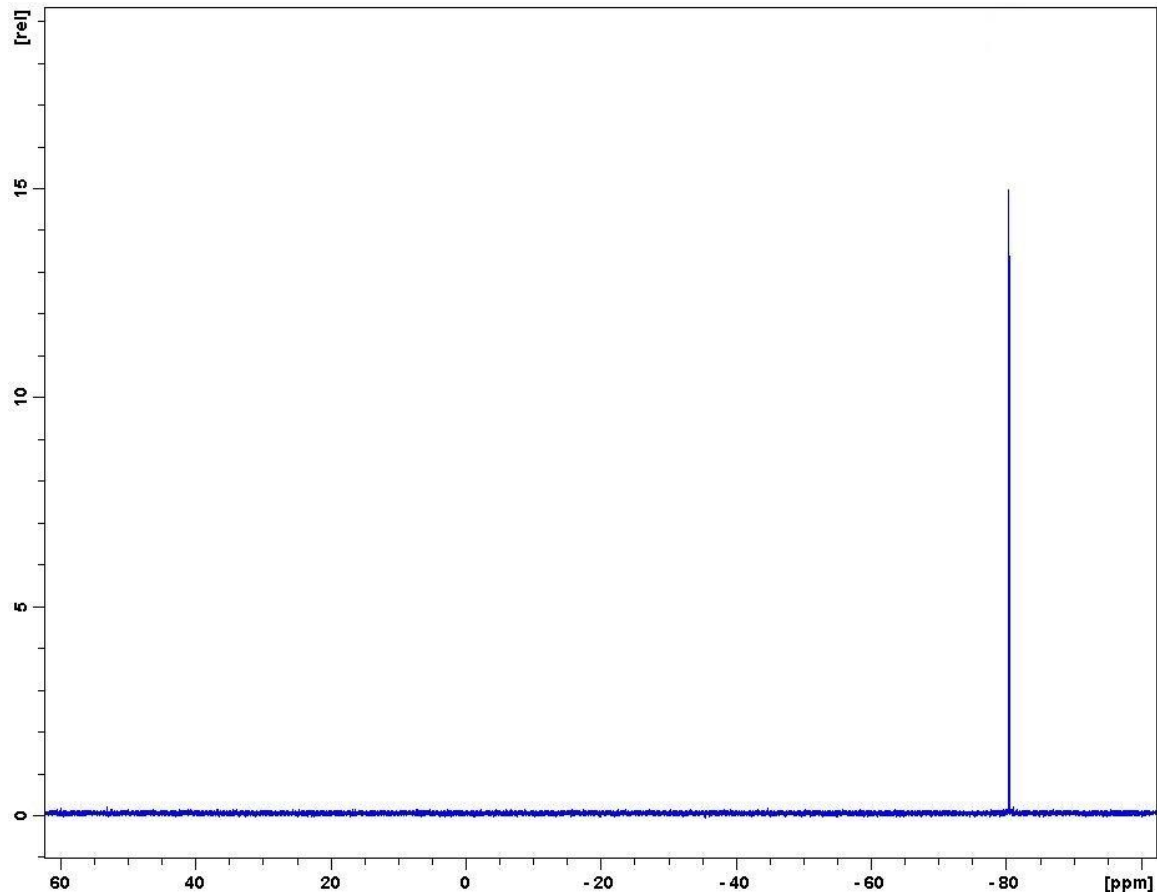


Figure 2-11. <sup>31</sup>P NMR spectrum of LTBP.

### 2.3 Synthesis of P-WCA-POFs and PA-POFs

The first attempt was to polymerize TTBP alone in a Yamamoto coupling reaction. The polymerization succeeded and P was found to have a chemical shift of -80 ppm (Figure 2-12), which is characteristic for  $[P(\text{catecholate})_3]^-$  type hexacoordinated P.<sup>15</sup> However, the reaction products proved to have a surface area of only  $88 \text{ m}^2 \text{ g}^{-1}$  according to  $\text{N}_2$  adsorption (Figure 2-13). The cations inside the polymer should only interact very weakly with the anionic framework and be easily exchangeable by another cation. Therefore, it was attempted to exchange the triethylammonium ions in the framework by sodium ions.



However, the absence of Na signal in EDX after ion-exchange showed that the cations were not ion-exchangeable (Figure 2-14). The reason for the failure of the ion-exchange may be the small surface area and/or the closed pores.

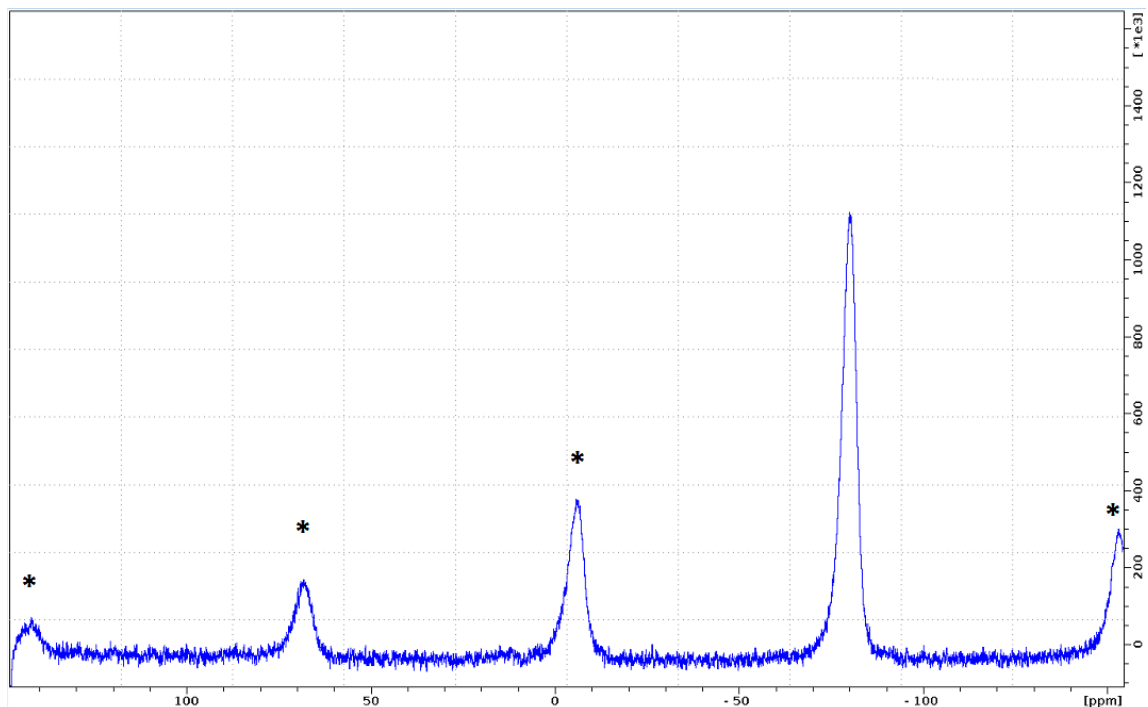


Figure 2-12.  $^{31}\text{P}$  solid state NMR spectrum of polymerized TTBP. Asterisks (\*) indicate peaks arising from spinning side bands.

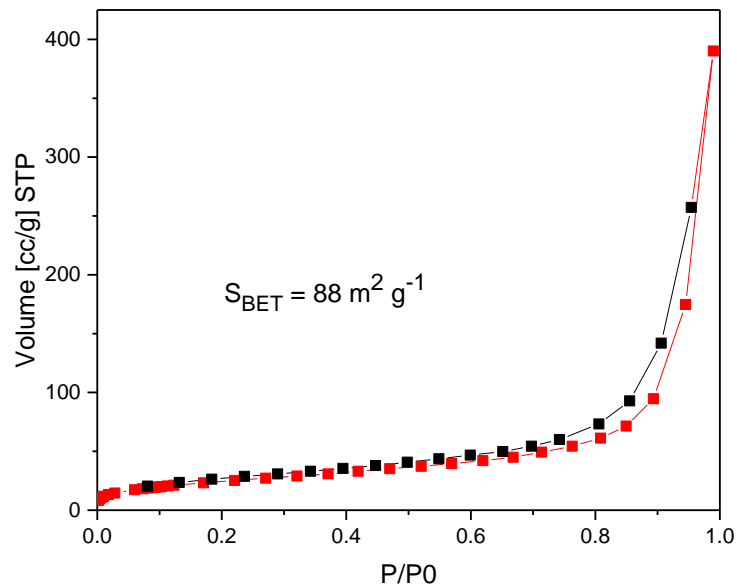


Figure 2-13. Nitrogen adsorption (red squares) and desorption (black squares) isotherms of polymerized TTBP measured at 77K.

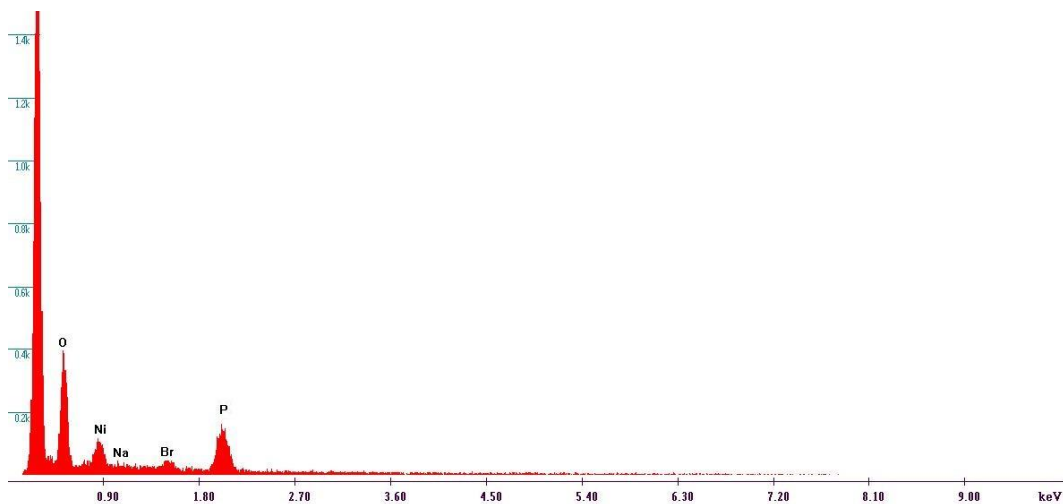


Figure 2-14. EDX spectrum of polymerized TTBP after ion exchange in NaCl solution. No Na can be found in the EDX spectrum shows that the cation was not exchangeable.

In a revised strategy TTBP was co-polymerized with a commercially available building block which was used to build PAF-1,<sup>16</sup> tetrakis(4-bromophenyl) methane (TBPM), to form a phosphorus-based WCA-POF (P-WCA-POF-1), Figure 2-15.

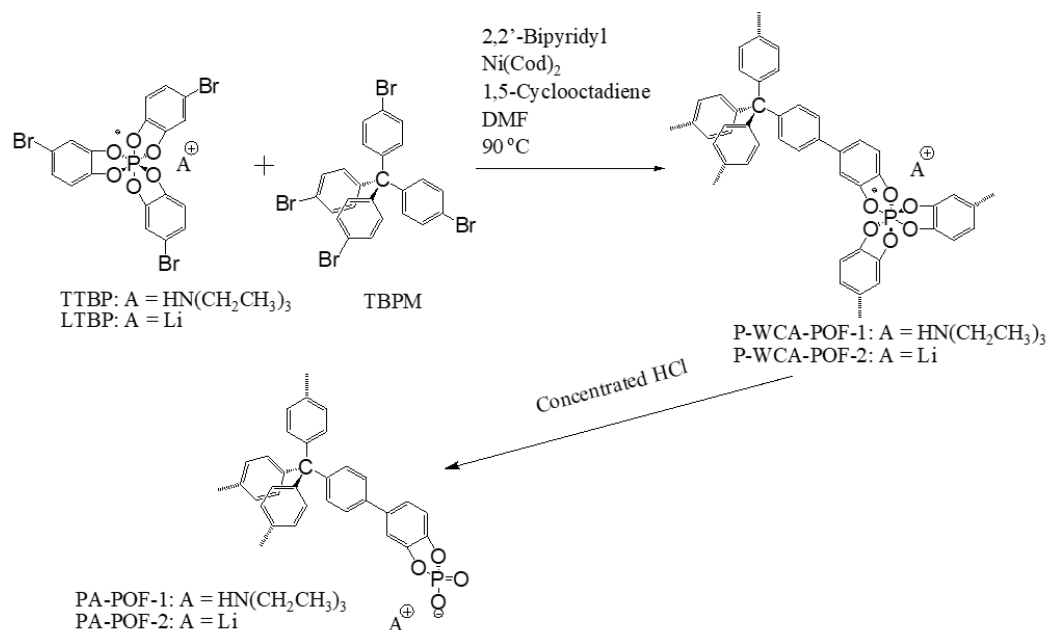


Figure 2-15. Synthesis of P-WCA-POFs and PA-POFs through Ni-promoted Yamamoto coupling reactions.

The resulting P-WCA-POF-1 was expected to have a high surface area because it was known that TBPM formed PAF-1 which had a surface area as high as 5,600 m<sup>2</sup> g<sup>-1</sup>.<sup>16</sup> Indeed, the surface area was much improved when TTBP and TBPM were co-polymerized in a molar ratio of 1:1 showing values of 434 m<sup>2</sup> g<sup>-1</sup> according to N<sub>2</sub> adsorption (Figure 2-16) and <sup>31</sup>P MAS NMR demonstrated that the [P(O<sub>2</sub>Ar)<sub>3</sub>]<sup>-</sup> octahedra remained intact during the polymerization (Figure 2-17), however, the cations were still not ion-exchangeable. The reason for this may be that the large triethylammonium ions are located within the pore walls and are tightly surrounded by organic polymer. Furthermore, EDX analysis of the material showed substantial amounts of Ni inside the material (Figure 2-18) and it might be that the trapped Ni coupling agent blocks the pore openings which prevents ion-exchange. Concentrated hydrochloric acid is usually used to quench the reaction mixture in Yamamoto reactions for the removal of Ni, and thus it was attempted to remove the Ni

from the material by washing it with concentrated HCl. It was found that the HCl did remove almost all Ni (Figure 2-19), however  $^{31}\text{P}$  MAS NMR (Figure 2-20) showed that the hexa-coordinated  $[\text{P}(\text{O}_2\text{Ar})_3]^-$  units were transformed into  $\text{PO}_4$  phosphate functional groups (Figure 2-15 and 2-20). The acid treated material (here-after named PA-POF-1) showed a type I  $\text{N}_2$  isotherm and an apparent BET surface area of  $478 \text{ m}^2 \text{ g}^{-1}$  (Figure 2-21). The material was ion-exchangeable by  $\text{Na}^+$  (Figure 2-22) according to EDX, suggesting that the pores are now open, which is possibly because of two reasons: firstly, the Ni impurities were removed; secondly, more pores may be created when P-O bonds break and ligands are etched away by the acid. Although PA-POF-1 did not have the desired  $\text{PO}_6$  building unit, it was still worthy of further investigation because of its high surface area and ion-exchange properties.

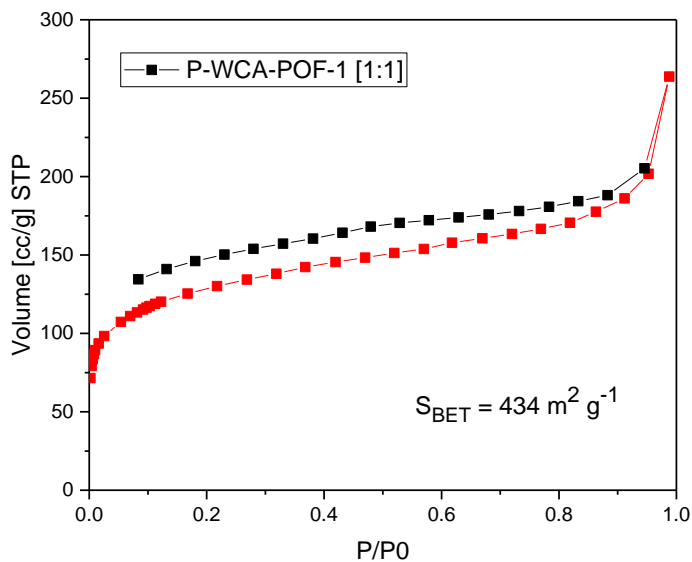


Figure 2-16. Nitrogen adsorption (red squares) and desorption (black squares) isotherms of P-WCA-POF-1 [1:1] measured at 77K.

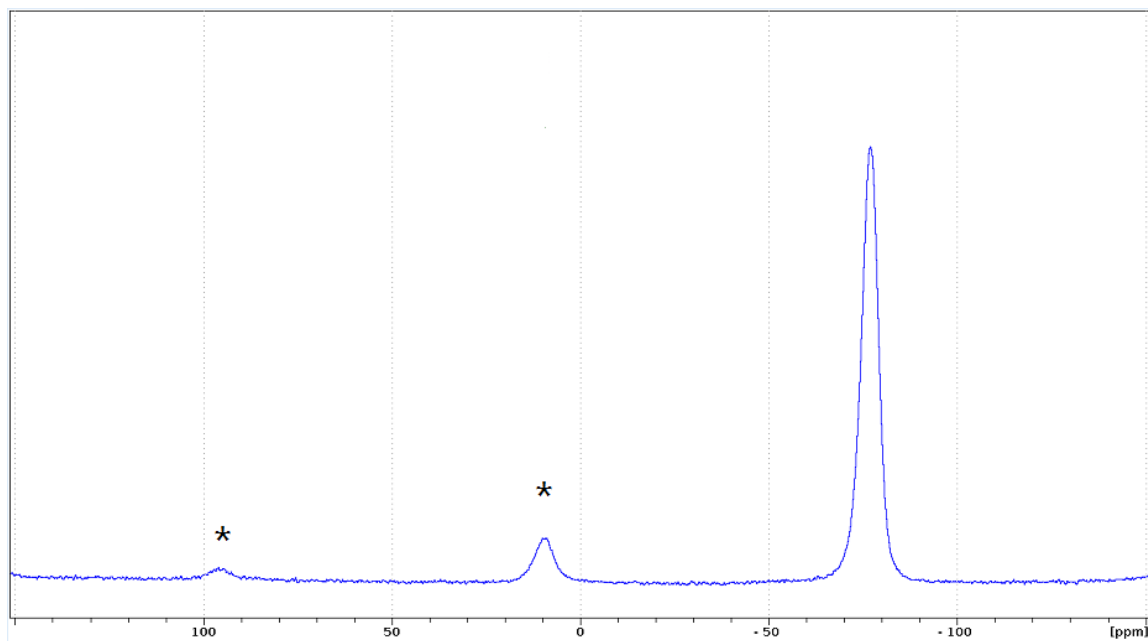


Figure 2-17.  $^{31}\text{P}$  solid state NMR spectrum of P-WCA-POF-1 [1:1]. Asterisks (\*) indicate peaks arising from spinning side bands.

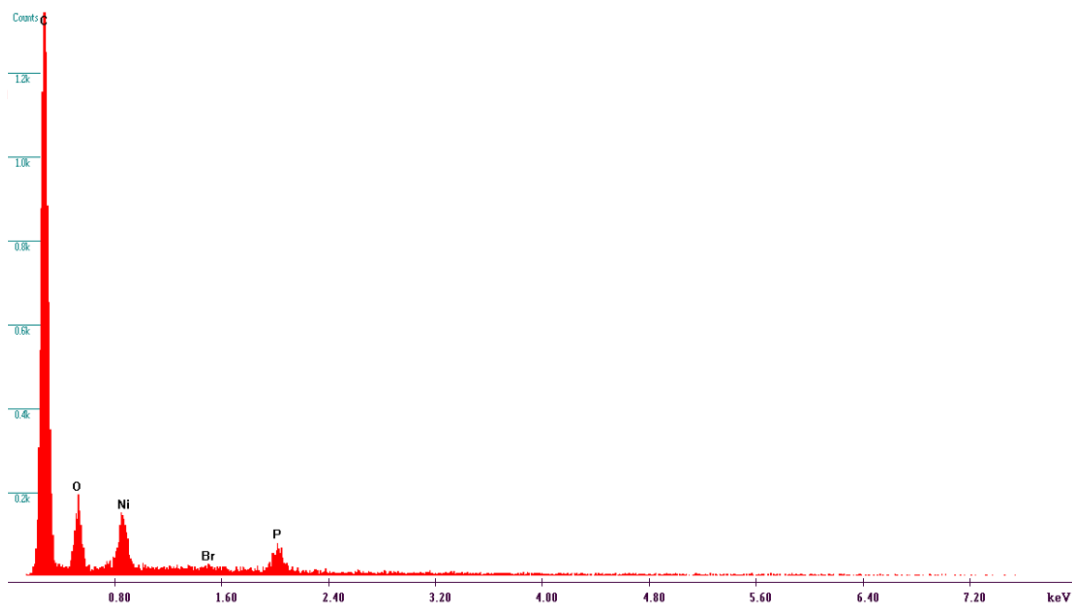


Figure 2-18. EDX spectrum of P-WCA-POF-1 [1:1].

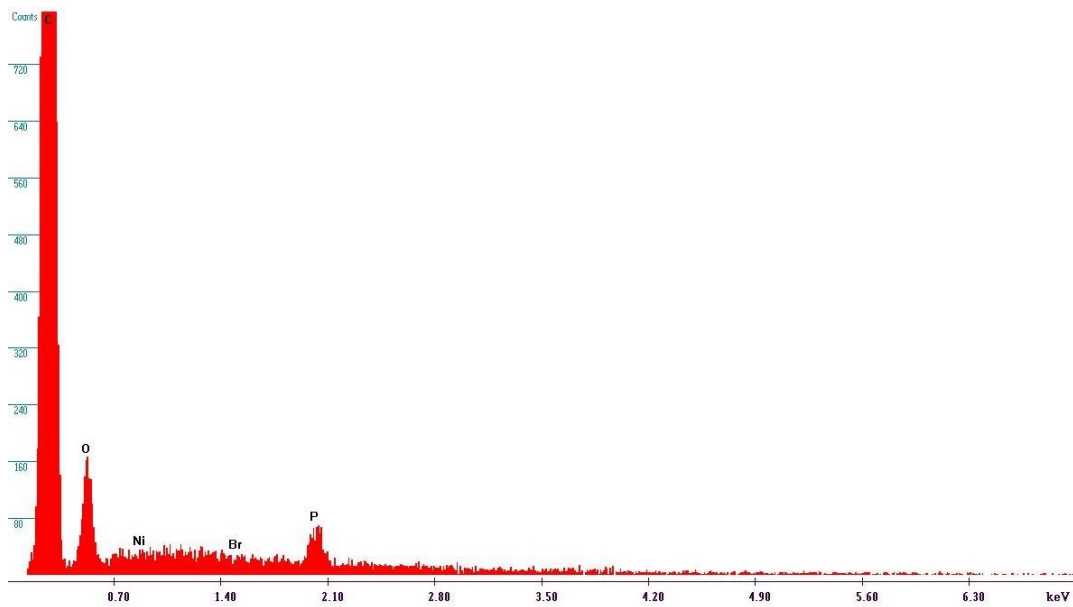


Figure 2-19. EDX spectrum of P-WCA-POF-1 [1:1] after treatment of concentrated HCl.

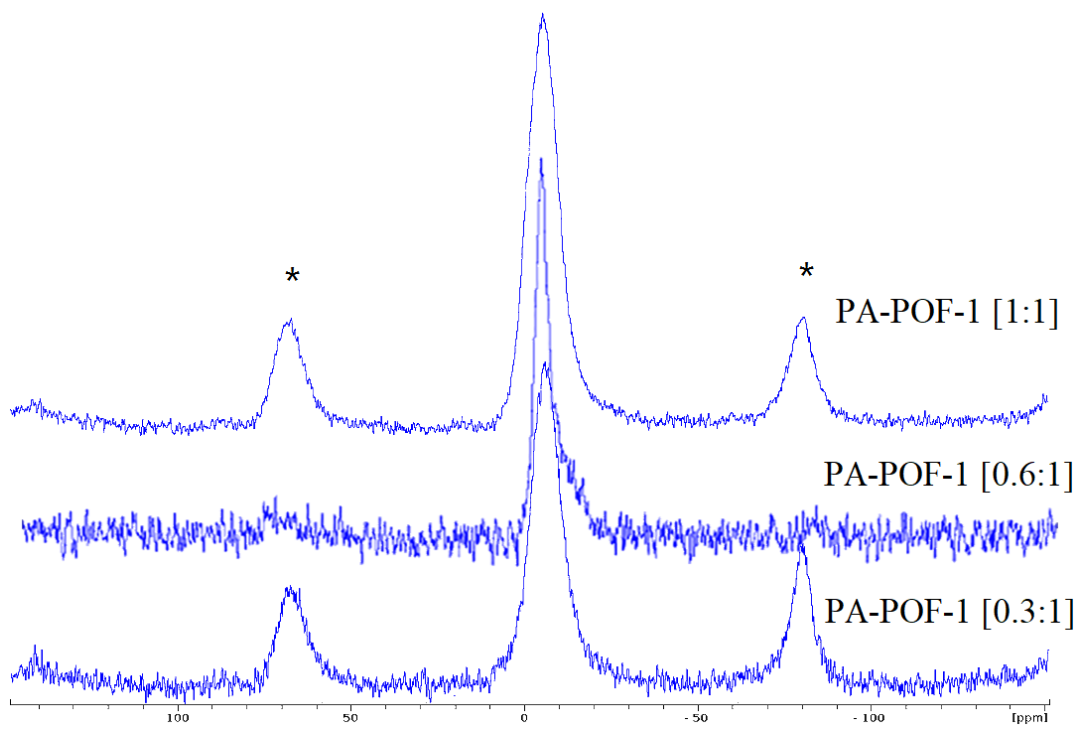


Figure 2-20.  $^{31}\text{P}$  solid state NMR spectrum of PA-POF-1s. Asterisks (\*) indicate peaks arising from spinning side bands.

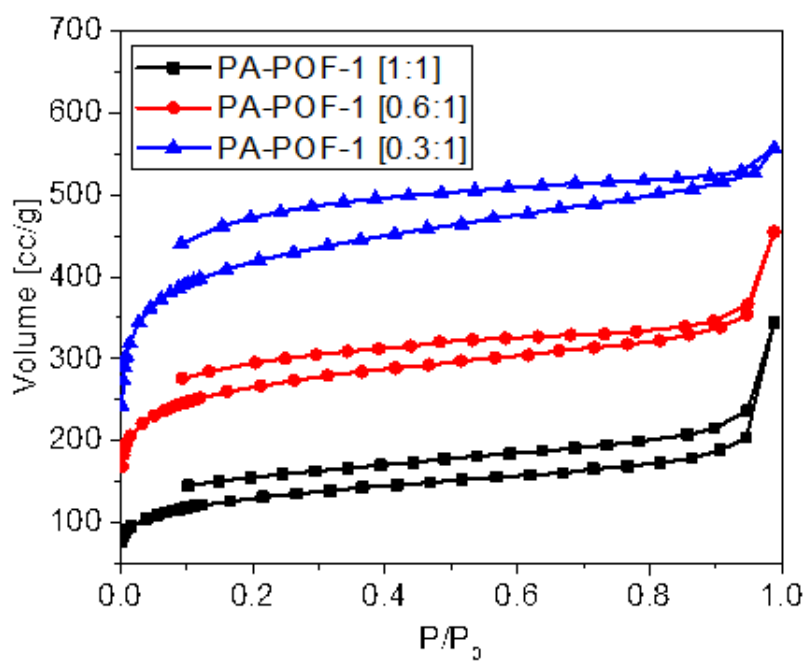


Figure 2-21. Nitrogen sorption isotherms of PA-POF-1s. The curves are offset for better visualization.

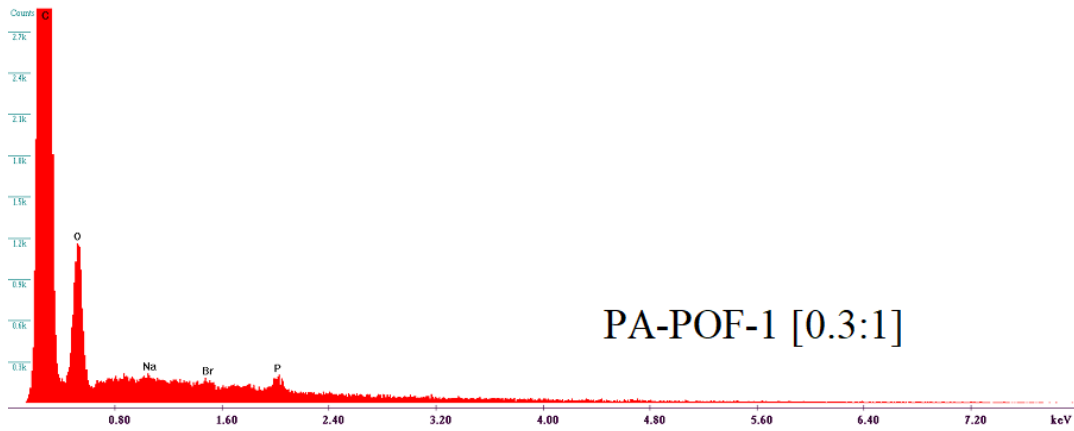
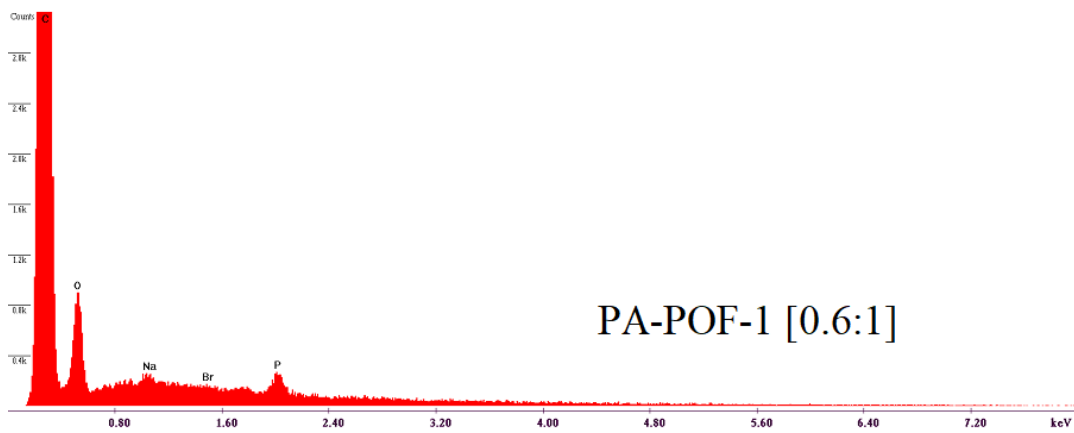
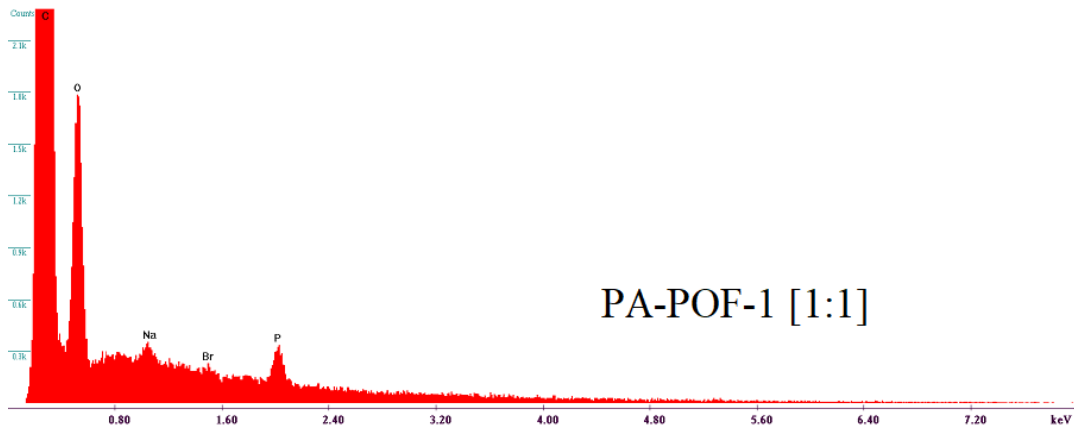


Figure 2-22. EDX spectrum of PA-POF-1s after ion exchange in NaCl solution.



In subsequent experiments the TTBP:TBPM molar ratio was decreased in the hope that a greater portion of TBPM in the polymer would further increase the surface area. Analysis of the N<sub>2</sub> sorption isotherm of PA-POF-1 [TTBP:TBPM] materials by the Brunauer-Emmett-Teller (BET) method within the relative pressure range of 0.02 - 0.12 showed that when the TTBP:TBPM molar ratio decreased from 1:1 to 0.6:1 to 0.3:1, the apparent specific surface area increased from 478 m<sup>2</sup> g<sup>-1</sup> to 979 m<sup>2</sup> g<sup>-1</sup> to 1,548 m<sup>2</sup> g<sup>-1</sup>, respectively (Figure 2-21). This result confirmed that a higher ratio of TBPM leads to higher surface area. PA-POF-1s were ion-exchangeable, as proven by EDX analysis from Figure 2-22. The absence of Na in EDX spectrum of PA-POF-1 [0.3:1] after ion exchange (Fig. 2-22) was because of the low content of P.

Next, the synthesis of P-WCA-POF with lithium as the cation was attempted. It was hoped that the small Li<sup>+</sup> cations were more easily ion-exchangeable, and that the acid-treatment would not be needed. As shown in Figure 2-15, the synthesis of P-WCA-POF-2 [1:1] was carried out using the same method as P-WCA-POF-1 [1:1], however the triethylammonium ions were replaced by lithium ions. The polymerization succeeded with LTBP and TBPM in a molar ratio of 1:1 in the Yamamoto coupling reaction and P was found to be in the desired coordination number 6 as shown by the <sup>31</sup>P MAS NMR spectrum (Figure 2-23). The product showed a BET surface area of 490 m<sup>2</sup> g<sup>-1</sup> according to N<sub>2</sub> adsorption (Figure 2-24). However, the cations are not exchangeable after the ion-exchange in NaCl solution (Fig. 2-25). The reason for this may be the same as P-WCA-POF-1 [1:1] which is that the lithium ions are located within the pore walls and are tightly surrounded by organic polymer.

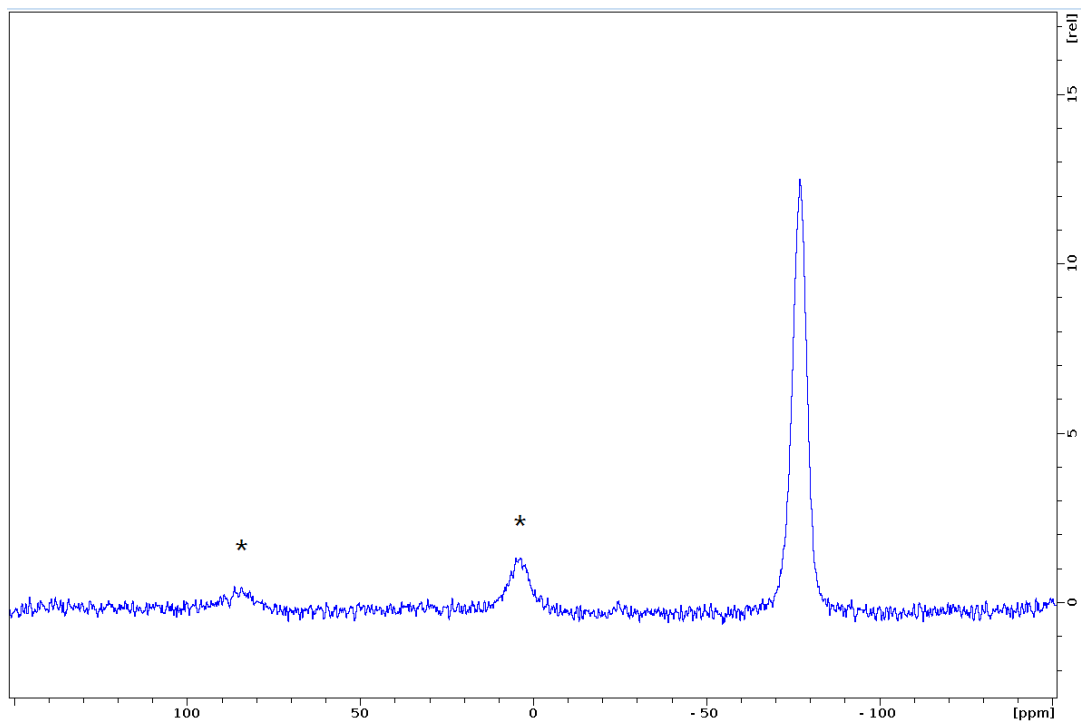


Figure 2-23.  $^{31}\text{P}$  solid state NMR spectrum of P-WCA-POF-2 [1:1]. Asterisks (\*) indicate peaks arising from spinning side bands.

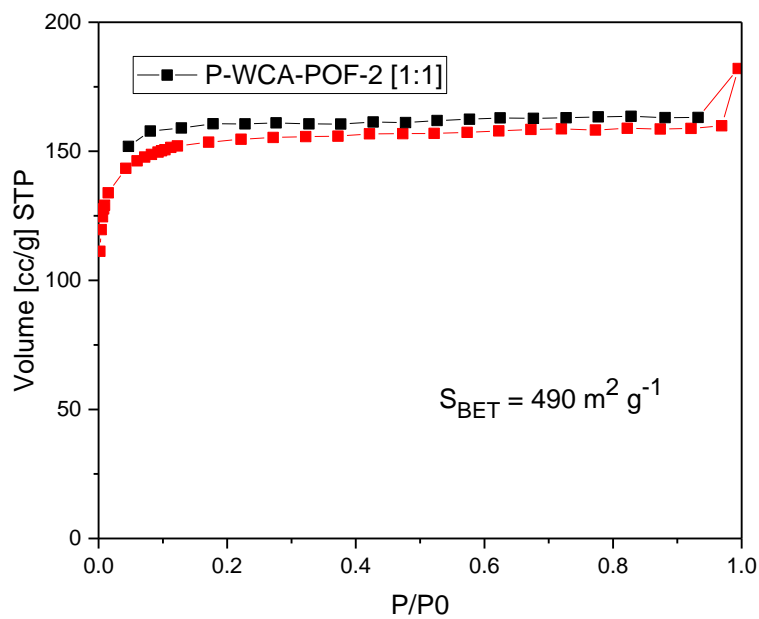


Figure 2-24. Nitrogen adsorption (red squares) and desorption (black squares) isotherms of P-WCA-POF-2 [1:1] measured at 77K.

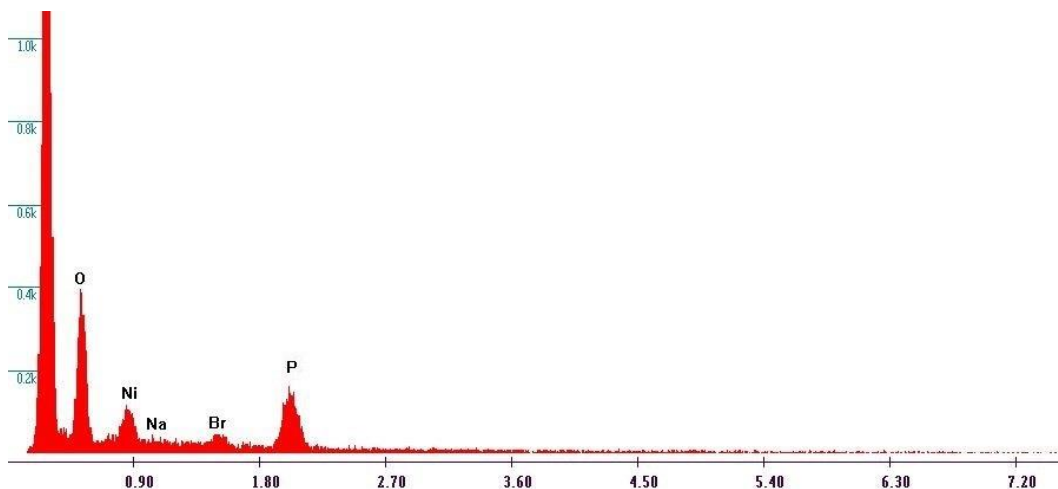


Figure 2-25. EDX spectrum of P-WCA-POF-2 [1:1] after ion exchange in NaCl solution. No Na can be found in the EDX spectrum shows that the cation was not exchangeable.

EDX analysis of the material showed substantial amounts of the Ni used as a coupling agent inside P-WCA-POF-2 [1:1]. This phenomenon has been observed in P-WCA-POF-1 [1:1]. In the synthesis of PA-POF-1, concentrated hydrochloric acid was used to remove the Ni impurities from P-WCA-POF-1 [1:1] and produced PA-POF-1 [1:1]. Here the same acid treatment was done to P-WCA-POF-2 [1:1]. The acid wash did remove almost all Ni (Figure 2-26), and also converted the hexa-coordinated  $[P(O_2Ar)_3]^-$  units into  $PO_4$  phosphate functional groups (Figure 2-15) as confirmed by  $^{31}P$  MAS NMR (Fig. 2-27). The acid treated material (PA-POF-2 [1:1]) showed a type I  $N_2$  isotherm and a surprisingly high apparent BET surface area of  $1,536 \text{ m}^2 \text{ g}^{-1}$  (Figure 2-28). The material is ion-exchangeable by  $Na^+$  (Figure 2-29) according to EDX, suggesting that the pores are now open.

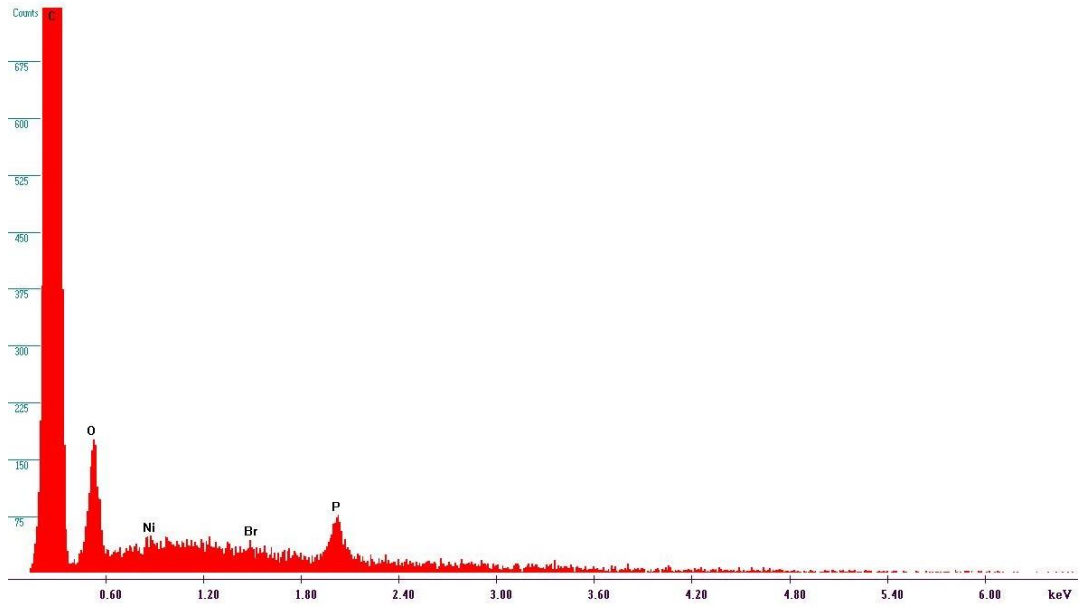


Figure 2-26. EDX spectrum of P-WCA-POF-2 [1:1] after treatment of concentrated HCl.

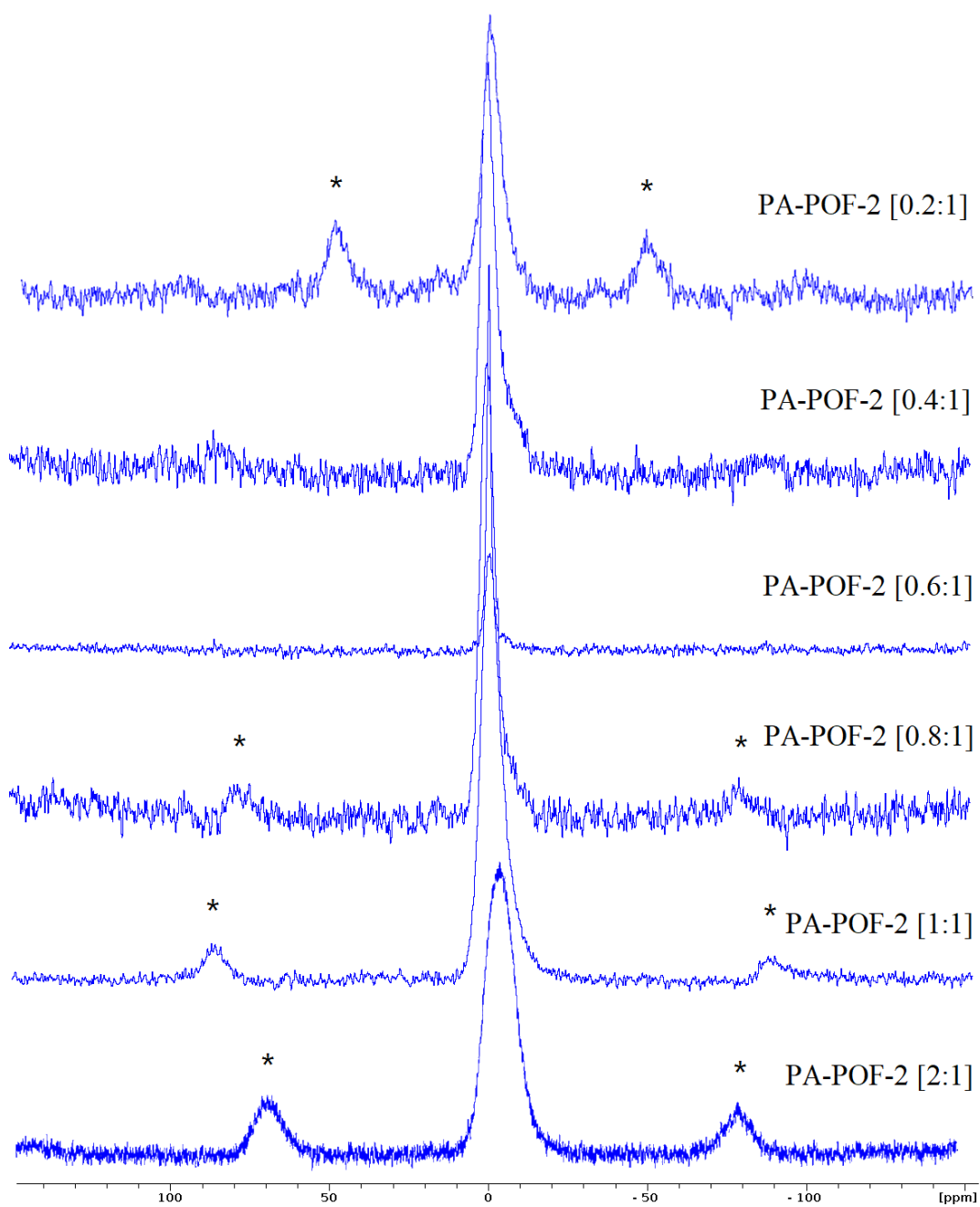


Figure 2-27.  $^{31}\text{P}$  solid state NMR spectrum of PA-POF-2s.

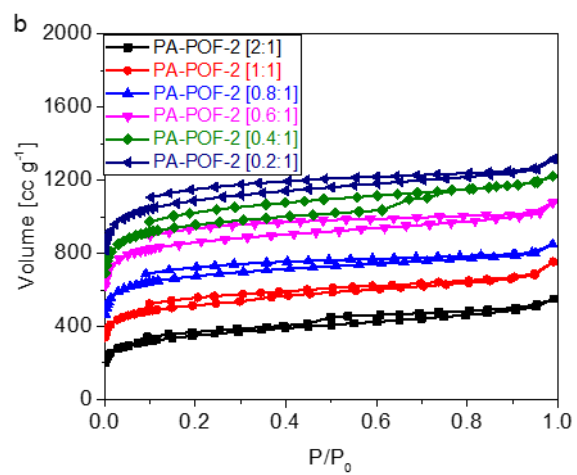


Figure 2-28. Nitrogen sorption isotherms of PA-POF-2s.

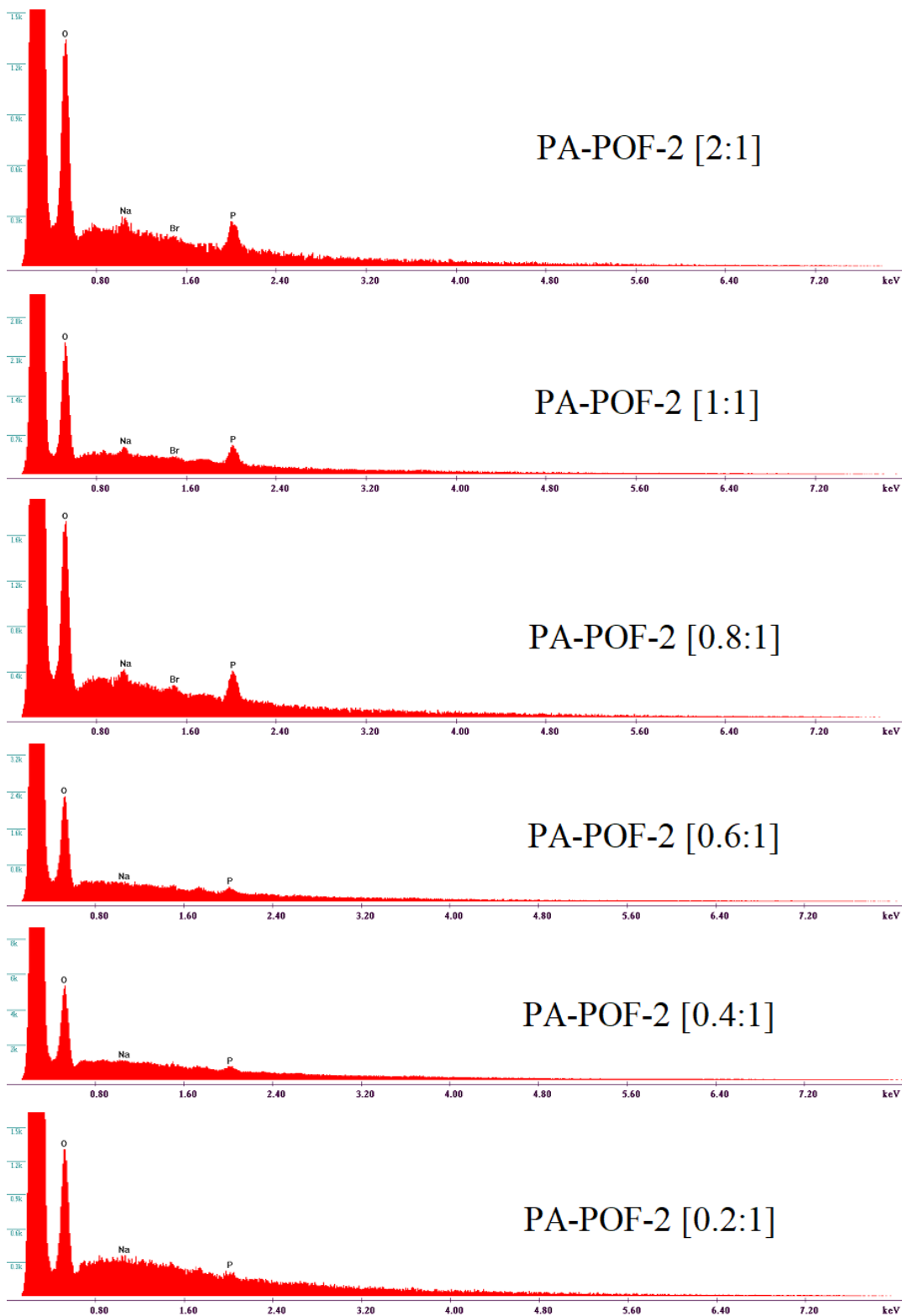


Figure 2-29. EDX spectrum of PA-POF-2s after ion exchange in NaCl solution.

In the study of PA-POF-1s, it was found that a greater portion of TBPM in the polymer increases the surface areas of PA-POF-1s. Analysis of the N<sub>2</sub> sorption isotherms of PA-POF-2 [TTBP:TBPM] materials by the BET method within the relative pressure range of 0.03 - 0.2 showed that the apparent BET surface area of PA-POF-2 [LTBP:TBPM] ranging from 1,291 m<sup>2</sup> g<sup>-1</sup> to 2,408 m<sup>2</sup> g<sup>-1</sup> as the LTBP:TBPM molar ratio changed from 2:1 to 0.2:1 (Figure 2-28). This result confirmed that a higher ratio of TBPM leads to higher porosity. However, compared with the surface areas of PA-POF-1s, the surface area of PA-POF-2s were much larger, possibly because different cations have different templating effects that influence the structure of the polymerizing frameworks. It is worthwhile to mention that no product was collected after the hydrochloric acid treatment in the synthesis of PA-POF-1 [2:0] and PA-POF-1 [2:1], as well as PA-POF-2 [2:0]. The reason for this is that the acid treatment breaks P-O bonds and leaves only terminal PO<sub>4</sub> units. If TTBP/LTBP is used as the sole starting monomer, the framework is linked by a large number of [P(O<sub>2</sub>Ar)<sub>3</sub>]<sup>-</sup> nodes. The breakage of these nodes by acid depolymerizes the framework to give smaller, soluble molecules. PA-POF-2s were also ion-exchangeable, as proven by EDX analysis in Figure 2-29. In PA-POF [0.6:1], PA-POF [0.4:1] and PA-POF [0.2:1], the Na signals were below the detection limit in the EDX spectra after Na<sup>+</sup> ion exchange because of the low content of P in these materials. These observations are also in accordance with PA-POF-1s.

The synthesis procedures of P-WCA-POFs and PA-POFs are listed as following.

P-WCA-POF-1: 1,5-cyclooctadiene (cod, 0.7 mL, 5.55 mmol, Acros Organics) was added to a solution of bis(1,5-cyclooctadiene) nickel (0) ([Ni(cod)<sub>2</sub>], 1.125 g, 4.09 mmol, Acros Organics), and 2,2'-bipyridyl (640 mg, 4.09 mmol, TCI) in anhydrous DMF (30 mL,



Acros Organics). To the purple solution, TTBP (312 mg, 0.449 mmol) and TBPM (213 mg, 0.336 mmol, TCI) were added. The reaction mixture was stirred and heated at 90 °C for three days to obtain a deep purple suspension. After cooling to RT, the suspension was vacuum filtered. The residue solid was washed with acetone and methanol, and dried in vacuo to give P-WCA-POF-1 [1:1] as a deep green powder (612 mg, 197%).

P-WCA-POF-2: 1,5-cyclooctadiene (cod, 0.7 mL, 5.55 mmol, Acros Organics) was added to a solution of bis(1,5-cyclooctadiene) nickel (0) ( $[\text{Ni}(\text{cod})_2]$ , 1.125 g, 4.09 mmol, Acros Organics), and 2,2'-bipyridyl (640 mg, 4.09 mmol, TCI) in anhydrous DMF (30 mL, Acros Organics). To the purple solution, LTBP (269 mg, 0.449 mmol) and TBPM (213 mg, 0.336 mmol, TCI) were added. The reaction mixture was stirred and heated at 90 °C for three days to obtain a deep purple suspension. After cooling to RT, the suspension was vacuum filtered. The residue solid was washed with acetone and methanol, and dried in vacuo to give P-WCA-POF-2 [1:1] as a deep greyish green powder (379 mg, 142%).

The yields of P-WCA-POFs were more than 100% because the materials included substantial amounts of Ni as shown by EDX.

PA-POF-1 [1:1]: 1,5-cyclooctadiene (cod, 0.7 mL, 5.55 mmol, Acros Organics) was added to a solution of bis(1,5-cyclooctadiene) nickel (0) ( $[\text{Ni}(\text{cod})_2]$ , 1.125 g, 4.09 mmol, Acros Organics), and 2,2'-bipyridyl (640 mg, 4.09 mmol, TCI) in anhydrous DMF (30 mL, Acros Organics). To the purple solution, TTBP (312 mg, 0.449 mmol) and TBPM (213 mg, 0.336 mmol, TCI) were added. The reaction mixture was stirred and heated at 90 °C for three days to obtain a deep purple suspension. To this purple suspension, concentrated HCl (10 mL x 2, EMD Millipore) was added and stirred for 15 min. The reaction mixture became hot and a lot of bubbles were released. The purple color of the reaction mixture

faded to green, and a lot of light yellow precipitates formed. This yellow precipitate was then vacuum filtered. The residue solid was washed with H<sub>2</sub>O, acetone and methanol, and dried in vacuo to give PA-POF-1 [1:1] as a light yellow powder (106 mg). Elemental analysis (%) found: C (80.55), H (4.90), N (1.05), P (1.66).

PA-POF-1 [2:0], [2:1], [0.6:1], [0.3:1] were also synthesized using the same method except the amounts of TTBP and TBPM were added as below.

PA-POF-1 [2:0] (0 mg): TTBP (312 mg, 0.449 mmol)

PA-POF-1 [2:1] (0 mg): TTBP (312 mg, 0.449 mmol), TBPM (106 mg, 0.168 mmol)

PA-POF-1 [0.6:1] (98 mg): TTBP (187 mg, 0.269 mmol), TBPM (213 mg, 0.336 mmol). Elemental analysis (%) found: C (82.20), H (5.17), N (1.25), P (1.22).

PA-POF-1 [0.3:1] (103 mg): TTBP (94 mg, 0.135 mmol), TBPM (213 mg, 0.336 mmol). Elemental analysis (%) found: C (91.58), H (6.09), N (0.90), P (< 0.4).

PA-POF-2 [1:1]: 1,5-cyclooctadiene (cod, 0.7 mL, 5.55 mmol, Acros Organics) was added to a solution of bis(1,5-cyclooctadiene) nickel (0) ([Ni(cod)<sub>2</sub>], 1.125 g, 4.09 mmol, Acros Organics), and 2,2'-bipyridyl (640 mg, 4.09 mmol, TCI) in anhydrous DMF (30 mL, Acros Organics). To the purple solution, LTBP (269 mg, 0.449 mmol) and TBPM (213 mg, 0.336 mmol, TCI) were added. The reaction mixture was stirred and heated at 90 °C for three days to obtain a deep purple suspension. To this purple suspension, concentrated HCl (10 mL x 2, EMD Millipore) was added and stirred for 15 min. The reaction mixture became hot and a lot of bubbles were released. The purple color of the reaction mixture faded to green, and a lot of light yellow precipitates formed. This yellow precipitate was then vacuum filtered. The residue solid was washed with H<sub>2</sub>O, acetone and methanol, and

dried in vacuo to give PA-POF-2 [1:1] as a light yellow powder (92 mg). Elemental analysis (%) found: C (83.14), H (5.18), N (1.09), P (0.93).

PA-POF-2 [2:0], [2:1], [0.8:1], [0.6:1], [0.4:1], [0.2:1] were also synthesized using the same method except the amounts of LTBP and TBPM were added as below.

PA-POF-2 [2:0] (0 mg): LTBP (269 mg, 0.449 mmol)

PA-POF-2 [2:1] (43 mg): LTBP (269 mg, 0.449 mmol), TBPM (106 mg, 0.168 mmol). Elemental analysis (%) found: C (84.14), H (4.92), N (1.04), P (1.44).

PA-POF-2 [0.8:1] (101 mg): LTBP (215 mg, 0.359 mmol), TBPM (213 mg, 0.336 mmol). Elemental analysis (%) found: C (87.01), H (4.88), N (0.85), P (<0.4).

PA-POF-2 [0.6:1] (90 mg): LTBP (161 mg, 0.269 mmol), TBPM (213 mg, 0.336 mmol). Elemental analysis (%) found: C (87.23), H (5.46), N (0.63), P (<0.4).

PA-POF-2 [0.4:1] (97 mg): LTBP (108 mg, 0.180 mmol), TBPM (213 mg, 0.336 mmol). Elemental analysis (%) found: C (88.26), H (5.15), N (0.91), P (<0.4).

PA-POF-2 [0.2:1] (97 mg): LTBP (54 mg, 0.0898 mmol), TBPM (213 mg, 0.336 mmol). Elemental analysis (%) found: C (88.91), H (5.34), N (0.84), P (<0.4).

## 2.4 Characterization of PA-POFs

The scanning electron microscopy (SEM) images and energy dispersive X-ray spectroscopy (EDX) spectra were taken using a Hitachi S-4300 SEM. Samples were dispersed over a sticky carbon surface adhered to a flat aluminum platform sample holder. Samples were coated with 5 nm thick iridium for SEM imaging. Samples analyzed by EDX were not coated with any material for a better understanding of element analysis. X-ray diffraction data were recorded using a Rigaku Rotaflex diffractometer with a Cu K $\alpha$

radiation source ( $\lambda = 0.15405$  nm). The thermogravimetric analysis (TGA) experiments were carried out both in air and nitrogen using a TA instrument Q-500 series thermal gravimetric analyzer, with a heating rate of  $10$  °C  $\text{min}^{-1}$ . Solution phase  $^1\text{H}$ ,  $^{13}\text{C}$ ,  $^{31}\text{P}$  and  $^7\text{Li}$  NMR spectra were obtained on a Bruker Avance 500 MHz instrument.  $^{31}\text{P}$  solid state NMR spectra were obtained on a Bruker Avance III HD 400 MHz instrument. Samples were packed into 4 mm outer diameter zirconia rotors and inserted into a Bruker magic angle spinning (MAS) probe. One pulse experiments were employed with a 20 s relaxation delay. The acquisition time was 0.041779 us. The number of scans were between 1000 to 5000. The  $^{31}\text{P}$  chemical shift of  $\text{NH}_4\text{H}_2\text{PO}_4$  was set to zero using external reference standard. Nitrogen and carbon dioxide sorption measurements were collected using a Quantachrome Autosorb-1 instrument. Before analysis, all the samples were outgassed five hours at  $200$  °C in vacuum. The Brunauer-Emmett-Teller surface area analysis was carried out using five data points in the pressure range between 0.05 and 0.2  $\text{P}/\text{P}_0$ .

The scanning electron microscopy (SEM) images of the PA-POFs showed that the materials are composed of spherical or near-spherical particles (Figure 2-30 and 2-31) which is typical for highly cross-linked polymers. No or small Ni signals can be found in EDX spectra of PA-POF-1s and -2s, proving HCl treatment is effective in removing the Ni impurities. According to powder X-ray diffraction (PXRD) patterns (Figure 2-32), no long-range-ordered structures are observed for all the PA-POFs. This result was expected because the inert nature of the C-C bonds formed during the coupling reaction prohibits crystallization. The thermal and oxidative stability of the PA-POFs was also studied. Thermogravimetric analysis (TGA) shows that all the PA-POF materials are stable up to  $450$  °C in air (Figure 2-33), and up to  $600$  °C in  $\text{N}_2$  environment (Figure 2-34). The FTIR

spectra of PA-POFs are shown in Figure 2-35. Because of the similar chemical nature of the building blocks and the rather low content of phosphate groups in the material, the spectra of PA-POFs and PAF-1 are very similar.

All the PA-POF materials show type I nitrogen sorption isotherms, which means all the PA-POFs are microporous materials. The CO<sub>2</sub> adsorption isotherms of PA-POFs were measured from  $P/P_0 = 10^{-3}$  to  $P/P_0 = 1$  at 273 K to analyze the micropore size distribution. As shown in Figure 2-36, all the PA-POFs showed a similar pore size distribution based on non-local density functional theory (NLDFT) calculations from CO<sub>2</sub> adsorption isotherms at 273 K. Two distinct pore sizes at 0.57 nm and 0.82 nm can be seen in all PA-POFs. The pore sizes of PA-POFs are very different from PAF-1, whose micropore size distribution is centered at 1.4 nm.<sup>17</sup> As shown in Table 2-1, the cumulative pore volume of the PA-POF materials increased with increasing TBPM molar ratio, ranging from 0.4 cm<sup>3</sup> g<sup>-1</sup> to 0.75 cm<sup>3</sup> g<sup>-1</sup>, and 0.74 cm<sup>3</sup> g<sup>-1</sup> to 1.09 cm<sup>3</sup> g<sup>-1</sup> for PA-POF-1s and PA-POF-2s, respectively.

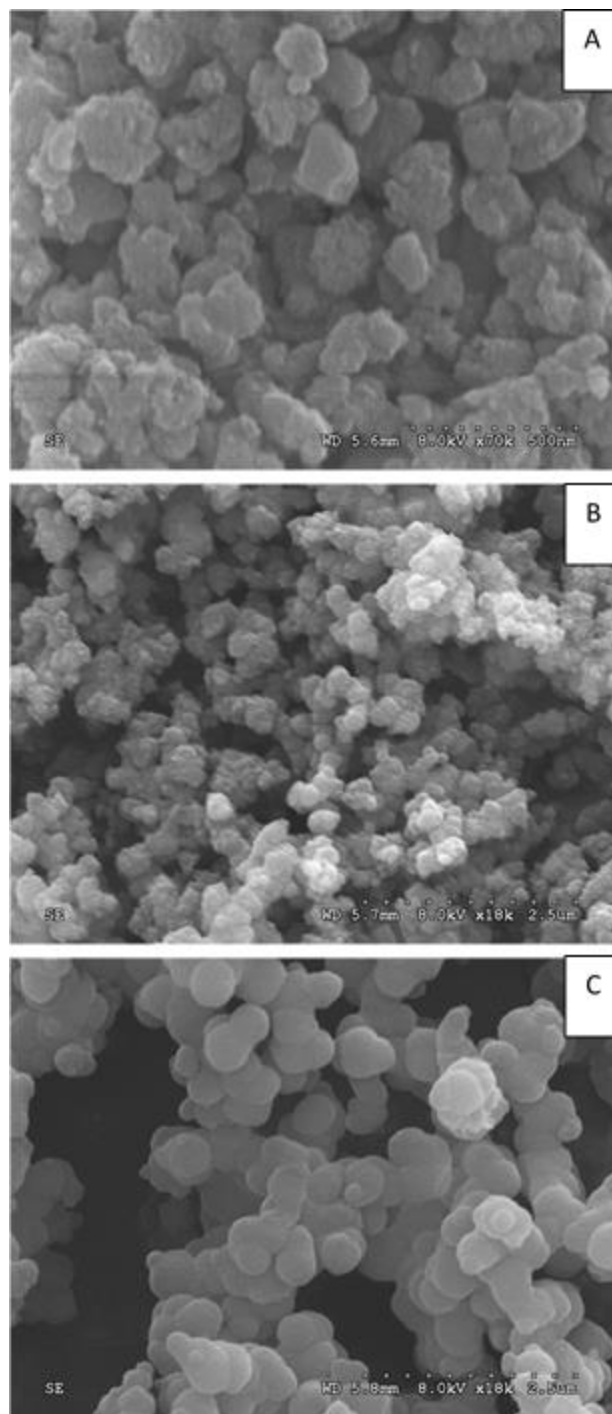


Figure 2-30. SEM images of PA-POF-1s. A: PA-POF-1 [1:1]; B: PA-POF-1 [0.6:1]; C: PA-POF-1 [0.3:1].

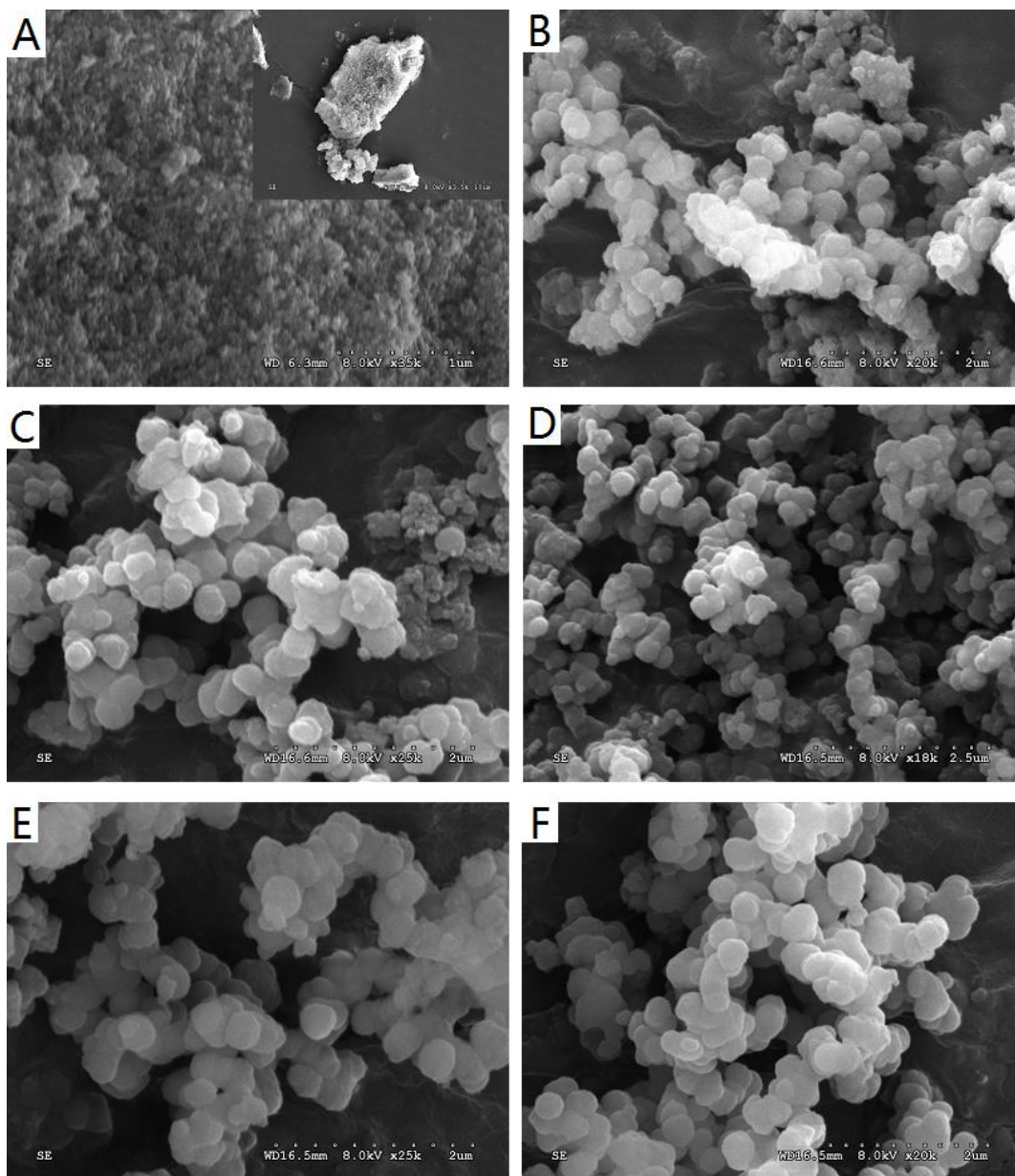


Figure 2-31. SEM images of PA-POF-2s. (A) PA-POF-2 [2:1]; (B) PA-POF-2 [1:1]; (C) PA-POF-2 [0.8:1]; (D) PA-POF-2 [0.6:1]; (E) PA-POF-2 [0.4:1]; and (F) PA-POF-2 [0.2:1].

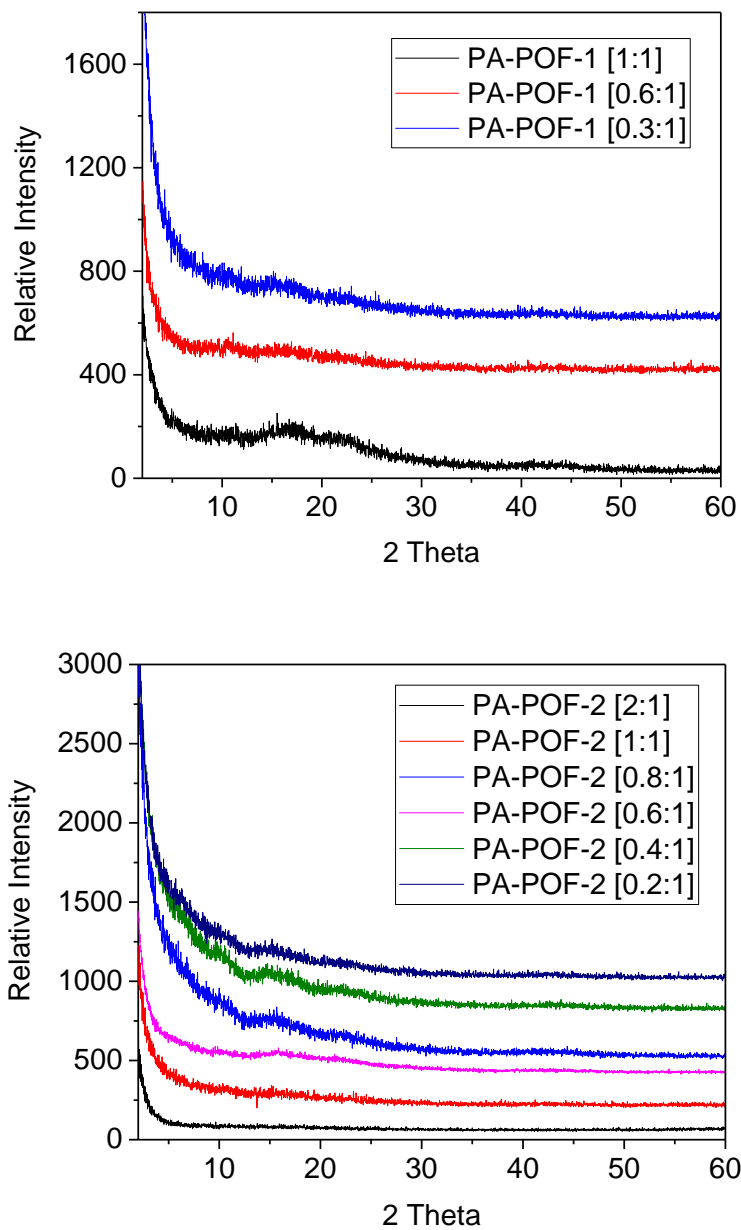


Figure 2-32. XRD patterns of PA-POF-1s and PA-POF-2s. Patterns are offset for clarification.



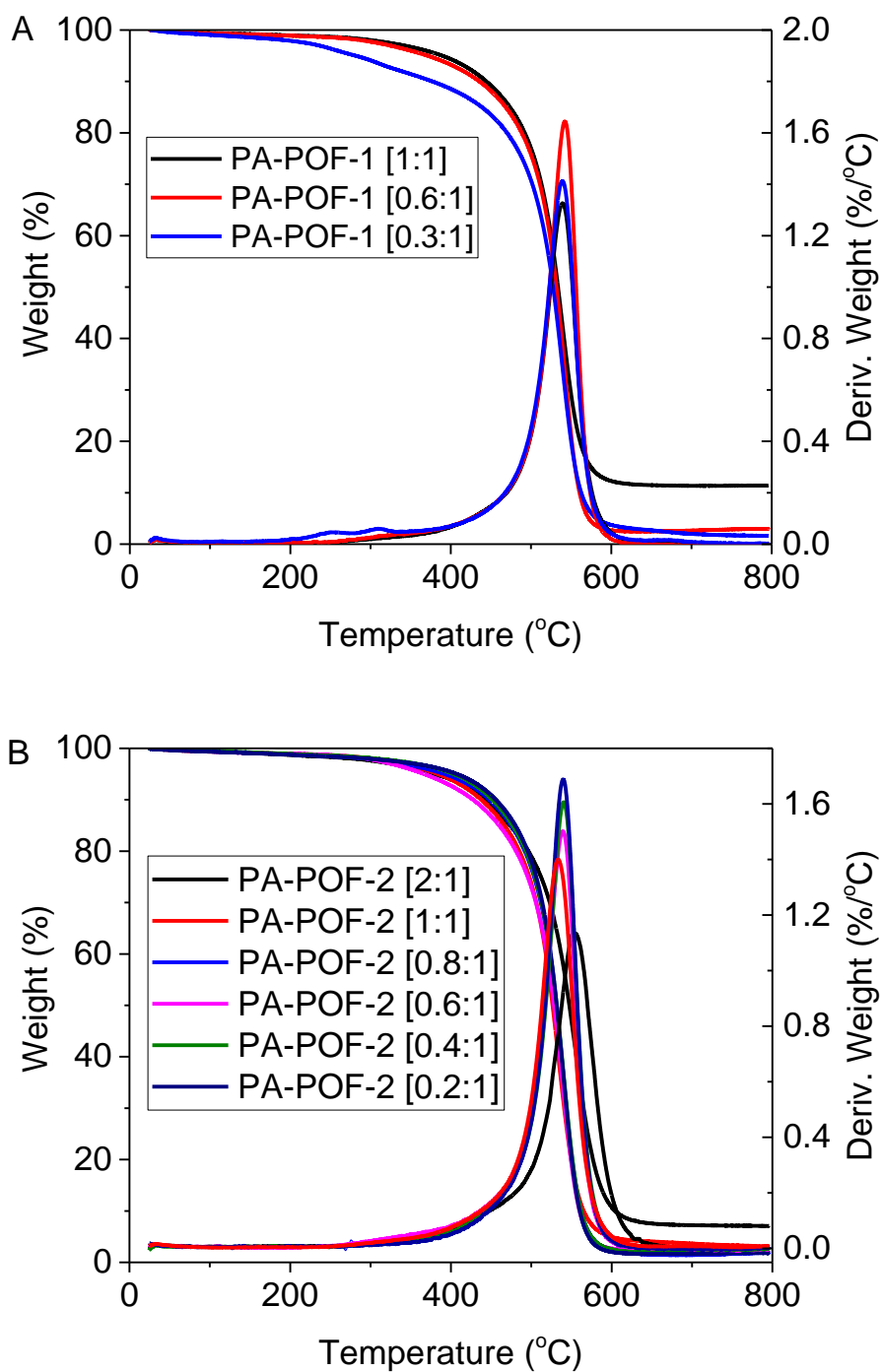


Figure 2-33. (A) PA-POF-1s and (B) PA-POF-2s thermograms measured in air.

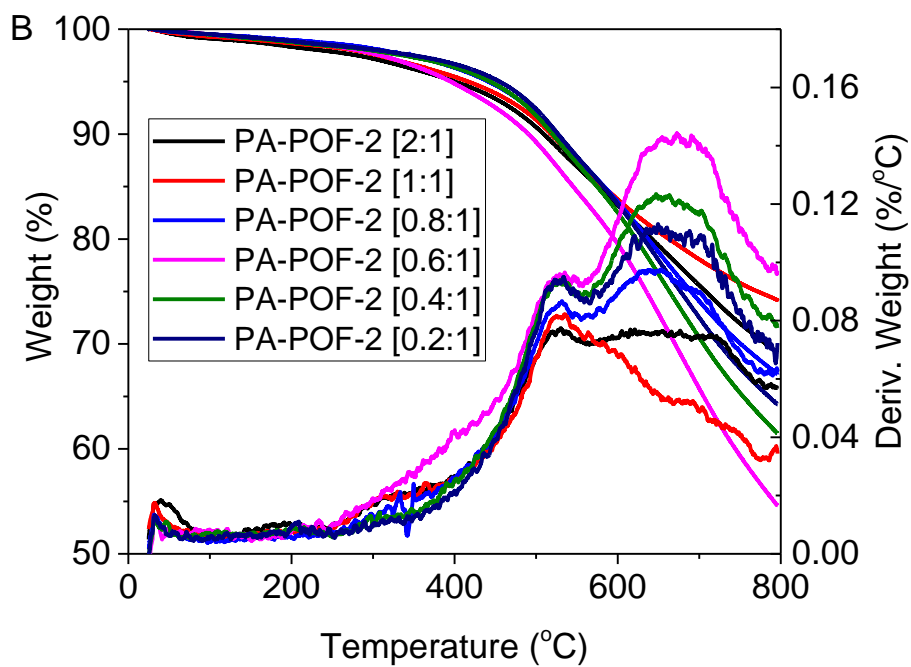
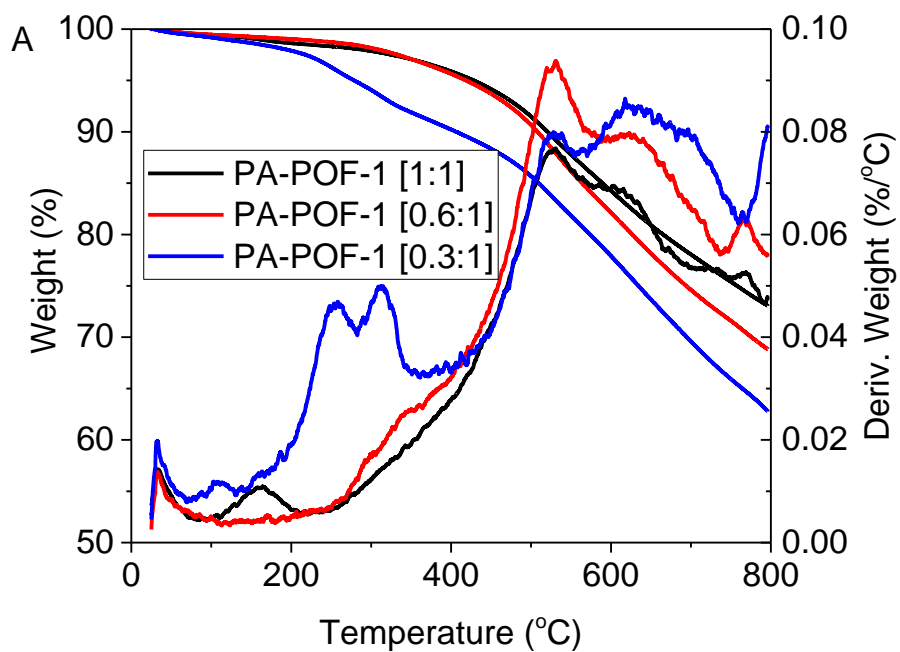


Figure 2-34. (A) PA-POF-1s and (B) PA-POF-2s thermograms measured in nitrogen.

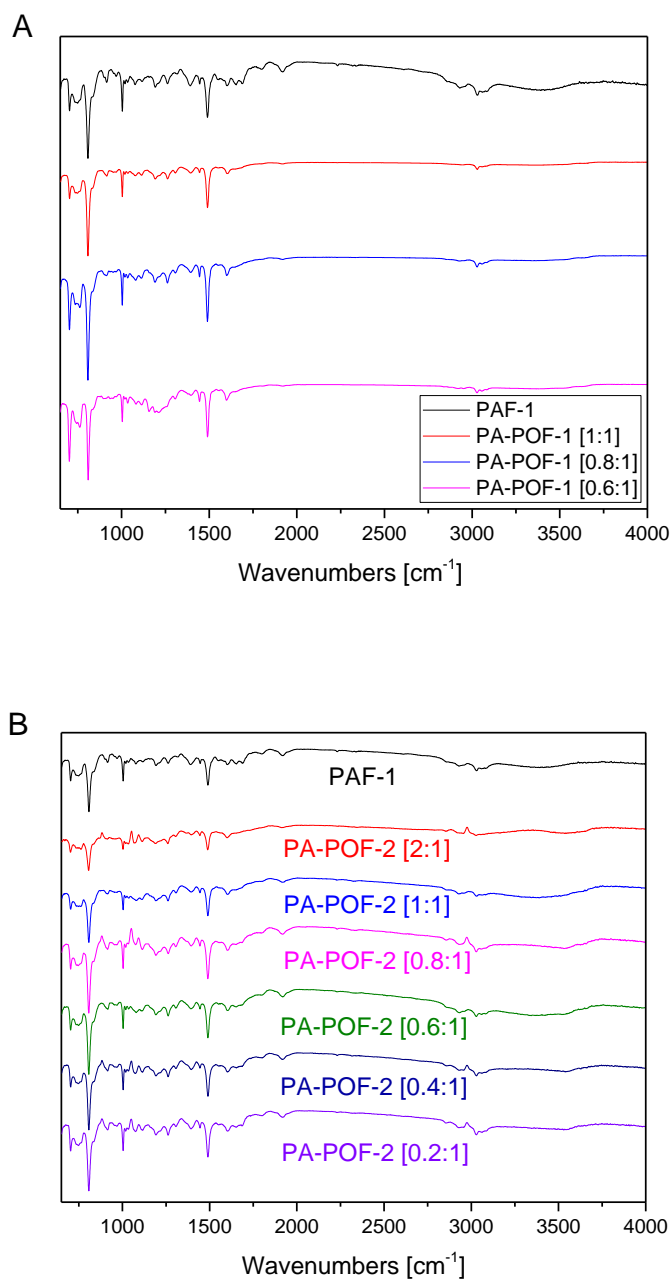


Figure 2-35: FTIR spectra of (A) PA-POF-1s and (B) PA-POF-2s. The FTIR spectrum of PAF-1 was inserted in each figure for comparison. Spectra are labeled by compound names. Because of the low content of phosphorus, P-O stretching is not obvious in the spectra.

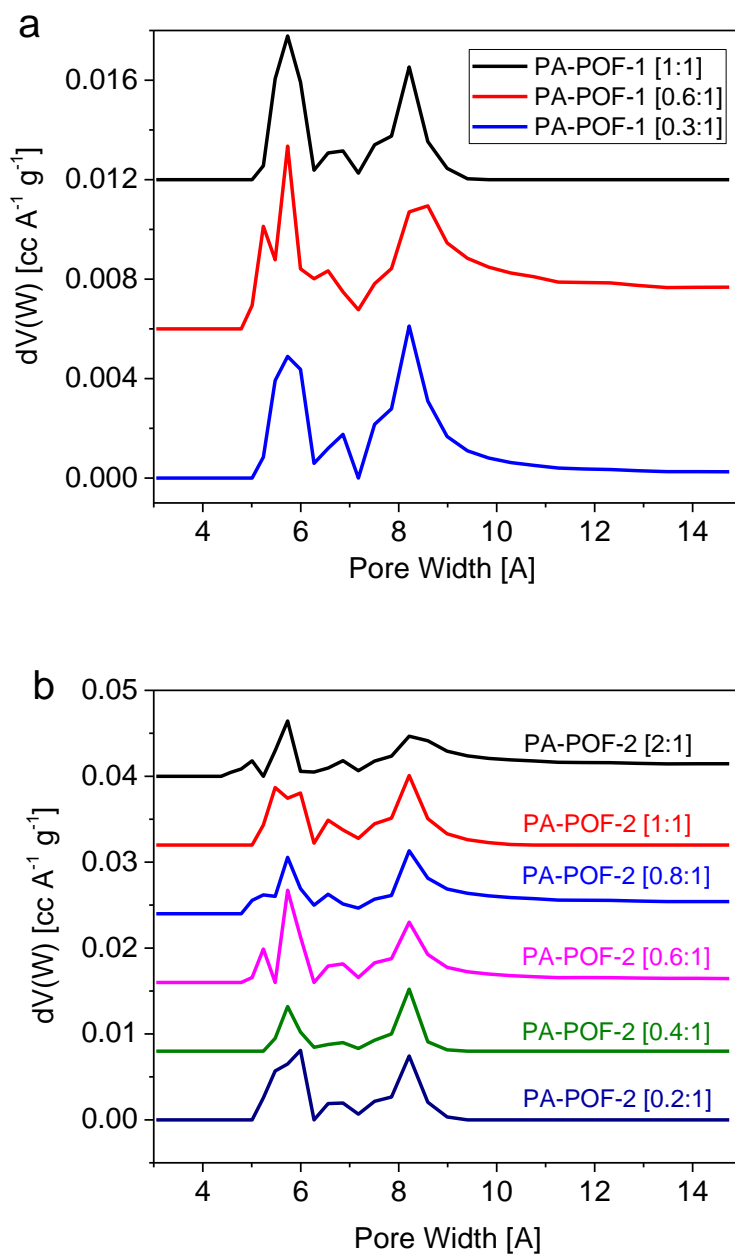


Figure 2-36. Pore size distribution of (a) PA-POF-1s and (b) PA-POF-2s calculated from CO<sub>2</sub> sorption isotherms collected at 273 K by NLDFT method (carbon slit pore model).

Table 2-1. Summary of apparent BET surface area and pore volume of PA-POFs.

<b>SAMPLE ID</b>	<b>BET SURFACE AREA (M<sup>2</sup> G<sup>-1</sup>)</b>	<b>DFT &amp; MONTE-CARLO CUMULATIVE PORE VOLUME (CM<sup>3</sup> G<sup>-1</sup>)</b>
PA-POF-1 [1:1]	478	0.40
PA-POF-1 [0.6:1]	979	0.56
PA-POF-1 [0.3:1]	1548	0.75
PA-POF-2 [2:1]	1291	0.74
PA-POF-2 [1:1]	1536	0.86
PA-POF-2 [0.8:1]	1761	0.84
PA-POF-2 [0.6:1]	2084	1.03
PA-POF-2 [0.4:1]	2220	1.08
PA-POF-2 [0.2:1]	2408	1.09

## 2.5 References

- 1 S. Fischer, J. Schmidt, P. Strauch and A. Thomas, *Angew. Chemie - Int. Ed.*, 2013, **52**, 12174–12178.
- 2 Y. Du, H. Yang, J. M. Whiteley, S. Wan, Y. Jin, S. H. Lee and W. Zhang, *Angew. Chemie - Int. Ed.*, 2016, **55**, 1737–1741.
- 3 J. F. Van Humbeck, M. L. Aubrey, A. Alsbaiee, R. Ameloot, G. W. Coates, W. R. Dichtel and J. R. Long, *Chem. Sci.*, 2015, **6**, 5499–5505.
- 4 H. R. Allcock and E. C. Bissell, *J. Am. Chem. Soc.*, 1973, **95**, 3154–3157.
- 5 H. R. Allcock and E. C. Bissell, *J. Chem. Soc. Chem. Commun.*, 1972, **0**, 676.
- 6 H. R. Allcock, *J. Am. Chem. Soc.*, 1964, **86**, 2591–2595.
- 7 H. R. Allcock, *J. Am. Chem. Soc.*, 1963, **85**, 4050–4051.
- 8 D. Hellwinkel and H.-J. Wilfinger, *Chem. Ber.*, 1970, **103**, 1056–1064.
- 9 D. Hellwinkel, *Chem. Ber.*, 1966, **99**, 3628–3641.
- 10 D. Hellwinkel, *Angew. Chemie*, 1965, **77**, 378–379.
- 11 M. Nakamoto and K. Akiba, *J. Am. Chem. Soc.*, 1999, **121**, 6958.
- 12 A. Chandrasekaran, R. O. Day and R. R. Holmes, *Inorg. Chem.*, 2002, **41**, 1645.
- 13 M. Koenig, A. Klaébé, A. Munoz and R. Wolf, *J. Chem. Soc., Perkin Trans. 2*, 1976, **0**, 955–958.
- 14 M. Eberwein, A. Schmid, M. Schmidt, M. Zabel, T. Burgemeister, J. Barthel, W. Kunz and H. J. Gores, *J. Electrochem. Soc.*, 2003, **150**, A994.
- 15 S. Constant and J. Lacour, *New trends in hexacoordinated phosphorus chemistry*, Springer, Berlin, 2005, vol. 250.
- 16 T. Ben, H. Ren, S. Ma, D. Cao, J. Lan, X. Jing, W. Wang, J. Xu, F. Deng, J. M. Simmons, S. Qiu and G. Zhu, *Angew. Chemie Int. Ed.*, 2009, **48**, 9457–9460.
- 17 T. Ben, C. Pei, D. Zhang, J. Xu, F. Deng, X. Jing, S. Qiu, R. Q. Snurr, M. O’Keeffe, J. Kim, O. M. Yaghi, G. Zhu, V. Marsaud, P. Bories, L. Cynober, S. Gil, G. Férey, P. Couvreur and R. Gref, *Energy Environ. Sci.*, 2011, **4**, 3991.

## Chapter 3

### CO<sub>2</sub> adsorption properties of PA-POFs

#### 3.1 Introduction

CO<sub>2</sub> is widely considered as a greenhouse gas which is a key cause for global warming. Serious issues such as the rise of temperature, the increase in sea level, drop in pH of the surface sea water, and species extinction is believed to be associated with the massive emission of CO<sub>2</sub>. Over the last half century, the atmospheric CO<sub>2</sub> concentration has increased from ~300 ppm to 390 ppm.<sup>1</sup> For the past 400,000 years, such a level of atmospheric CO<sub>2</sub> concentration has never been reached.<sup>2,3</sup> The pH value of sea surface water could drop from 8.2 to 7.8 by 2095 due to the accumulative effect of the dissolved CO<sub>2</sub>.<sup>4</sup> Based on the possible scenarios presented in the International Panel on Climate Change (IPCC) climate report in 2007, the average global temperature is expected to rise by between 1.8 and 6.4 °C by the end of the 21st century.

As shown in Figure 3-1, approximately 77% of the greenhouse gas emission is attributed to CO<sub>2</sub>, among which 74% was released from the combustion of fossil fuels, including coal, natural gas, and oil. Global CO<sub>2</sub> emissions have increased by approximately 80% over the period of 1970 - 2004 (from 21 to 38 Gt per year), and these emission levels are projected to increase further over the next several decades owing to rises in energy demands associated with a growing global population and economic and industrial development, especially in developing countries.<sup>5</sup>

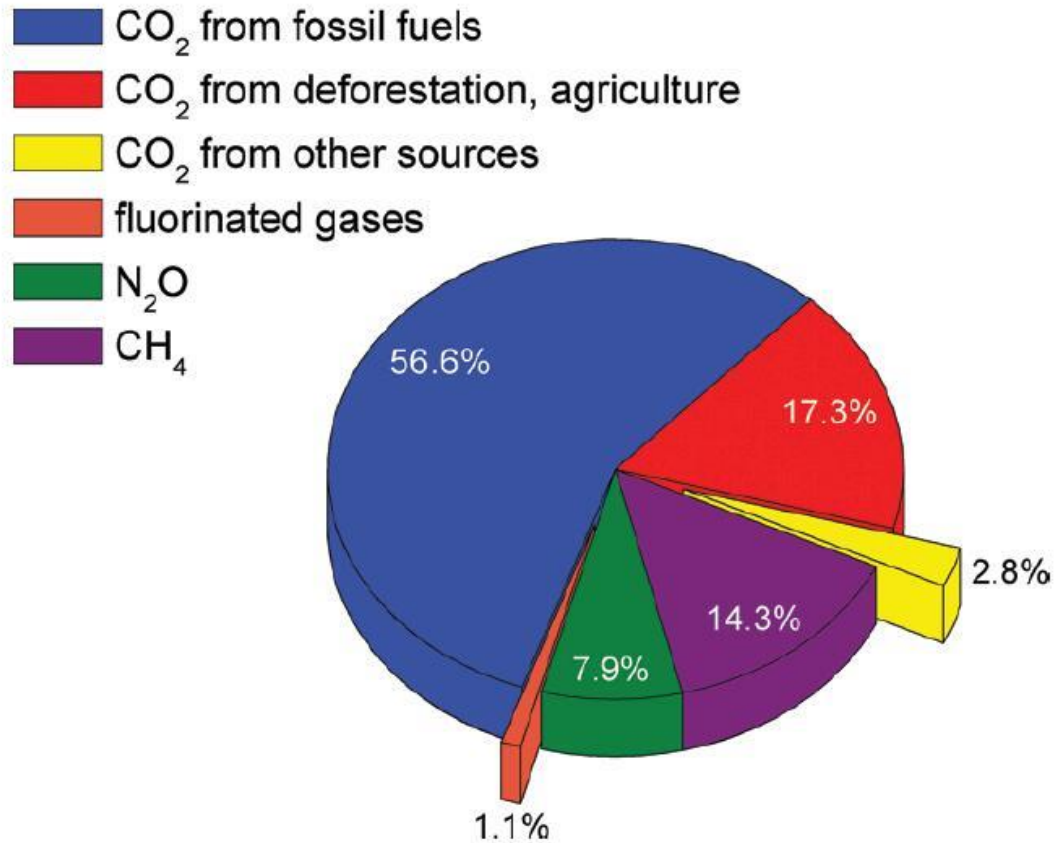


Figure 3-1. Global greenhouse gas emission sources in 2004. Ref. 5.

In order to reduce carbon emission, various approaches are being studied, which include the following:

1. Improving the thermal efficiency of fossil fuels. Normally the heat efficiency in a fossil fuel power station is ~33%. The combustion thermal efficiency of any fuel in a traditional generator or engine is limited by the Carnot cycle. For example, the theoretical maximum thermal efficiency of a car engine is ~74%, despite that the real efficiency is only ~30%. This limitation can be broken if fuels are used in a fuel cell. The theoretical heat efficiency of fuel cell could reach 100%. Even



though normally only 40% ~ 60% is reached, it is already much higher than traditional combustion methods. However, this technology is limited by immaturity as well as the very high price in production.

2. Switch to non-carbon fuel sources such as hydrogen. The hydrogen is abundant on earth because of the massive amount of water, and hydrogen gas is an acknowledged clean fuel because its only product is water. However, the continuous production of hydrogen is still challenging and pricy. In addition, because hydrogen is highly explosive when mixed with air, the safe storage and transportation of hydrogen still require many years of research, development and implementation.
3. Use of renewable energy such as solar energy, wind energy and nuclear energy. The wide use of solar energy needs high capital investment, and new technologies including the discovery of advanced materials are still developing for high conversion efficiency. The use of wind and water energy are strictly limited by locations. Nuclear fusion power, the ultimate energy solution, is undergoing a slow development. According to David Kingham, CEO of Tokamak Energy, Oxford, UK, humans are only half way towards the controllable use of fusion energy, and it is unlikely to use fusion energy at commercial scale before 2030.<sup>6</sup>
4. CO<sub>2</sub> capture and sequestration (CCS). Due to the abovementioned limitations of clean energy methodologies, fossil fuels would remain as the major energy source for a considerable amount of time. According to the U.S. Energy Information Administration, global energy-related CO<sub>2</sub> emissions will rise from 32.2 billion metric tons in 2012 to 35.6 billion metric tons in 2020 and to 43.2 billion metric

tons in 2040 -- an increase of 34% over the projection period (Figure 3-2).<sup>7</sup> Although the tremendous usage of fuel combustion for energy use is of significant concern, it does not mean humans are unable to prevent CO<sub>2</sub> emission. CCS have gained much attention because it allows the capture of the released CO<sub>2</sub> from fossil fuel power plants for further utilization or storage.

CO<sub>2</sub> capture and sequestration (CCS) is generally a three-step process that includes CO<sub>2</sub> separation and capture from sources, compression and transportation, and further utilization or permanent storage on the ocean floor in the form of solid gas hydrate.<sup>9</sup> Indeed, the installation of CCS systems within fossil fuel power stations that selectively remove CO<sub>2</sub> from the flue gas is able to significantly reduce the worldwide CO<sub>2</sub> emissions. CCS can lower the environmental impact of CO<sub>2</sub> until more environmentally sustainable energy sources are widely employed.<sup>8</sup> Currently, one of the greatest challenges in this process is the discovery of excellent adsorbent materials that display suitable physical and chemical properties and would remain stable in the long term. POFs, due to the permanent porosity, high surface areas and high thermal and chemical stabilities, are good candidates for CO<sub>2</sub> adsorption.

**Figure ES-8. World energy-related carbon dioxide emissions by fuel type, 1990–2040 (billion metric tons)**

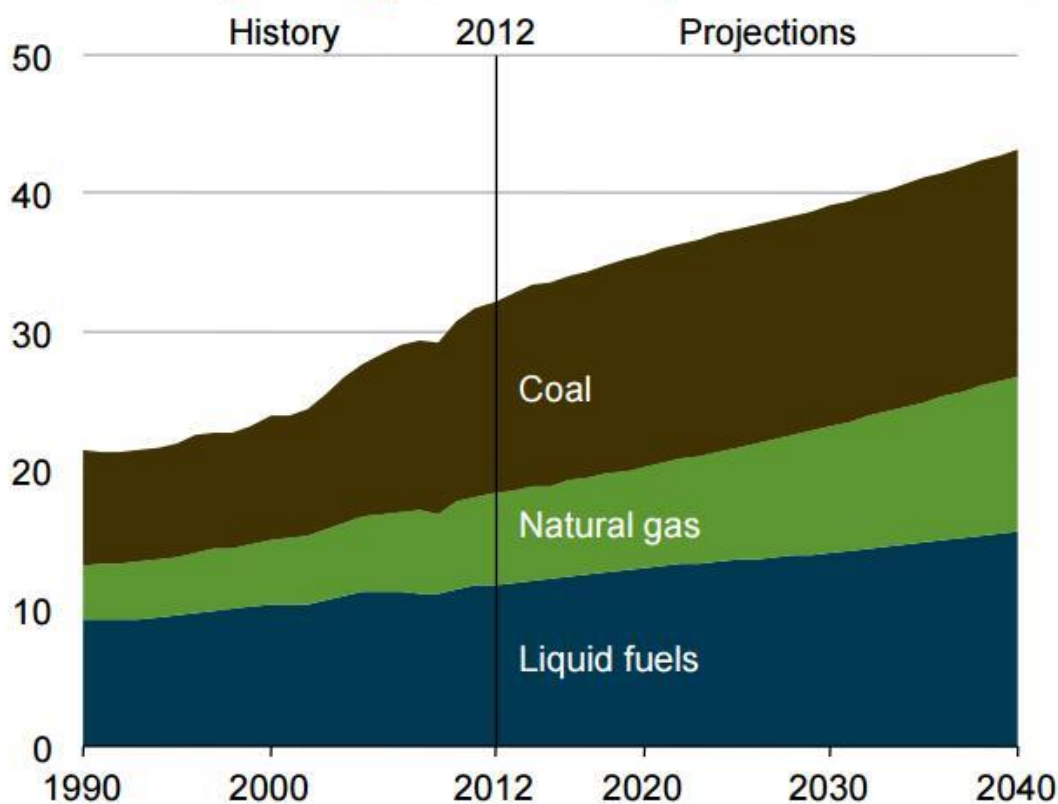


Figure 3-2. Projected growth in CO<sub>2</sub> emissions until 2040 by U.S. Energy Information Administration. Ref. 7.

### 3.2 CO<sub>2</sub> adsorption properties of PA-POFs

PA-POFs have high apparent BET surface areas up to 2408 m<sup>2</sup> g<sup>-1</sup>. In this section, the CO<sub>2</sub> adsorption properties of these materials is discussed. The CO<sub>2</sub> sorption measurements are shown in Figure 3-3, which were collected using a Quantachrome Autosorb-1 instrument. Before analysis, all the samples were outgassed five hours at 200 °C in vacuum.

The CO<sub>2</sub> adsorption isotherms at 258 K, 273 K, and 298 K (Figure 3-3) were measured. The BET surface areas, pore volumes, CO<sub>2</sub> uptakes, and heats of CO<sub>2</sub> adsorption of all the PA-POFs are summarized in Table 3-1.

Table 3-1. Summary of BET surface areas, pore volumes, CO<sub>2</sub> uptakes, and heats of CO<sub>2</sub> adsorption of PA-POFs.

Sample ID	BET surface area (m <sup>2</sup> g <sup>-1</sup> )	DFT & Monte-Carlo Cumulative Pore Volume (cm <sup>3</sup> g <sup>-1</sup> )	CO <sub>2</sub> uptake at 1 bar (cc g <sup>-1</sup> )			Isosteric Heat of CO <sub>2</sub> Adsorption (kJ mol <sup>-1</sup> )
			258 K	273 K	298 K	
PA-POF-1 [1:1]	478	0.40	66	56	34	23.8
PA-POF-1 [0.6:1]	979	0.56	89	85	54	20.8
PA-POF-1 [0.3:1]	1548	0.75	101	88	64	15.7
PA-POF-2 [2:1]	1291	0.74	78	73	43	22.2
PA-POF-2 [1:1]	1536	0.86	132	98	57	21.4
PA-POF-2 [0.8:1]	1761	0.84	126	91	64	23.8
PA-POF-2 [0.6:1]	2084	1.03	135	103	66	19.8
PA-POF-2 [0.4:1]	2220	1.08	133	97	59	20.4
PA-POF-2 [0.2:1]	2408	1.09	107	94	53	20.3

For PA-POF-1s, in general, CO<sub>2</sub> uptakes increase with the surface areas (Table 3-1). For PA-POF-2s, PA-POF-2 [2:1] has significantly lower CO<sub>2</sub> uptake than the other PA-POF-2s at all three temperatures. This is possibly because of the dense structure of PA-POF-2 [2:1]. As seen in the SEM images of PA-POFs (Figure 2-28), PA-POF-2 [2:1] has a much denser structure and larger particle size than all the other PA-POF-2s, which makes PA-POF-2 [2:1] lacking of macropores for a clear adsorption path of CO<sub>2</sub>. The CO<sub>2</sub> uptakes of PA-POF-2s are generally greater than PA-POF-1s, which can be attributed to the larger surface areas of PA-POF-2s. Among all PA-POF materials, PA-POF-2 [0.6:1] adsorbs the

most CO<sub>2</sub> with an uptake of 103 cc g<sup>-1</sup> (4.59 mmol g<sup>-1</sup>) at 273 K and 1 bar (Table 3-1). This adsorption capacity is remarkable compared with PAF-1. PAF-1 (Figure 3-4 a) only shows a CO<sub>2</sub> uptake of 45 cc g<sup>-1</sup> at 273 K and 1 bar.<sup>10</sup> The CO<sub>2</sub> adsorption capacities of PA-POFs are about twice as much as that of PAF-1, despite the smaller BET surface areas of the PA-POFs. The CO<sub>2</sub> adsorption capacity of PA-POF-2 [0.6:1] is also comparable to the best performing CO<sub>2</sub> adsorbing POF materials such as azo-linked polymers (ALPs; 3.52–5.37 mmol g<sup>-1</sup>),<sup>11</sup> microporous polycarbazole (CPOP-1; 4.82 mmol g<sup>-1</sup>),<sup>12</sup> imine-linked porous polymer frameworks (PPFs; 2.1–6.12 mmol g<sup>-1</sup>),<sup>13</sup> benzimidazole-linked polymers (BILPs; 2.91–5.34 mmol g<sup>-1</sup>)<sup>14-16</sup>, aminal-linked porous organic polymers (APOPs; 2.27–4.45 mmol g<sup>-1</sup>),<sup>17</sup> and covalent triazine polymers (PCTPs; 3.46–4.92 mmol g<sup>-1</sup>).<sup>18</sup>

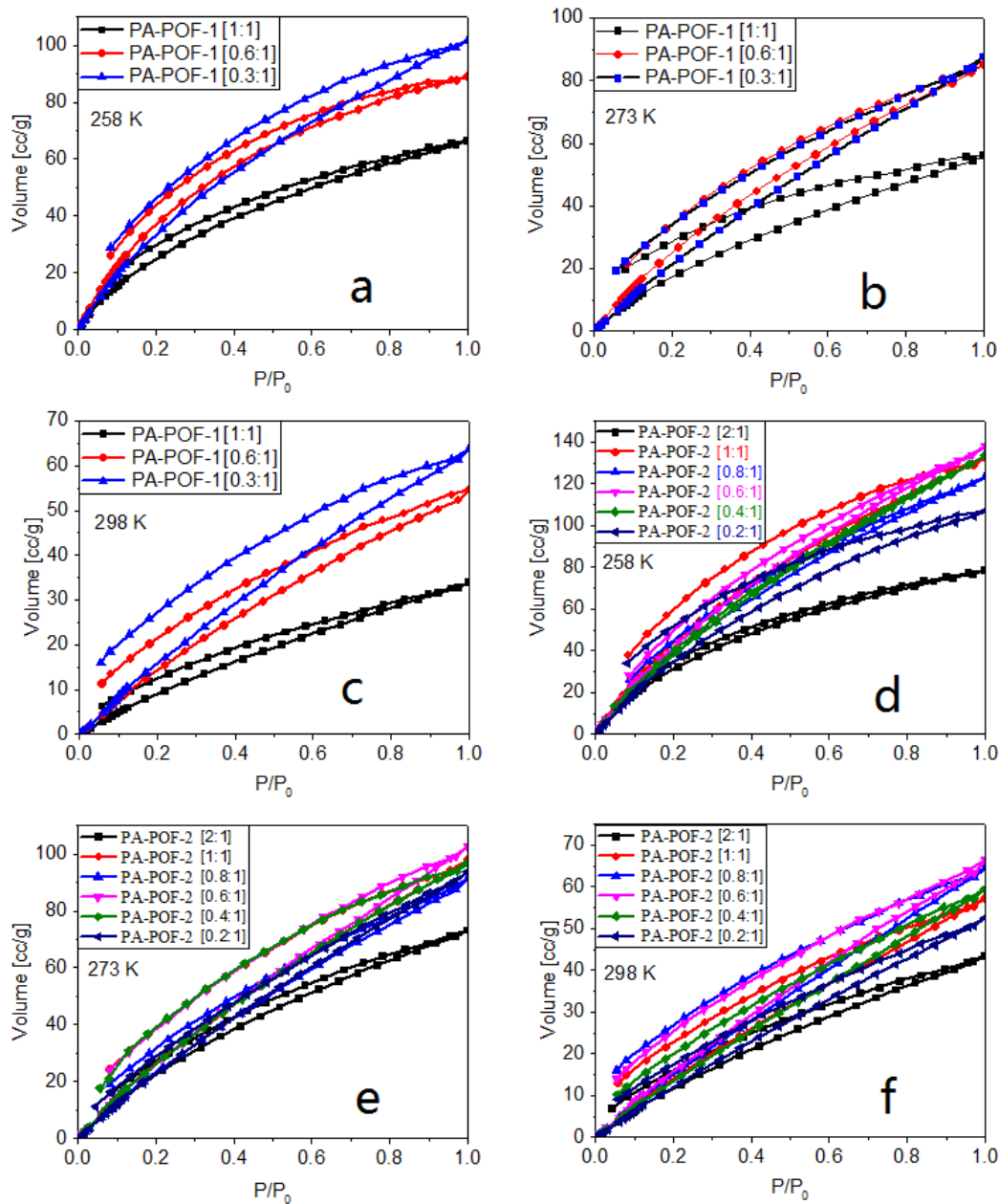


Figure 3-3. CO<sub>2</sub> adsorption isotherms of PA-POF-1s at (a) 258 K, (b) 273 K, and (c) 298 K; CO<sub>2</sub> adsorption isotherms of PA-POF-2s at (d) 258 K, (e) 273 K, and (f) 298 K.

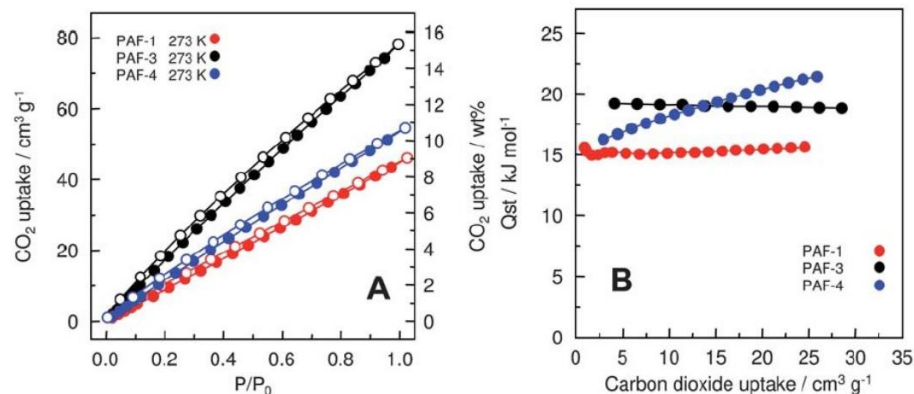


Figure 3-4. (A) CO<sub>2</sub> uptakes at 273K and 1 bar and (B) isosteric heats of CO<sub>2</sub> adsorption (Q<sub>st</sub>) of PAFs. Ref. 10.

As can be seen in Table 3-1 and Figure 3-3, the CO<sub>2</sub> uptake does not directly correlate with the BET surface areas of the materials. For example, PA-POF-2 [0.2:1] possesses the highest BET surface area among all the PA-POFs, but adsorbs slightly less CO<sub>2</sub> than PA-POF-2 [1:1] at all three temperatures. This can be explained by the interactions between CO<sub>2</sub> molecules and the framework. Isosteric heats of CO<sub>2</sub> adsorption (Q<sub>st</sub>) were calculated from the adsorption at three temperatures (258 K, 273 K, and 298 K) using the Clausius-Clapeyron equation which is shown as following:

$$\ln P_q = \frac{\Delta H_q}{RT} + C$$

Q<sub>st</sub> values of all the PA-POFs except PA-POF-1 [0.3:1] vary between 20 kJ mol<sup>-1</sup> and 25 kJ mol<sup>-1</sup> (Figure 3-5), which is higher than PAF-1 (Q<sub>st</sub> = 15 kJ mol<sup>-1</sup>).<sup>10</sup> The higher Q<sub>st</sub> values suggest that PA-POFs have stronger interactions to CO<sub>2</sub> molecules than PAF-1, possibly due to ion-dipole force between the anionic framework and CO<sub>2</sub>. The higher heats

of adsorption may explain why PA-POFs adsorb more CO<sub>2</sub> than PAF-1 despite the smaller surface areas. PA-POF-1 [0.3:1] has a similar Q<sub>st</sub> value as PAF-1 probably due to the low content of phosphorus.

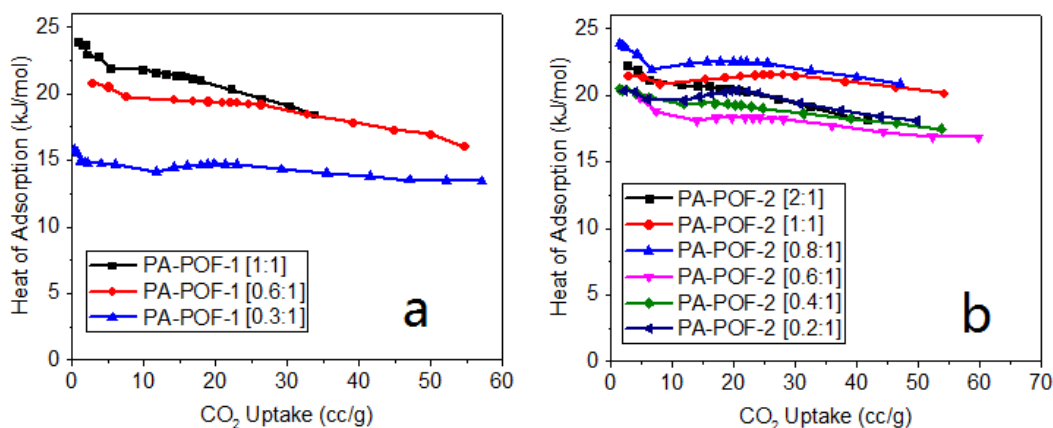


Figure 3-5. Isothermic heats of CO<sub>2</sub> adsorption (Q<sub>st</sub>) of (a) PA-POF-1s and (b) PA-POF-2s.

### 3.3 References

1. Earth System Research Laboratory: <http://www.esrl.noaa.gov/gmd/ccgg/trends/index.html>, 2011.
2. Fischer, H.; Wahlen, M.; Smith, J.; Mastoianni, D.; Deck, B. *Science* 1999, 283, 1712.
3. Demicco, R. V.; Lowenstein, T. K.; Hardie, L. A. *Geology* 2003, 31, 793.
4. R. A. Feely, S. C. Doney and S. R. Cooley, *Oceanography*, 2009, 22, 36–47.
5. Pachauri, R. K.; Reisinger, A. IPCC Fourth Assessment Report, Intergovernmental Panel on Climate Change, 2007.
6. <http://www.world-nuclear-news.org/NN-Tokamak-Energy-turns-on-ST40-fusion-reactor-28041701.html>
7. International Energy Outlook 2016, [https://www.eia.gov/outlooks/ieo/pdf/0484\(2016\).pdf](https://www.eia.gov/outlooks/ieo/pdf/0484(2016).pdf).
8. K. Sumida, D. L. Rogow, J. A. Mason, T. M. McDonald, E. D. Bloch, Z. R. Herm, T.-H. Bae and J. R. Long, *Chem. Rev.*, 2012, 112, 724–781.
9. Klara, S. M.; Srivastava, R. D. *Environ. Prog.* 2002, 21, 247.
10. T. Ben, C. Pei, D. Zhang, J. Xu, F. Deng, X. Jing and S. Qiu, *Energy Environ. Sci.*, 2011, 4, 3991–3999.



11. P. Arab, M. G. Rabbani, A. K. Sekizkardes, T. Islamoglu and H. M. El-Kaderi, *Chem. Mater.*, 2014, 26, 1385.
12. Q. Chen, M. Luo, P. Hammershøj, D. Zhou, Y. Han, B. W. Laursen, C. Yan and B. Han, *J. Am. Chem. Soc.*, 2012, 134, 6084–6087.
13. Y. Zhu, H. Long and W. Zhang, *Chem. Mater.*, 2013, 25, 1630.
14. M. G. Rabbani and H. M. El-Kaderi, *Chem. Mater.*, 2012, 24, 1511.
15. M. G. Rabbani and H. M. El-Kaderi, *Chem. Mater.*, 2011, 23, 1650.
16. M. G. Rabbani, A. K. Sekizkardes, O. M. El-Kadri, B. R. Kaafarani and H. M. El-Kaderi, *J. Mater. Chem.*, 2012, 22, 25409–25417.
17. W. Song, X. Xu, Q. Chen, Z. Zhuang and X. Bu, *Polym. Chem.*, 2013, 4, 4690–4696.
18. P. Puthiaraj, S. Kim and W. Ahn, *Chem. Eng. J.*, 2016, 283, 184.

## Chapter 4

# Rapid adsorption of organic pollutants from water by PA-POFs

### 4.1 Introduction

Water safety is crucial to human life. It is estimated that more than 20 million people die because of waterborne pathogens, in addition to non-fatal infection of more than 200 million people every year.<sup>1</sup> The emerging organic pollutants, such as pesticides and endocrine disrupting compounds are becoming an issue in polluted water/waste water. The discharge of these pollutants into the environment affects not only human beings, but also all living organisms. For example, according to a 7-year, whole-lake study at the Experimental Lakes Area in northwestern Ontario, Canada, the long-term exposure of fathead minnow (*Pimephales promelas*) to  $17\alpha$ -ethynyl estradiol (a synthetic estrogen used in birth-control pills) at low concentrations ( $5\text{--}6\text{ ng L}^{-1}$ ) led to feminization of males and, ultimately, a near extinction of this species in the lake.<sup>2</sup>

Adsorption of hazardous organic compounds is one of the simplest and the most effective methods for the removal of organic pollutants from water. Porous materials play a vital role in water purification processes due to their strong adsorption ability. To date, activated carbons are the most used adsorbent materials to remove organic micropollutants from water because of their high surface areas and economic prices.<sup>3</sup> However, certain weaknesses of these materials such as slow adsorption rate (in hours), low uptake capacity,

difficulty in regeneration (heating to 500 °C with loss of performance), and poor removal of relatively hydrophilic micropollutants are significant drawbacks. Other porous materials such as zeolites,<sup>4</sup> mesoporous silicas,<sup>5</sup> covalent organic frameworks (COFs),<sup>6</sup> porous organic polymers,<sup>7</sup> metal organic frameworks (MOFs),<sup>8,9</sup> and porous non-covalent frameworks,<sup>10</sup> have also been investigated with respect to their adsorption properties towards organic pollutants from water, though slow uptake remains a problem. In 2015, a porous  $\beta$ -cyclodextrin polymer (P-CDP) material was reported to have rapid adsorption towards various organic micropollutants.<sup>11</sup> This material showed outstanding adsorption kinetics towards bisphenol A (BPA), a component that is generally used in polymer production such as phenol resins, epoxy resins and polyesters, and is considered to be one of the most frequently detected pollutants in aquatic environments and in waste water.<sup>12</sup> Figure 4-1 shows the removal of ~ 90% BPA from 1 mL 0.1 mM solution by 1 mg P-CDP in less than 1 min, while under the same conditions, commercial activated carbons (ACs) require more than five minutes to reach equilibrium. However, the maximum BPA adsorption capacity at equilibrium by P-CDP was found to be only 88 mg g<sup>-1</sup>, which is relatively low even compared with ACs. For example, a coconut shell based activated carbon AC-PCB has a maximum BPA uptake of 227 mg g<sup>-1</sup>, with the adsorption equilibrium reached in approximately one hour.<sup>13</sup> To date, the discovery of materials that adsorb organic contaminants with different hydrophilicity in both large quantity and at fast removal rate remains a challenge.

PA-POFs offer such an opportunity because of their high porosity and good thermal stability. In the following context, the BPA adsorption properties of PA-POF materials as

well as the removal of other representative organic micropollutants by PA-POFs are presented.

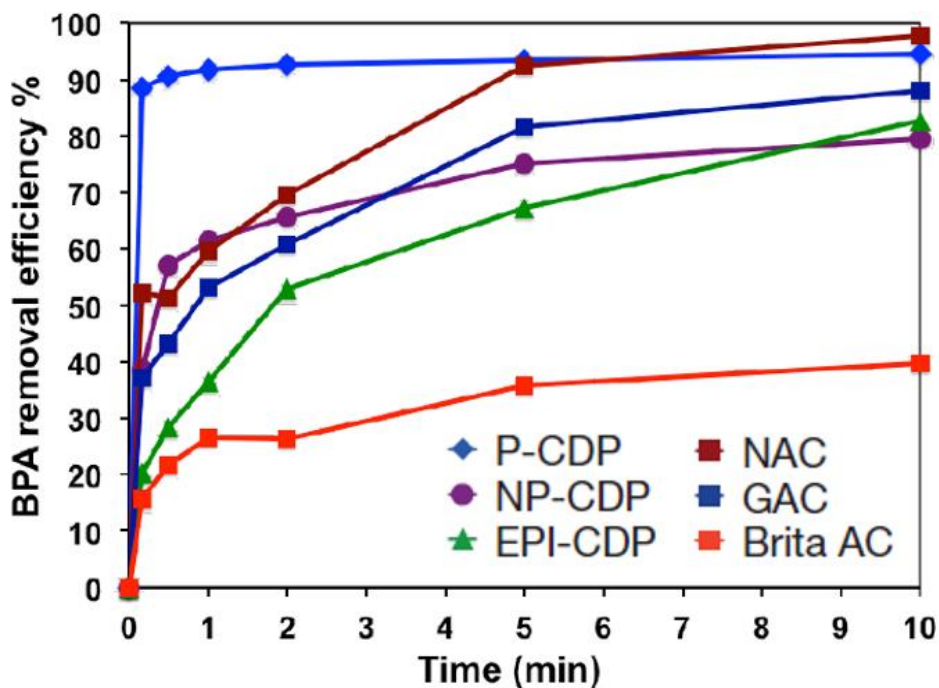


Figure 4-1. Time dependent adsorption of 0.1 mM aqueous bisphenol A ( $1 \text{ mL mg}^{-1}$ ) by each adsorbent. P-CDP: porous  $\beta$ -cyclodextrin polymer ( $S_{\text{BET}} = 263 \text{ m}^2 \text{ g}^{-1}$ ); NP-CDP: nonporous  $\beta$ -cyclodextrin polymer ( $S_{\text{BET}} = 6 \text{ m}^2 \text{ g}^{-1}$ ); EPI-CDP: a non-porous  $\beta$ -cyclodextrin polymer crosslinked with epichlorohydrin ( $S_{\text{BET}} = 23 \text{ m}^2 \text{ g}^{-1}$ ); NAC: Norit RO 0.8 activated carbon ( $S_{\text{BET}} = 984 \text{ m}^2 \text{ g}^{-1}$ ); GAC: DARCO granular activated carbon ( $S_{\text{BET}} = 612 \text{ m}^2 \text{ g}^{-1}$ ); Brita AC: the hybrid AC/ion exchange resin used in commercial Brita point-of-use filters ( $S_{\text{BET}} = 507 \text{ m}^2 \text{ g}^{-1}$ ). Ref. 11.

## 4.2 Methods and materials

2,2-bis(4-hydroxyphenol) propane (BPA), 1-naphthylamine (1-NA), bis(4-hydroxyphenol) sulfone (BPS), 2-naphthol, 2,4-dichlorophenol (2,4-DCP) and propranolol hydrochloride were purchased from TCI. Ethinyl oestradiol, and metolachlor were purchased from Sigma Aldrich. Brita activated carbon was obtained from a Brita on tap

faucet water filter and was ground into fine powder before use. PAF-1 was synthesized following a previously published protocol.<sup>14</sup>

Ultraviolet-visible (UV-Vis) spectroscopy was performed on a Shimadzu UV-2101PC UV-Vis scanning spectrometer. UV-vis spectra were recorded at RT over the range of 200 - 400 nm, and normalized to zero absorbance at 400 nm. The concentrations of the pollutants were calculated from the UV-vis spectra, based on their molar extinction coefficients using Beer's Law: bisphenol A ( $3,343 \text{ M}^{-1} \text{ cm}^{-1}$  at  $\lambda_{\text{max}} = 276 \text{ nm}$ ), bisphenol S ( $20,700 \text{ M}^{-1} \text{ cm}^{-1}$  at  $\lambda_{\text{max}} = 259 \text{ nm}$ ), 2-naphthol ( $4,639 \text{ M}^{-1} \text{ cm}^{-1}$  at  $\lambda_{\text{max}} = 273 \text{ nm}$ ), 1-naphthyl amine ( $5,185 \text{ M}^{-1} \text{ cm}^{-1}$  at  $\lambda_{\text{max}} = 305 \text{ nm}$ ), 2,4-dichlorophenol ( $2,255 \text{ M}^{-1} \text{ cm}^{-1}$  at  $\lambda_{\text{max}} = 284 \text{ nm}$ ), ethinyl oestradiol ( $8,430 \text{ M}^{-1} \text{ cm}^{-1}$  at  $\lambda_{\text{max}} = 220 \text{ nm}$ ), propranolol hydrochloride ( $5,310 \text{ M}^{-1} \text{ cm}^{-1}$  at  $\lambda_{\text{max}} = 290 \text{ nm}$ ) and metolachlor ( $213 \text{ M}^{-1} \text{ cm}^{-1}$  at  $\lambda_{\text{max}} = 15,330 \text{ nm}$ ).

### 4.3 Adsorption of bisphenol A from water by PA-POFs

Firstly, in order to determine which PA-POF material adsorbs the most BPA, the following experiments were conducted. 1 mg of each material (measured using Cahn C-35 microbalance) was stirred in 100 mL 0.1 mM BPA solution at RT for 1 hour (defined as 100 mL  $\text{mg}^{-1}$  adsorption study), after which 4 mL of the suspension was taken *via* a syringe and filtered through a VWR 0.45  $\mu\text{m}$  PTFE syringe filter. The filtrate was collected for UV-vis analysis to determine the residual concentration of the pollutant.

The UV-vis spectra after the adsorption are shown in Figure 4-2. The removal efficiency of each material was calculated using the following equation, and is plotted in Figure 4-3.

$$\text{Pollutant Removal Efficiency} = \frac{C_0 - C_t}{C_0} \times 100\%$$

where  $C_0$  (mmol l<sup>-1</sup>) and  $C_t$  (mmol l<sup>-1</sup>) are the initial and residual concentration of pollutant in the stock solution and the filtrate, respectively.

The amount of pollutant adsorbed by the adsorbent was determined by the following equation:

$$Q_t = \frac{(C_0 - C_t)M_wV}{m}$$

where  $C_0$  (mmol l<sup>-1</sup>) and  $C_t$  (mmol l<sup>-1</sup>) are the initial and residual concentration of pollutant in the stock solution and the filtrate, respectively.  $Q_t$  (mg g<sup>-1</sup>) is the amount of the pollutant adsorbed.  $M_w$  (g mol<sup>-1</sup>) is the molar mass of the pollutant.  $V$  (l) is the volume of the pollutant solution.  $m$  (g) is the mass of adsorbent used in the experiment.

PA-POF-2 [0.8:1] was found to remove ~ 88% of BPA from a 100 mL mg<sup>-1</sup> solution in one hour, corresponding to an equilibrium uptake of 2,015 mg g<sup>-1</sup>, which is the highest among all PA-POFs. Other PA-POF materials such as PA-POF-2 [1:1], PA-POF-2 [0.6:1], and PA-POF-2 [0.4:1] also show good adsorption ability towards BPA with the removal efficiencies over 80%. Compared with the rest of PA-POFs, PA-POF-2 [2:1] showed much smaller removal efficiency of ~ 7%. This small removal efficiency may be due to the homogeneous structure of PA-POF-2 [2:1], resulting in the lack of macropores for easy access of BPA molecules and much longer adsorption pathways. PA-POF-1s have less adsorption of BPA than PA-POF-2s except PA-POF-2 [2:1] probably because of the smaller surface areas of PA-POF-1s. PAF-1 was also tested using the same method and the

removal efficiency was found to be only ~ 4.5%. Even though PAF-1 has a much larger surface area than PA-POFs, it shows little uptake towards BPA.

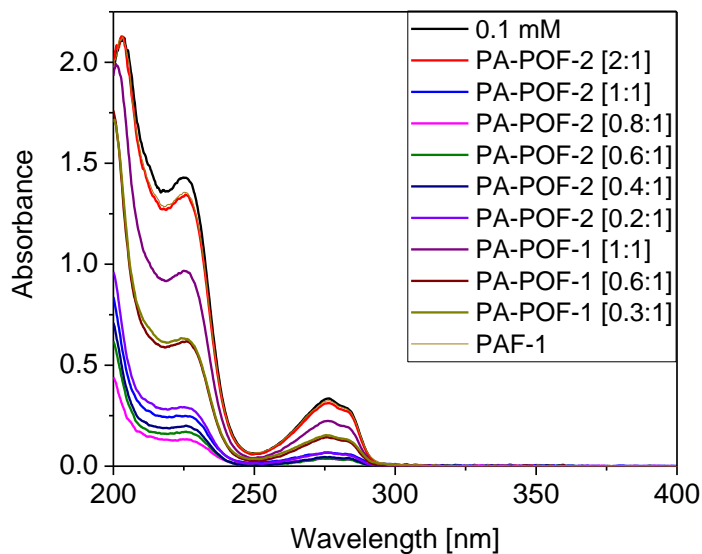


Figure 4-2. UV-vis spectra of BPA solutions after 100 mL mg<sup>-1</sup> adsorption studies for one hour by PA-POFs and PAF-1.

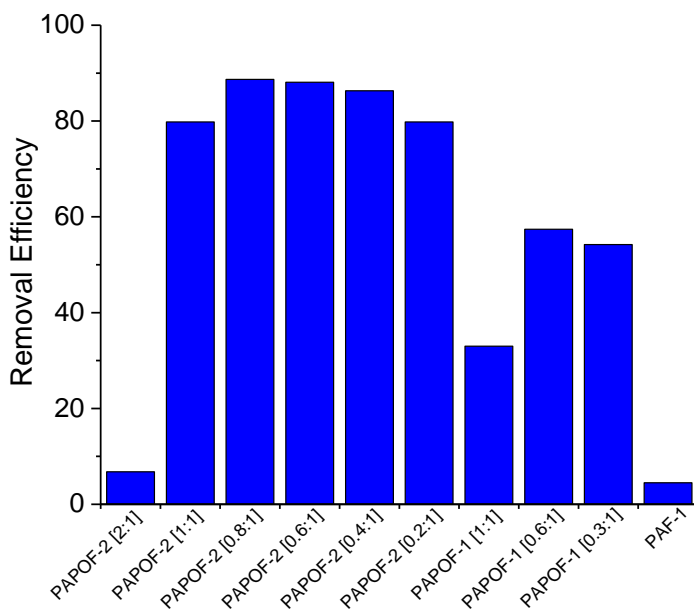


Figure 4-3. Bisphenol A removal efficiency of PA-POFs and PAF-1 from 100 mL mg<sup>-1</sup> 0.1 mM BPA solution.

The adsorption capacity of PA-POF-2 [0.8:1] was further examined by simulating the BPA adsorption isotherms using the following procedures. 1 mg of PA-POF-2 [0.8:1] was stirred in a closed bottle with 40 mL (for 40 mL mg<sup>-1</sup> study), 50 mL (for 50 mL mg<sup>-1</sup> study), until 140 mL (for 140 mL mg<sup>-1</sup> study) 0.1 mM BPA stock solution at RT for one hour to reach equilibrium. 4 mL of the suspension was then taken out *via* a syringe and subsequently filtered through a VWR 0.45 μm PTFE syringe filter. The filtrate was collected and measured by UV-vis spectroscopy and is shown in Figure 4-4. The spectra clearly show a trend that feeding with increased amount of BPA solution, the residual BPA concentration in the filtrate is increased after the treatment. The removal efficiency in each study was calculated and shown in Figure 4-5. A 90% removal efficiency can be reached in one hour when PA-POF-2 [0.8:1] was treated with as much as 80 mL mg<sup>-1</sup> solution.

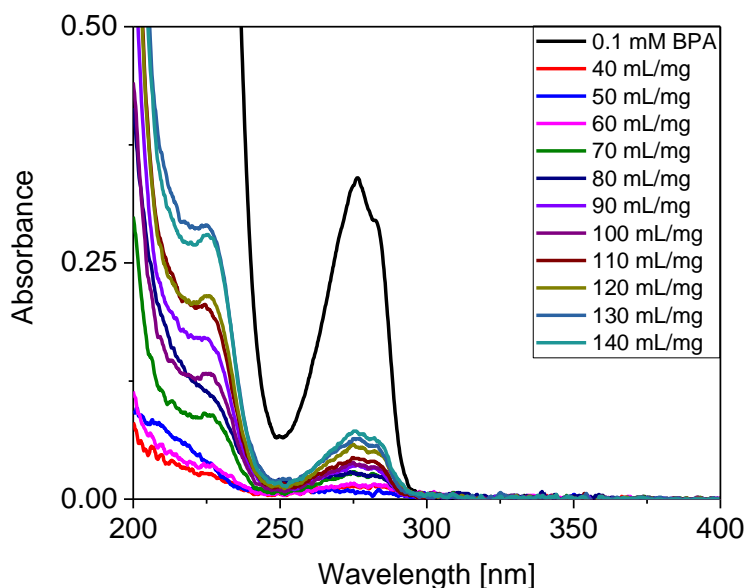


Figure 4-4. UV-vis spectra of BPA solutions after 40-140 mL mg<sup>-1</sup> adsorption studies for one hour by PA-POF-2 [0.8:1].



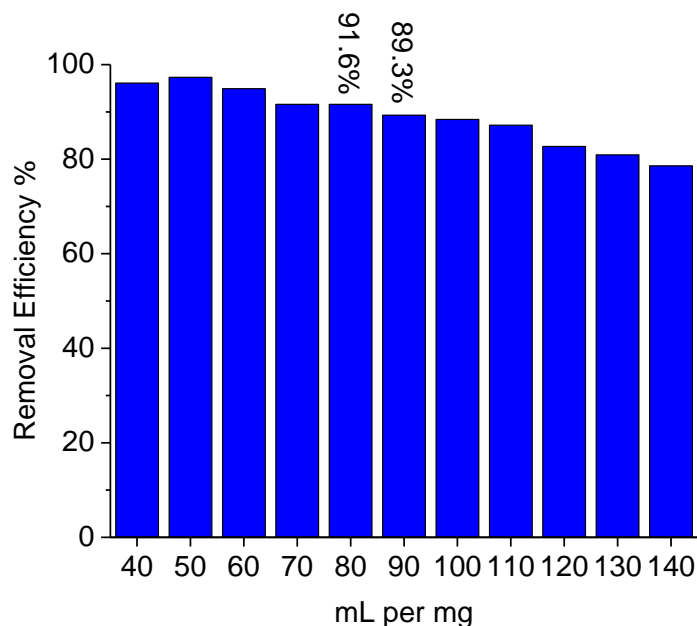


Figure 4-5. Bisphenol A removal efficiency of PA-POF-2 [0.8:1] from 40-140 mL mg<sup>-1</sup> 0.1 mM BPA solution.

Two classic sorption isotherm models, Langmuir and Freundlich models were fitted to the experiment data. The Langmuir isotherm model assumes that the adsorption occurred in a monolayer.<sup>15</sup> The Freundlich model was shown to be in accord with an exponential distribution of active sites which hypothesizes that a multilayer adsorption takes place on the heterogeneous surface.<sup>16</sup> The two models are expressed in the following equations:

Langmuir Model 
$$\frac{1}{Q_e} = \frac{1}{K_L Q_m C_e} + \frac{1}{Q_m}$$

Freundlich model 
$$Q_e = K_F C_e^{1/n}$$

where  $C_e$  (mg L<sup>-1</sup>) and  $Q_e$  (mg g<sup>-1</sup>) are the concentration of the pollutant in the solution after the adsorption and the adsorbate uptake at equilibrium, respectively.  $C_e$  and  $Q_e$  were calculated based on the UV-vis spectrum for each study.  $K_L$  (L mg<sup>-1</sup>) describes the intensity

of the adsorption process, and  $Q_m$  ( $\text{mg g}^{-1}$ ) reflects maximum adsorption capacity.  $K_F$  ( $\text{mg (L mg}^{-1})^{1/n} \text{g}^{-1}$ ) is a constant related to binding energy, and represents the general capacity of adsorbate adsorbed onto adsorbents for a unit equilibrium concentration.  $1/n$  gives an indication of the favorability of adsorption. Values of  $n > 1$  represent favorable adsorption condition.<sup>17</sup>

The BPA uptake of PA-POF-2 [0.8:1] at equilibrium as a function of residual BPA concentration after adsorption was fitted into both models (Figure 4-6). The Langmuir and Freundlich adsorption isotherm parameters are shown in Table 4-1. The maximum adsorption capacity obtained from the Langmuir model was as high as  $3,366 \text{ mg g}^{-1}$ . This adsorption capacity is more than 10 times higher than that of all the published materials. A few examples are selected and presented in Table 4-2 for comparison, for example, Fe/OMC ( $311 \text{ mg g}^{-1}$ ),<sup>19</sup> hydrophobic zeolite ( $125 \text{ mg g}^{-1}$ ),<sup>4</sup> meso-SiO<sub>2</sub> ( $353 \text{ mg g}^{-1}$ ),<sup>20</sup> MIL-101-Cr ( $252.5 \text{ mg g}^{-1}$ ),<sup>22</sup> and activated carbon-PCB ( $227 \text{ mg g}^{-1}$ ).<sup>13</sup> Compared with the Langmuir adsorption capacity of P-CDP ( $88 \text{ mg g}^{-1}$ ), the BPA adsorption capacity of PA-POF-2 [0.8:1] is more than 35 times higher. The  $K_F$  value,  $1,276 \text{ mg g}^{-1} (\text{L mg}^{-1})^{1/n}$  (Table 4-1), obtained from the Freundlich model also indicates a large maximum adsorption capacity. The Langmuir equation makes the assumption of a homogeneous surface monolayer coverage and the Freundlich model is an empirical multilayer adsorption model.<sup>15,16</sup> Based on the correlation coefficient  $R^2$  values, the adsorption isotherm fit is slightly better with the Freundlich model compared to the Langmuir model, suggesting multilayer adsorption rather than monolayer adsorption.

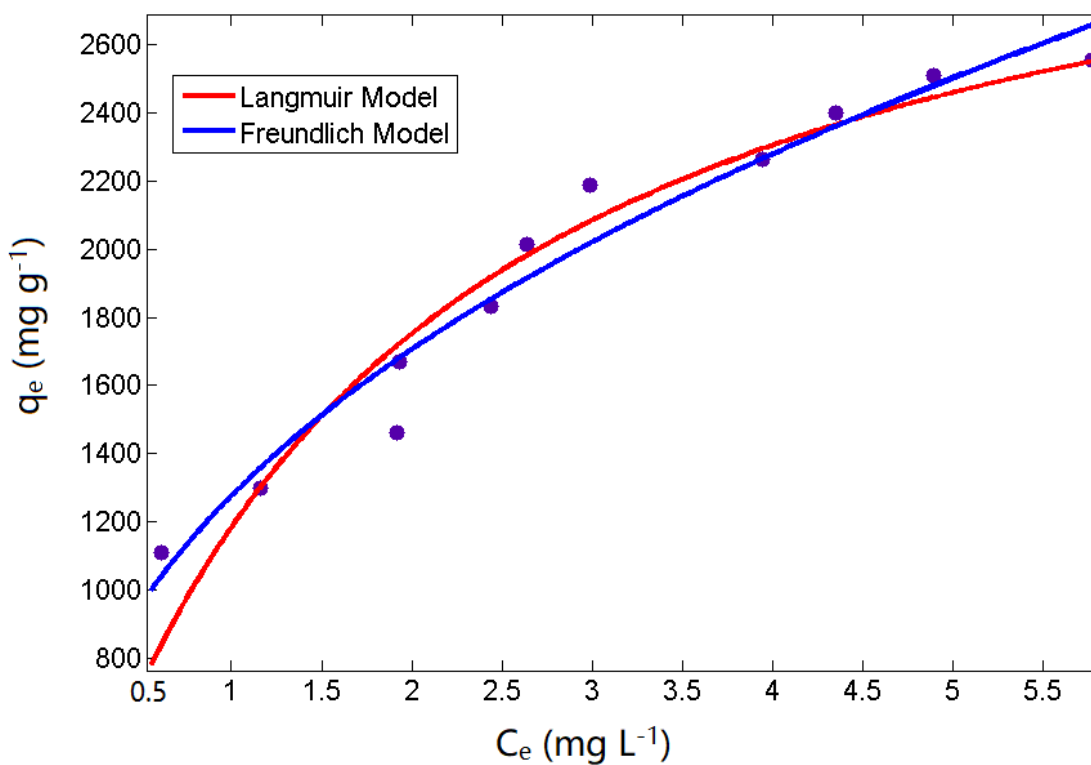


Figure 4-6. Langmuir (red) and Freundlich (blue) adsorption isotherms of BPA by PA-POF-2 [0.8:1].

Table 4-1. Langmuir and Freundlich adsorption isotherm parameters for the adsorption of BPA by PA-POF-2 [0.8:1].

Langmuir			Freundlich		
$q_m$ ( $\text{mg g}^{-1}$ )	$K_L$ ( $\text{L mg}^{-1}$ )	$R^2$	$K_F$	$1/n$	$R^2$
3,366	0.5424	0.9256	1,276	0.4185	0.9527

Table 4-2. The comparison of removal performance of several adsorbents used for BPA removal.

<b>Adsorbent</b>	<b>q<sub>m</sub> (mg g<sup>-1</sup>)</b>	<b>Isothermal Model</b>	<b>References</b>
CNTs/Fe <sub>3</sub> O <sub>4</sub>	46	Freundlich	18
Graphene	182	Langmuir	15
Fe/OMC	311	Freundlich	19
Activated carbon–PCB	227	Freundlich	13
Merck AC, K27350518015	263.1	Langmuir	21
meso-SiO <sub>2</sub>	353	Langmuir	20
MIL-101-Cr	252.5	Langmuir	22
hydrophobic zeolite	141	Redlich–Peterson	4
PA-POF-2 [0.8:1]	3366	Langmuir	This work

The adsorption kinetics of PA-POF-2 [0.8:1] were studied using the following procedures. A glass vial was charged with 1 mg of PA-POF-1 material and 10 mL 0.1 mM BPA aqueous solution. This procedure is called hereafter “the removal of BPA from a 10 mL mg<sup>-1</sup> 0.1 mM BPA solution”. The vial was closed and placed on a stirring plate with a 300 r.p.m stirring rate for a certain amount of time. 4 mL of the aqueous suspension obtained during the adsorption experiment was filtered through a VWR 0.45 μm PTFE syringe filter. The filtrate was collected for UV-vis analysis.

The uptake rate of BPA was determined by a simple and popular model, pseudo-second-order model,<sup>23</sup> shown in the following equation:

$$\frac{t}{Q_t} = \frac{t}{Q_e} + \frac{1}{k_{obs}Q_e^2}$$

where  $Q_t$  ( $\text{mg g}^{-1}$ ) and  $Q_e$  ( $\text{mg g}^{-1}$ ) are the adsorbate uptakes at time  $t$  (min) and at equilibrium, respectively.  $k_{obs}$  ( $\text{g mg}^{-1} \text{min}^{-1}$ ) is the second-order rate constant.

As shown in Figure 4-7, the UV-vis spectra of the filtrates after being treated for different amounts of time are recorded. The absorbance of all the spectra at 276 nm is low, showing great removal efficiencies. The removal efficiency of each removal for different contact time is calculated and plotted in Figure 4-8.

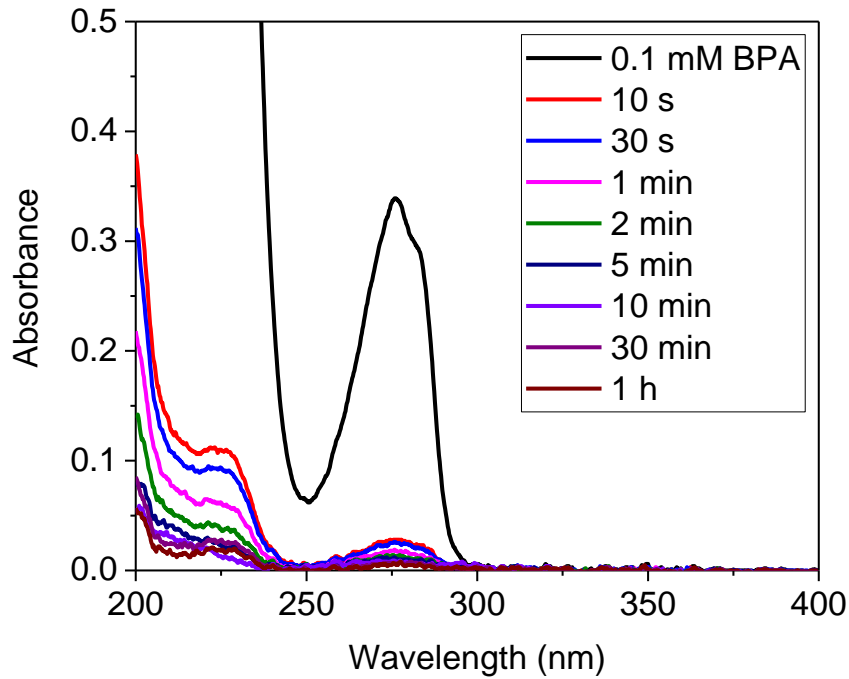


Figure 4-7. UV-vis spectra of the filtrates as a function of contact times for PA-POF-2 [0.8:1].

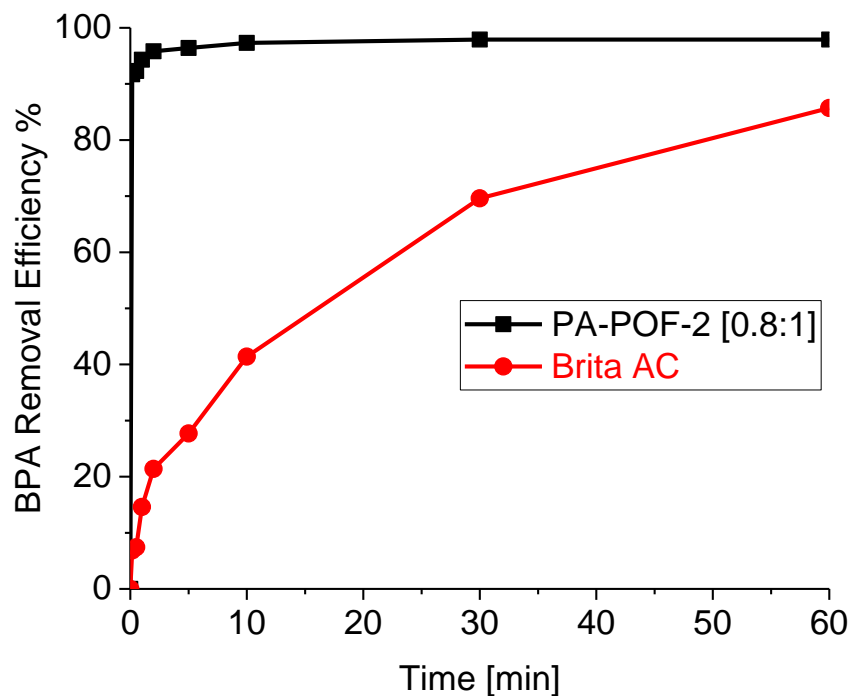


Figure 4-8. Effect of contact time on the adsorption of 10 mL mg<sup>-1</sup> BPA by PA-POF-2 [0.8:1] and Brita AC.

As can be seen in Figure 4-8, PA-POF-2 [0.8:1] removes 98% of BPA from a 10 mL mg<sup>-1</sup> solution when the equilibrium is reached. More importantly, the removal reached its equilibrium in less than 2 min, with 91% removal efficiency reached in 10 s. For comparison, P-CDP, a material that so far possesses the record for fast BPA removal rate, removes 90% BPA in 10 s,<sup>11</sup> however the amount of BPA adsorbed was 10 times less (a 1 mL mg<sup>-1</sup> solution was used for P-CDP compared to the 10 mL mg<sup>-1</sup> solution used for PA-POF-2 [0.8:1]). The uptake kinetics were determined by a pseudo-second-order adsorption model. As shown in Figure 4-9, the equation fit with the data very well showing a correlation coefficient R<sup>2</sup> value 0.99998 and a pseudo-second-order rate constant ( $k_{obs}$ ) of 0.15 g mg<sup>-1</sup> min<sup>-1</sup>. The adsorption capacity at equilibrium estimated by the kinetic model,

$q_e = 222 \text{ mg g}^{-1}$ , also coincided with the experimental data,  $q_e(\text{exp}) = 223 \text{ mg g}^{-1}$ . The kinetic model shows that 35 s contact time is enough to reach 95% of equilibrium adsorption capacity for PA-POF-2 [0.8:1], which is  $211 \text{ mg g}^{-1}$  adsorption in 35 s. For comparison, the time-dependent adsorption of a commercially available activated carbon (AC), Brita AC, was also tested using the same method, as shown in Figure 4-8. In 10 seconds, only 6.4% BPA was adsorbed by Brita AC, showing a much slower uptake rate compared with the removal efficiency of 91% reached in 10 s by PA-POF-1 material. In 30 minutes, only 70% removal efficiency was achieved for the Brita AC and the equilibrium was still not reached.

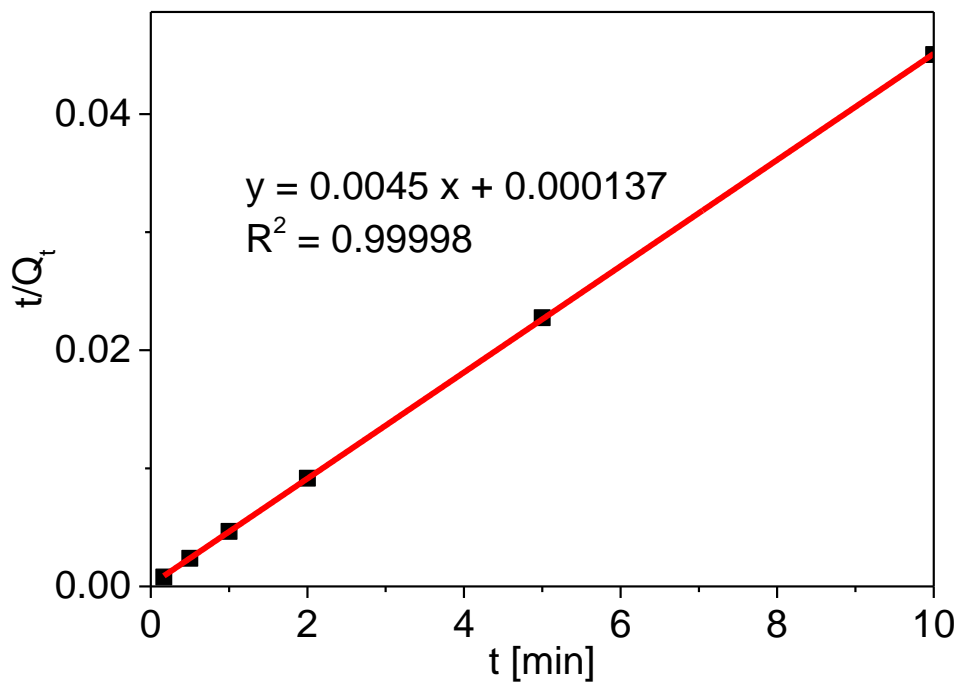


Figure 4-9. Pseudo-second-order plot of the PA-POF-2 [0.8:1] kinetics study ( $q_e = 222 \text{ mg g}^{-1}$ ,  $k_{\text{obs}} = 0.15 \text{ g mg}^{-1} \text{ min}^{-1}$ ).

Regeneration and reuse of an adsorbent are essential for practical applications. In this study, regeneration experiments for used PA-POF-2 [0.8:1] was conducted using a simple methanol washing procedure, and the regenerated material was evaluated for its removal efficiency in an 80 mL mg-1 solution. A detailed procedure is listed below.

1 mg of PA-POF-2 [0.8:1] was placed in a glass vial equipped with a magnetic stirring bar, to which 80 mL 0.1 mM BPA solution was added. The mixture was stirred at RT for 1 hour, and 4 mL of the suspension was taken *via* a syringe and then filtered through a VWR 0.45  $\mu\text{m}$  PTFE syringe filter. The filtrate was collected and measured by UV-vis spectroscopy. PA-POF-2 [0.8:1] was regenerated by washing with MeOH (10 mL x 3) and recovered by filtration. PA-POF-2 [0.8:1] was then dried in vacuo and collected for the next cycle. This adsorption-desorption cycle was performed five times as shown in Figure 4-10. The data shown are the average of triplicate experiments.

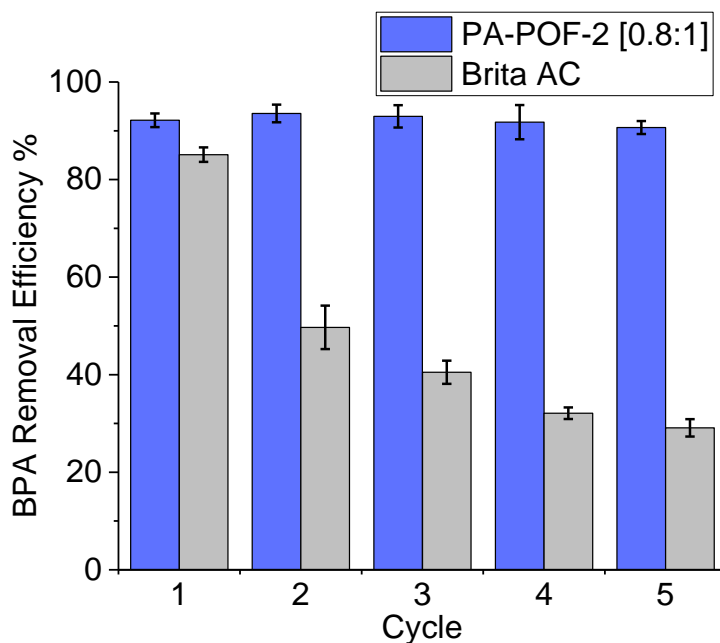


Figure 4-10. The average percentage BPA removal efficiency by PA-POF-2 [0.8:1] and Brita AC after regeneration cycles.



As shown in Figure 4-10, no significant decrease in removal efficiency was observed for the as-synthesized material in at least five cycles. In each cycle, more than 90% removal efficiency was achieved, indicating no loss in the performance of PA-POF material. Brita AC was tested with 10 mL mg<sup>-1</sup> BPA solution, and regenerated using the same method, however decreased performance in each cycle was found (Figure 3d). For the first cycle by Brita AC, an 85% removal efficiency was reached in one hour. In the second cycle, it was observed that only 49% efficiency was reached, showing a 42% loss in the performance. Then the performance keeps decreasing in each cycle by nearly 20%, until only 29% removal efficiency was observed in the fifth cycle.

To further support recyclability of PA-POF-2 [0.8:1], solid phase extraction experiments were conducted. The procedures of solid phase extraction experiments are described as follows. 1 mg of PA-POF-2 [0.8:1] was placed in a glass vial equipped with a magnetic stirring bar, to which 10 mL 0.1 mM BPA solution was added. The mixture was stirred at RT for 10 min, and 4 mL of the suspension was taken using a syringe and filtered through a VWR 0.45 μm PTFE syringe filter. The filtrate was collected and measured by UV-vis spectroscopy. PA-POF-2 [0.8:1] was regenerated by washing with MeOH (5 mL x 3) and recovered by filtration. PA-POF-2 [0.8:1] was dried in vacuo and collected for the next cycle. The methanol washing filtrate was evaporated, and the residual solid was dissolved in 10 mL DI water and measured by UV-vis spectroscopy to determine whether BPA that had been adsorbed by PA-POF-2 [0.8:1] could be fully extracted by MeOH. This adsorption-desorption-recovery cycle was performed three times as shown in Figure 4-11.

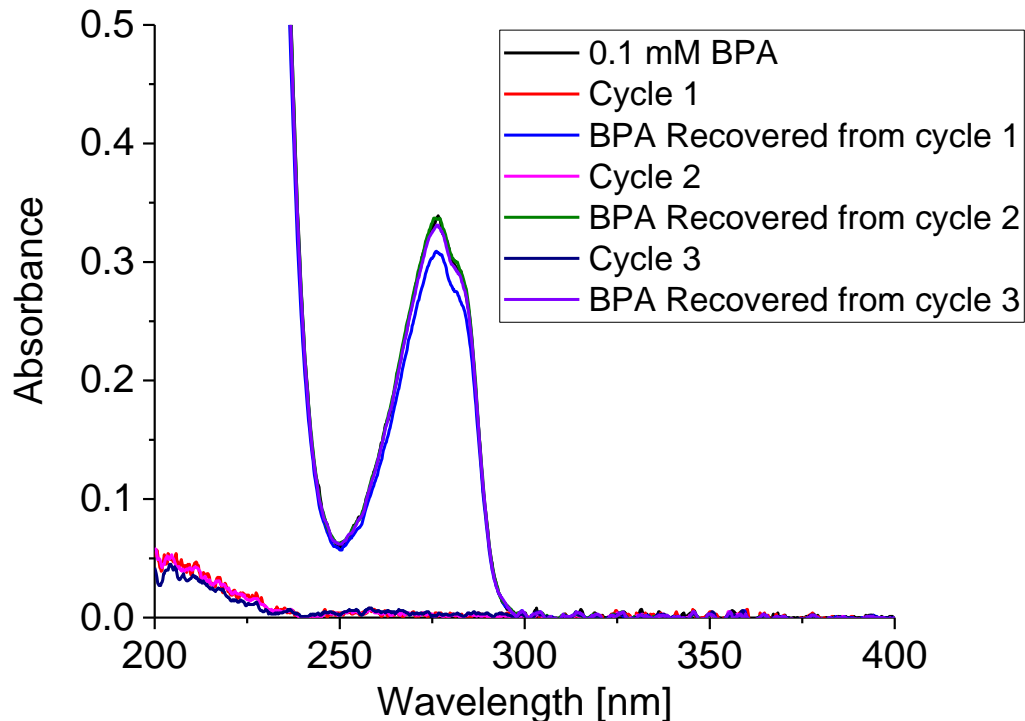


Figure 4-11. The UV-vis spectra of the filtrate after adsorption and the redissolved BPA solution recovered by extraction with MeOH.

Figure 4-11 shows the UV-Vis spectra of the solutions obtained from the solid phase extraction experiments. The UV absorbance at 276 nm of the filtrates are significantly lower than the stock solution and close to zero, showing that more than 95% of BPA from the treated solution was removed by PA-POF-2 [0.8:1] in each cycle. The UV-vis absorbance of BPA recovered from MeOH in each cycle equals the absorbance of the stock BPA solution which proves that all the BPA adsorbed by adsorbents can be fully extracted by MeOH. The spectra clearly show that adsorbed BPA can be fully washed out using methanol for at least three cycles.

## 4.4 Adsorption of various organic micropollutants from water by PA-POFs

To better elucidate its rapid removal ability for different organic pollutants with variable size and functionality, PA-POF-2 [0.8:1] was also treated with a number of other micropollutants. These pollutants are described as following: 2-naphthol, a model for various naphthol compounds; 1-naphthyl amine, a known carcinogen and precursor to a variety of dyes;<sup>24</sup> bisphenol S, a substitute of BPA in some epoxies but also a known endocrine disruptor, and even more resistant to environmental degradation than BPA;<sup>25</sup> metolachlor, a widely used herbicide which induces cytotoxic and genotoxic effects in human lymphocytes;<sup>26</sup> ethinyl oestradiol, an orally active oestrogen used in combined oral contraceptives that may cause male feminization of fathead minnow at concentrations as low as 5-6 ng L<sup>-1</sup>;<sup>2</sup> propranolol hydrochloride, a beta blocker which is used for the treatment of high blood pressure; and 2,4-dichlorophenol, an intermediate in herbicide production and degradation product of the antibacterial agent triclosan.<sup>27</sup>

Similar adsorption studies were performed with these compounds by treating 10 mL of each solution with 1 mg of PA-POF-2 [0.8:1]. The UV-vis spectra recorded at different contact time (10 s to 1 hour) of each pollutant and the corresponding time dependent removal efficiency are shown in Figure 4-12 and Figure 4-13. It is obvious that PA-POF-2 [0.8:1] rapidly removes each organic pollutant with more than 90% efficiency in 10 minutes, and the time dependent removal curves are similar to that of BPA. For example, the removal of 10 mL mg<sup>-1</sup> 0.1 mM metolachlor reached its equilibrium value in 1 minute and over 96% removal efficiency was achieved.

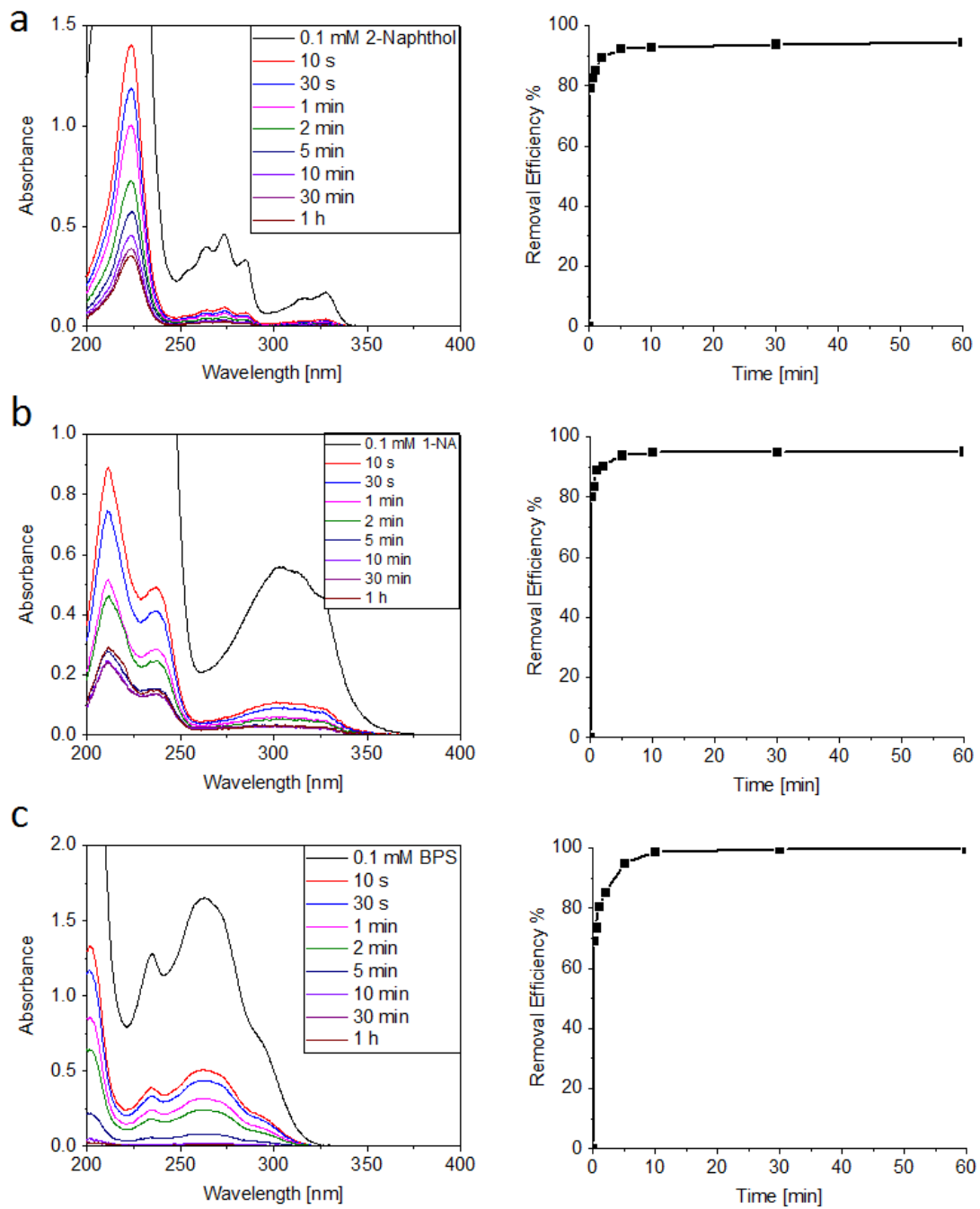


Figure 4-12. UV-vis spectra recorded at different contact time and time dependent removal efficiency of 10 mL mg<sup>-1</sup> (a) 0.1 mM 2-naphthol, (b) 0.1 mM 1-naphthyl amine, and (c) 0.1 mM bisphenol S.

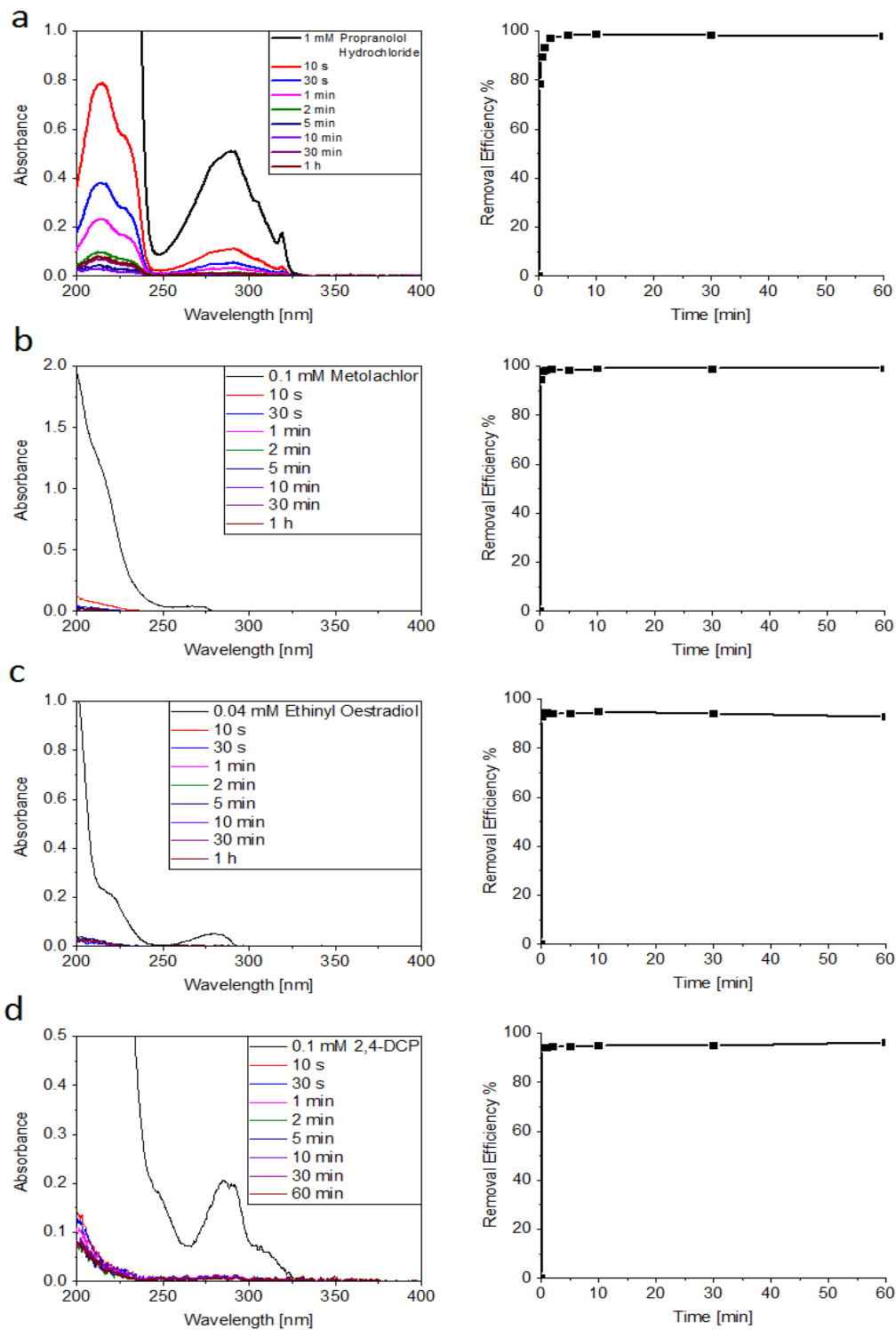


Figure 4-13. UV-vis spectra recorded at different contact time and time dependent removal efficiency of 10 mL mg<sup>-1</sup> (a) 0.09 mM propranolol hydrochloride, (b) 0.1 mM metolachlor, (c) 0.04 mM ethinyl oestradiol, and (d) 0.1 mM 2,4-dichlorophenol.

The outstanding performance of PA-POF-2 [0.8:1] can also be seen visually if a colored pollutant is used. 4-nitrophenol was chosen as the pollutant for two reasons. First, 4-nitrophenol is a relatively hydrophilic organic compound. Secondly, the aqueous solution of 4-nitrophenol has a bright yellow color even at low concentrations. As shown in the supporting video 1, 4 mg of PA-POF-2 [0.8:1] was transferred into a vial which contained 4 mL 0.1 mM 4-nitrophenol solution. After a couple of shakes, the color disappeared immediately. For comparison, PAF-1 and Brita AC were not able to effectively adsorb 4-nitrophenol under the same conditions. The remarkable performance of the PA-POF material for adsorbing organic contaminants suggests potential application for the removal of multiple contaminants that span a wide range of molecular weight, polarity, and functional groups.

## 4.5 Summary and discussion

The adsorption properties towards organic pollutants from water by PA-POFs were systematically discussed. The PA-POF materials suggest excellent BPA adsorption capacity. In a 100 mL mg<sup>-1</sup> study, PA-POFs remove as much as 88% BPA from the solution within one hour. Compared with 4.5% removal efficiency of PAF-1, the removal capacities of PA-POFs are enormous. Since the linkers in the frameworks of PA-POFs and PAF-1 are both tetraphenyl methane, this huge difference is surprising. Given that PA-POFs are built through the co-condensation reactions between TTBP/LTBP and TBPM, while PAF-1 is only built by TBPM, the reason of the huge uptakes should be attributed to the addition of TTBP/LTBP during the polymerization. The anionic building blocks, TTBP/LTBP, might behave as templating agents in the polymerization, and promote the formation of the

structure that is preferable for the adsorption of organic molecules. PA-POF-2 [0.8:1] was found to have a maximum Langmuir adsorption capacity of 3366 mg g<sup>-1</sup>. This adsorption capacity is more than ten times higher than those of all reported high-performance adsorption materials in BPA removal.

Before the discovery of PA-POFs, it was reported the fastest removal rate in the adsorption of a variety of organic micropollutants by P-CDP, with pseudo-second-order rate constants ( $k_{obs}$ ) 15 to 200 times greater than those of activated carbons.<sup>11</sup> For example, the  $k_{obs}$  of BPA adsorption to P-CDP was 1.5 mg g<sup>-1</sup> min<sup>-1</sup>, and the authors claimed that this number is 15 times higher than activated carbons and two or more orders of magnitude higher than the other studied adsorbents. However, a greater number of  $k_{obs}$  does not always represent a higher removal rate. For example, PA-POF-2 [0.8:1] adsorbs 10 times more BPA in the same time range, yet the  $k_{obs}$  is only 0.15 mg g<sup>-1</sup> min<sup>-1</sup> (Figure 4-9). This result can be explained by the following pseudo-second-order model equation.<sup>11</sup>

$$\frac{t}{Q_t} = \frac{t}{Q_e} + \frac{1}{k_{obs}Q_e^2}$$

The physical meaning of  $Q_t$  and  $Q_e$  is mg(adsorbate) per g(adsorbent). The physical meaning of the rate constant  $k_{obs}$  is g(adsorbent) per mg(adsorbate) per minute. If the mass of the adsorbent and the mass of the adsorbate are constant and the time required for reaching equilibrium is shorter, the value of  $k_{obs}$  is of course greater. In this case, a larger number for  $k_{obs}$  means faster kinetics. However, if the amount of sorbent is constant but the amount of adsorbed adsorbate is larger, the value of  $k_{obs}$  actually gets smaller. For example, if 1 g of material A adsorbs 1 mg adsorbate in 1 minute, then  $k_{obs}$  (A) = 1 g mg<sup>-1</sup> min<sup>-1</sup>; if 1 g material B adsorbs 10 mg adsorbate in 1 minute,  $k_{obs}$  (B) = 0.1 g mg<sup>-1</sup> min<sup>-1</sup>.

In this case, a larger value of  $k_{\text{obs}}$  does not mean faster but slower kinetics. To give another example, if 100 g material C adsorbs 0.1 mg adsorbate in 10 minutes,  $k_{\text{obs}}(\text{C}) = 100 \text{ g mg}^{-1} \text{ min}^{-1}$ , which is a high value, however it doesn't mean faster kinetics. Even though this is not exactly how  $k_{\text{obs}}$  was calculated, it helps for a better understanding of the meaning of  $k_{\text{obs}}$ . One can conclude from here that the reason of a smaller pseudo-second-order rate constant of PA-POF-2 [0.8:1] than P-CDP is the higher BPA uptake.

PA-POF-2 [0.8:1] was also studied for its regeneration ability. Experiments proved that a convenient methanol-washing procedure was able to regenerate PA-POF-2 [0.8:1] without significant loss in performance. In contrast, Brita AC was found to lose more than 65% in removal efficiency after five regeneration cycles. The solid phase extraction experiments show that the adsorbed BPA in PA-POF-2 [0.8:1] can be fully recovered from the methanol-washing filtrate.

It is also noteworthy that PA-POF-2 [0.8:1] removes various organic pollutants of different size, functionality, and hydrophobicity. The pollutants studied span simple aromatic compounds such as 2,4-dichlorophenol, pesticides such as metolachlor, and pharmaceuticals such as ethinyl oestradiol. In all the studies, PA-POF-2 [0.8:1] removes more than 90% of the pollutants from water within 5 minutes and equilibrium concentrations are reached in 10 minutes. This result further supports the fast and massive removal of organic pollutants from water by PA-POF material.



## 4.6 Reference

1. P. Leonard, S. Hearty, J. Brennan, L. Dunne, J. Quinn, T. Chakraborty, R. O’Kennedy, *Enzyme Microb. Technol.*, **2003**, 32, 1, 3–13.
2. K. A. Kidd, P. J. Blanchfield, K. H. Mills, V. P. Palace, R. E. Evans, J. M. Lazorchak, R. W. Flick, *PNAS*, **2007**, 104, 8897.
3. W. Tsai, C. Lai, T. J. Su, *J. Hazard. Mater.*, 2006, 134, 169–175.
4. W. Tsai, H. Hsu, T. Su, K. Lin, C. Lin, *J. Colloid Interface Sci.*, 2006, 299, 513–519.
5. Y. H. Kim, B. Lee, K. H. Choo, S. J. Choi, *Micropor. Mesopor. Mater.*, 2011, 138, 184–190.
6. S. Yu, H. Lyu, J. Tian, H. Wang, D. Zhang, Y. Liu, Z. Li, *Polym. Chem.*, 2016, 7, 3392–3397.
7. H. Ou, Q. You, J. Li, G. Liao, H. Xia, D. Wang, *RSC Advances*, 2016, 6, 98487–98497.
8. N. A. Khan, Z. Hasan, S. H. Jhung, *J. Hazard. Mater.*, 2013, 244, 444–456.
9. S. Yao, T. Xu, N. Zhao, L. Zhang, Q. Huo, Y. Liu, *Dalton Trans.*, 2017, 46, 3332–3337.
10. T. Chen, I. Popov, W. Kaveevivitchai, Y. Chuang, Y. Chen, O. Daugulis, A. J. Jacobson, O. S. Miljanic, *Nature Comm.*, 2014, 5, 5131.
11. A. Alsaiee, B. J. Smith, L. Xiao, Y. Ling, D. E. Helbling, W. R. Dichtel, *Nature*, 2016, 529, 190.
12. K. Choi, S. Kim, C. Kim, S. Kim, *Chemosphere*, 2005, 58, 1535–1545.
13. W. T. Tsai, C. W. Lai, T. Y. Su, *J. Hazard. Mater.*, 2006, 134, 169–175.
14. T. Ben, H. Ren, S. Ma, D. Cao, J. Lan, X. Jing, W. Wang, J. Xu, F. Deng, J. Simmons, S. Qiu, G. Zhu, *Angew. Chem. Int. Ed.*, 2009, 48, 9457–9460.
15. J. Xu, L. Wang, Y. Zhu, *Langmuir*, 2012, 28, 8418–8425.
16. Z. Yu, S. Peldszus, P. M. Huck, *Water Res.*, 2008, 42, 2873–2882.
17. Y. Ho, G. McKay, *Chem. Eng. J.*, 1978, 70, 115–124.
18. S. Li, Y. Gong, Y. Yang, C. He, L. Hu, L. Zhu, L. Sun, D. Shu, *Chem. Eng. J.*, 2015, 260, 231–239.
19. L. Tang, Z. Xie, G. Zeng, H. Dong, C. Fan, Y. Zhou, J. Wang, Y. Deng, J. Wang, X. Wei, *RSC Adv.*, 2016, 6, 25724–25732.
20. X. Fan, B. Tu, H. Ma, X. Wang, *Bulletin of the Korean Chemical Society*, 2011, 32, 2560–2564.
21. I. Bautista-Toledo, M. Ferro-García, J. Rivera-Utrilla, C. Moreno-Castilla, F. J. Vegas-Fernández, *Environmental Science & Technology*, 2005, 39, 6246–6250.
22. F. Qin, S. Jia, Y. Liu, H. Li, S. Wu, *Desalin. Water. Treat.*, 2014, 93–102.
23. Y. Ho, G. McKay, *Process Biochem.*, 1999, 34, 451–465.
24. G. Booth, *Ullmann’s Encyclopedia of Industrial Chemistry: Naphthalene Derivatives*, Wiley-VCH, Weinheim, Germany 2012.

25. M. Mathew, S. Sreedhanya, P. Manoj, C. T. Aravindakumar, U. K. Aravind, *J. Phys. Chem. B*, 2014, 118, 14, 3832–3843.
26. B. Roloff, D. Belluck, L. Meiser, *Mut. Res. Lett.*, 1992, 281, 4, 295–298.
27. D. E. Latch, J. L. Packer, B. L. Stender, J. Vanoverbeke, W. A. Arnold, K. Mcneill, *Environ. Toxicol. Chem.*, 2005, 24, 517–525.

## Chapter 5

# Synthesis of a periodic mesoporous crystalline aluminosilicate material

The discovery of mesoporous silicas in 1992 was intended to replace microporous zeolites for long-chain hydrocarbon cracking.<sup>1</sup> However, it was soon found that mesoporous silicas were not able to fulfill the task because of the lacking of catalytically active acidic sites. In order to incorporate acidity into the silica framework, heteroatoms such as Al have been introduced. The synthesis of such amorphous aluminosilica materials was discussed in Chapter 1.3.2. Still, the application of amorphous aluminosilica materials in the petrochemical industry was limited because of the inferior hydrothermal stability of the amorphous pore channel walls. In Chapter 1.3.3, strategies to crystallize the amorphous pore channel walls of mesoporous silicas were discussed. Among all the techniques, Kuroda's work that a strong flux of  $\text{Li}^+$  induced the crystallization from a silica colloidal crystal to a single crystalline mesoporous quartz superlattice is especially important because it introduced an easy and scalable method to produce single crystalline mesoporous silica materials.<sup>2</sup> So far, no such attempts using the flux-grown technique were applied to crystallize mesoporous materials other than mesoporous silica. Herein, the flux-grown technique was expanded to a mesoporous aluminosilica material. The research led to the synthesis of a periodic mesoporous hexagonal spodumene material, and its corresponding acidity was investigated.

## 5.1 Experimental methods and procedures

### 5.1.1 Materials and methods

Pluronic P123 triblock copolymer was purchased from BASF. Lithium nitrate, TEOS, furfuryl alcohol, and oxalic acid was purchased from Sigma Aldrich.  $\text{Al}_2(\text{SO}_4)_3 \cdot x\text{H}_2\text{O}$  was purchased from Alfa Aesar. All the materials were used as received without further purification.

Powder X-ray diffraction (PXRD) data were obtained on a Rigaku MiniFlexII instrument using  $\text{Cu K}\alpha$  radiation. The Rietveld refinements of the XRD pattern were calculated using the PDXL software (Rigaku). The small-angle X-ray scattering (SAXS) patterns were recorded using an Anton Paar SAXSpace instrument. Samples were placed into the hole of an aluminium sample holder and secured on both sides using tape. Gas adsorption measurements were taken with a Quantachrome AS-1 instrument. The samples were outgassed 6 hours at 300 °C prior to measurement. The pore size distributions of the materials were calculated using the Barrett-Joyner-Halenda (BJH) model from the adsorption branch of the isotherm. The surface area was determined using the multipoint BET method in the relative pressure range between 0.05 and 0.3. Transmission electron microscopy (TEM) images were recorded on a JEOL 2000FX instrument operated at an accelerating voltage of 200 kV. Energy dispersive X-ray spectroscopy (EDS) was carried out using Oxford ISIS EDS with a light element detector connected with the TEM. The samples were ground and dispersed in acetone, then drop-casted onto copper grid supported carbon films (SPI supplies). One pulse  $^{29}\text{Si}$ ,  $^{27}\text{Al}$  and  $^7\text{Li}$  solid state NMR spectra were obtained on a Bruker Avance III HD 400 MHz instrument with a spin rate of 12 kHz. Samples were packed into 4 mm outer diameter zirconia rotors and inserted into a Bruker

magic angle spinning (MAS) probe. The  $^{29}\text{Si}$  chemical shift was referred to 3-(Trimethylsilyl)-1-propanesulfonic acid sodium salt at 0 ppm as an external reference standard. The  $^{29}\text{Si}$  pulse length was 5  $\mu\text{s}$  with the recycle delay time of 30 s. The spinning rate of the rotors was 12 kHz. The number of scan is between 3000 to 4000. The  $^{27}\text{Al}$  MAS NMR spectra were recorded using 1  $\mu\text{s}$  pulse length and 1 s recycle delays. The MAS rotors were spun at 12 kHz. The  $^{27}\text{Al}$  chemical shift was referenced to  $\text{AlCl}_3 \cdot 6\text{H}_2\text{O}$  at 0 ppm as an external reference standard. The  $^7\text{Li}$  chemical shift was referred to  $\text{LiCl}$  at 0 ppm as an external reference standard. The silicon/aluminum contents of LAS materials were determined using an Inductively Coupled Plasma Optical Emission Spectrophotometer (ICP-OES, PerkinElmer Optima 2000 DV). The samples for ICP-OES were prepared as follows: 10 mg of material was dissolved in 20 mL 5% HF solution at RT. The solution was later neutralized to  $\text{pH} = 7$  using ammonium hydroxide solution and then quantitatively diluted as needed.

#### 5.1.2 Synthesis of mesoporous aluminosilica material (Al-SBA-15)

The mesoporous aluminosilica material with a two-dimensional hexagonal structure was synthesized following the in situ pH adjusting method similar to literature procedures.<sup>3,4</sup> In a typical synthesis, 0.8 g of Pluronic P123 (PEO-PPO-PEO) triblock copolymer was dissolved in 25 ml of 2 M HCl solution at a temperature of 40 °C by vigorously magnetic stirring in a closed polypropylene bottle. 1.7 g of tetraethoxysilane (TEOS) was then added to this solution. After stirring for 4 h, 1.36 g of  $\text{Al}_2(\text{SO}_4)_3 \cdot x\text{H}_2\text{O}$  ( $x = 14-18$ ) was added to the mixture and stirring was continued for 1 day at the initial synthesis temperature. The whole solution was hydrothermally treated for 2 days at 100 °C.

Then, the pH of the reaction mixture was adjusted to 7.5 by adding concentrated  $\text{NH}_4\text{OH}$  solution drop-wise and then again treated hydrothermally for 2 days at 100 °C. The resulting material was then centrifuged, washed with deionized water, and dried in an oven at 80 °C. Finally, the surfactant was removed by calcination under air at 550 °C (heating ramp rate = 2 °C  $\text{min}^{-1}$ ) for 5 h to obtain white mesoporous aluminosilica material, Al-SBA-15.

### 5.1.3 Li induced crystallization of Al-SBA-15

Lithium nitrate (80 mg), oxalic acid (8 mg) and Al-SBA-15 (100 mg) were mixed and ground into fine powders in a mortar. Lithium nitrate was used as a flux and the oxalic acid was used as an acid catalyst for the polymerization of furfuryl alcohol. The powder mixture was transferred into a Schlenk tube. Into the tube, 2 mL furfuryl alcohol was added, followed by the evacuation for 15 min to allow the infiltration of the furfuryl alcohol into the pores of Al-SBA-15. Then, the wet sample was transferred to an alumina boat crucible and the crucible was placed into an alumina tube furnace. Furfuryl alcohol polymerized at 90 °C for 3 days under Ar atmosphere. Later, the tube furnace was heated to 870 °C at a heating rate of 5 °C  $\text{min}^{-1}$ , and kept at 870 °C under Ar atmosphere for 30 min. This procedure is to carbonize the polymer and induce the crystallization of Al-SBA-15. The obtained black sample was then calcined in air at 550 °C for 6 h to remove the carbon support. A grey powder sample was collected after the combustion for subsequent characterizations.

## 5.2 Results and Discussions

### 5.2.1 Characterization of mesoporous aluminosilica material (Al-SBA-15)

Nitrogen adsorption was used to characterize the mesoporosity of Al-SBA-15 (Fig. 5-1). The nitrogen isotherm shows a capillary condensation step between  $P/P_0 = 0.6$  to  $P/P_0 = 0.8$  indicating that the material is mesoporous. The material has a specific BET surface area of  $324 \text{ m}^2 \text{ g}^{-1}$ , a pore volume of  $0.64 \text{ cm}^3 \text{ g}^{-1}$  and a BJH pore size of  $\sim 7.2 \text{ nm}$  with narrow distribution (Figure 5-2). TEM image of Al-SBA-15 was taken to visualize the mesopores in Al-SBA-15 material. As shown in Figure 5-3, mesopores with a pore size of about  $7 \text{ nm}$  can be clearly seen on TEM images. SAED pattern shows that the material is amorphous. The material is only composed of Al, Si and O as shown in EDS spectrum.

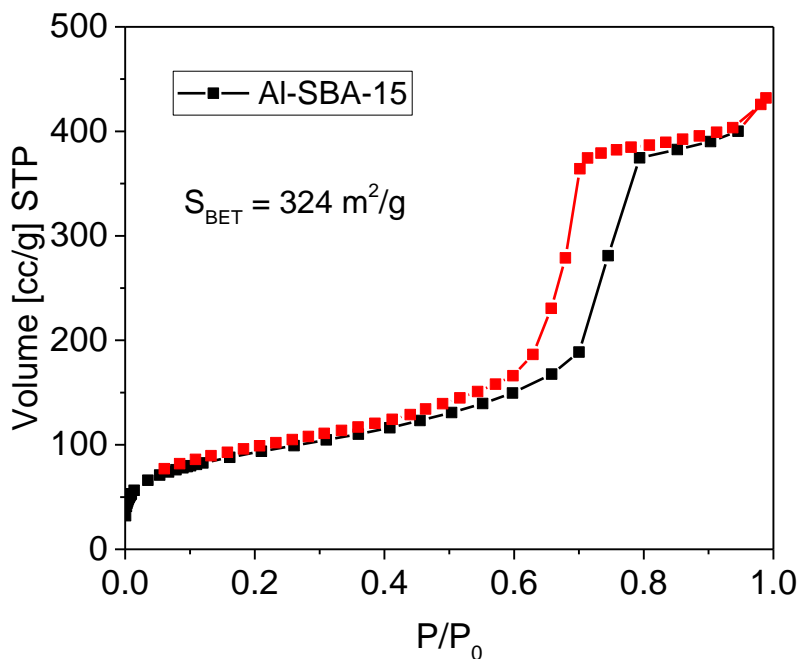


Figure 5-1. Nitrogen adsorption isotherm of Al-SBA-15.

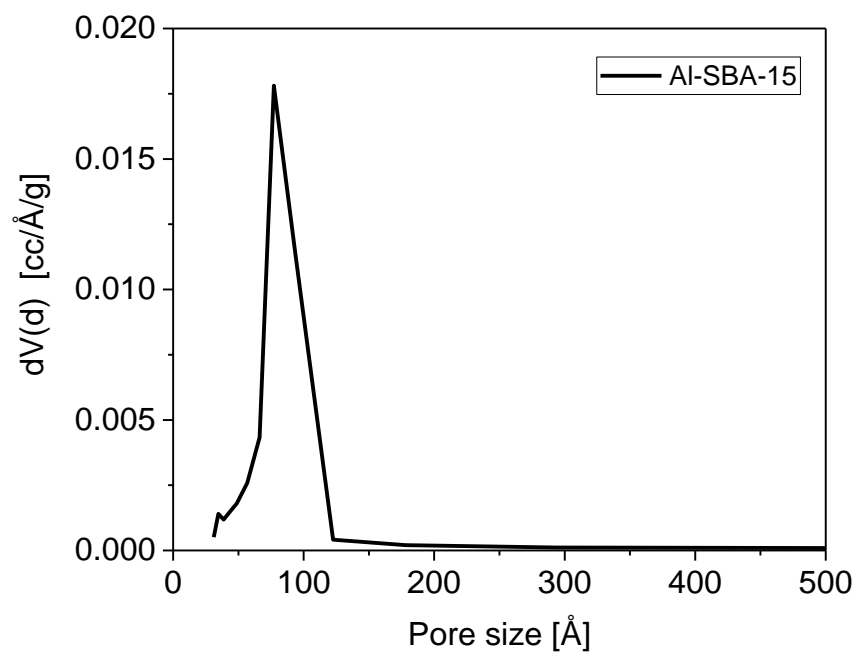


Figure 5-2. Pore size distribution of Al-SBA-15 calculated by BJH method from the adsorption branch.



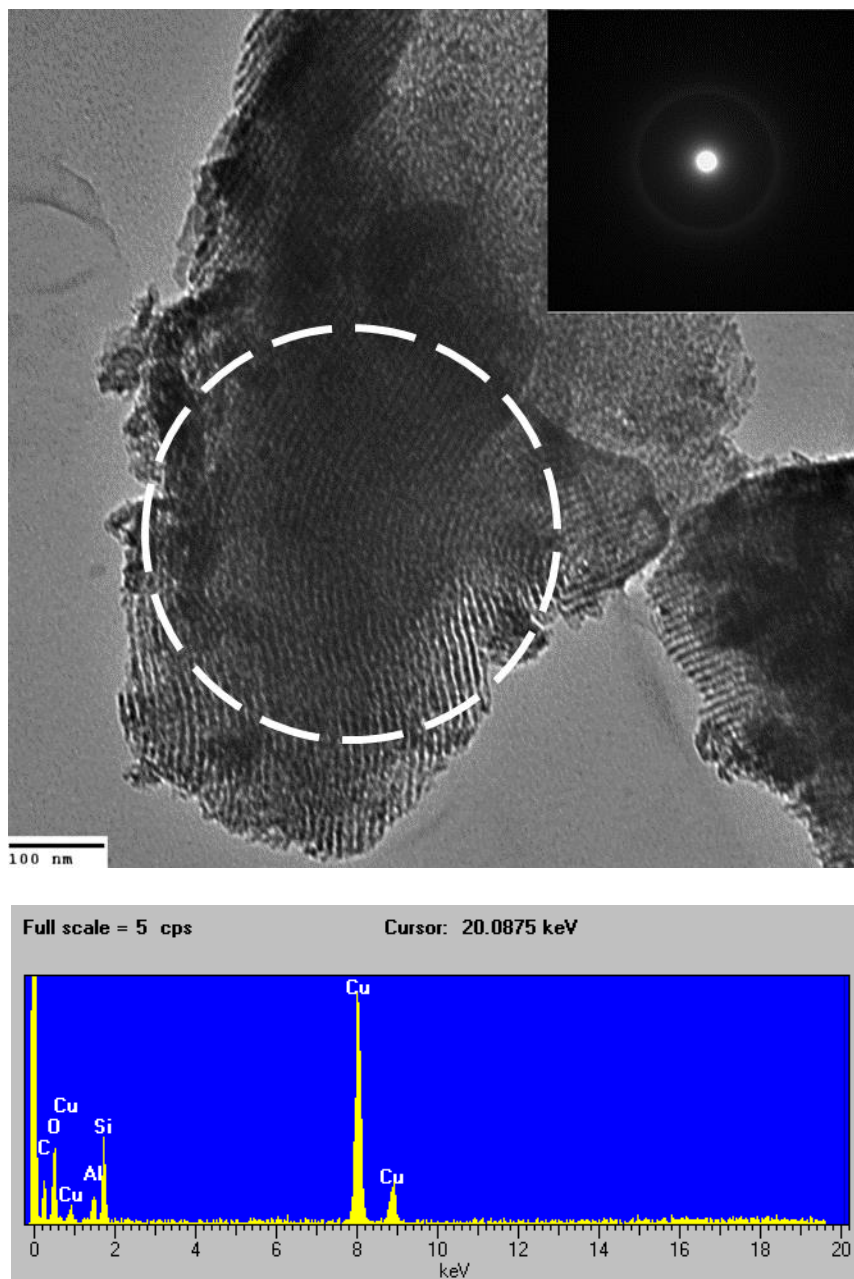


Figure 5-3. Top: TEM image of Al-SBA-15 (inset shows corresponding SAED pattern collected from the encircled area). Bottom: EDS spectrum of Al-SBA-15.

### 5.2.2 Characterization of lithium aluminosilicate (LAS)

The PXRD pattern of the as-synthesized LAS material shows successful crystallization of Al-SBA-15 (Figure 5-4). The peaks with the highest intensity are assigned to hexagonal

lithium aluminosilicate ( $\text{LiAlSi}_2\text{O}_6$ , JCPDS card 01-073-2336). The rest of the peaks can be assigned to two kinds of lithium silicates,  $\text{Li}_2\text{SiO}_3$  (JCPDS card 00-029-0829) and  $\text{Li}_4\text{SiO}_4$  (JCPDS card 01-076-1085). By quantitatively analyzing the XRD pattern using WPPF method (Figure 5-5), the as-synthesized LAS material was found to contain 58.3 wt% hexagonal spodumene, 30.8 wt%  $\text{Li}_2\text{SiO}_3$ , and 10.9 wt%  $\text{Li}_4\text{SiO}_4$ . Based on the quantitative analysis result, a Si/Al ratio of 3.51:1 by mole is thus calculated. The actual Si/Al content ratio of the as-synthesized LAS was determined by Inductively Coupled Plasma Optical Emission Spectrophotometer (ICP-OES). A Si/Al mole ratio of 3.71:1 was obtained by ICP-OES. This result is in good accordance with the quantitative analysis from XRD data.

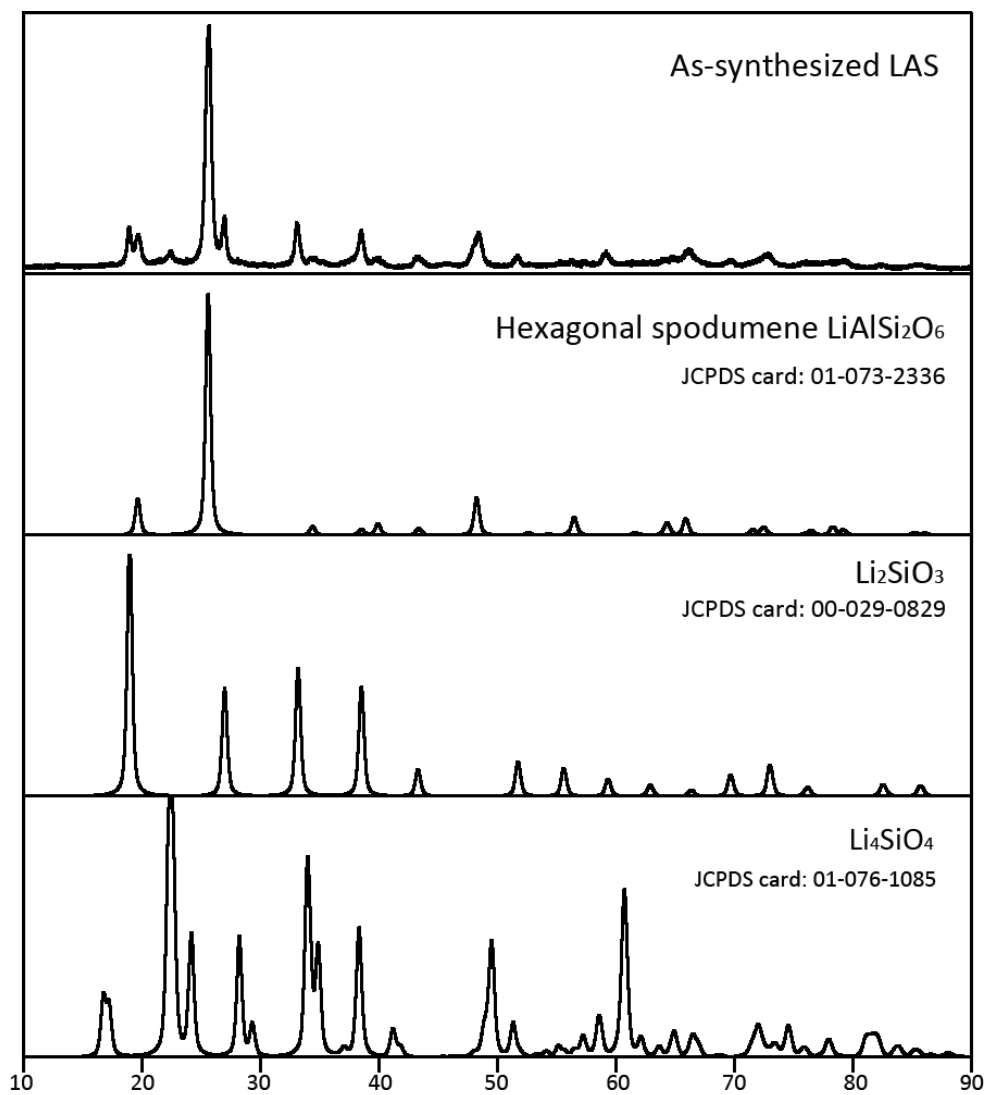


Figure 5-4. XRD pattern of as-synthesized LAS material, compared with hexagonal spodumene,  $\text{Li}_2\text{SiO}_3$ , and  $\text{Li}_4\text{SiO}_4$ .

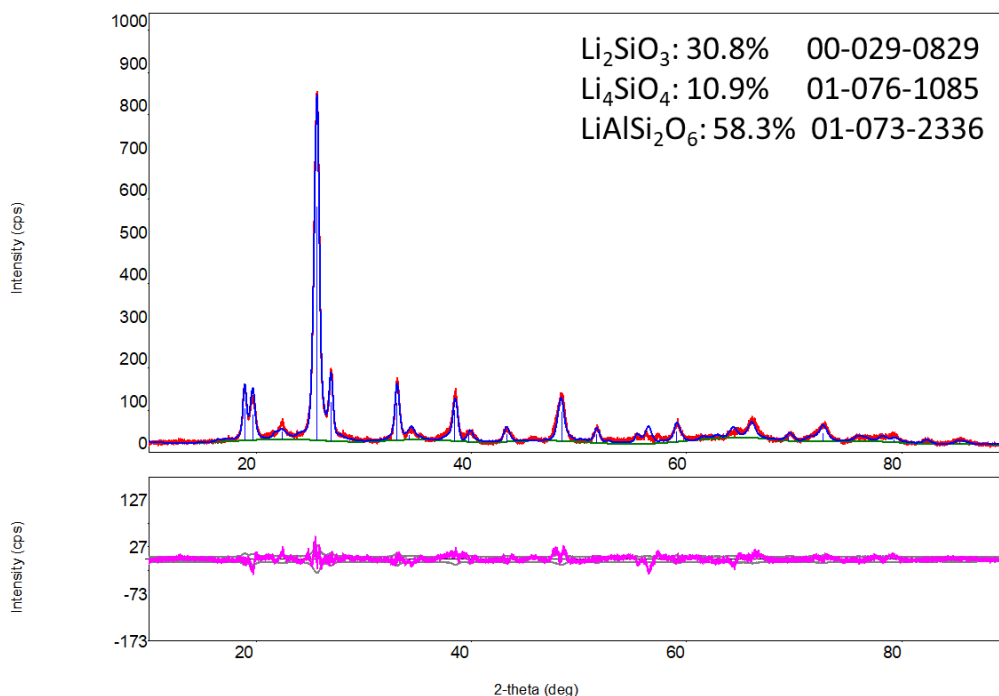


Figure 5-5. Quantitative analysis (WPPF method) of as-synthesized LAS material. Relative percentages of crystalline phases are shown in the upper-right corner. The blue line is the original pattern; the red line is the calculated pattern using crystal information from JCPDS cards listed in the graph; the purple line in the lower box shows the errors.

Nitrogen adsorption analysis, SAXS, and TEM were used to confirm the periodic mesoporosity in the as-synthesized LAS material. The nitrogen sorption isotherm (Figure 5-6) showed the hysteresis loop at relative pressure of 0.5 to 0.7, proving the mesoporosity of the material. The isotherm also showed macroporosity in the material. The apparent BET surface area was  $85 \text{ m}^2 \text{ g}^{-1}$ , and the BJH pore volume was  $0.23 \text{ cm}^3 \text{ g}^{-1}$ . The decrease in the surface area and pore volume is probably due to a higher density of the crystalline pore channel walls compared with the amorphous pore walls and the deterioration of some mesostructures. The BJH pore size distribution is centered at about 5 nm (Figure 5-7). In Figure 5-8, Al-SBA-15 exhibits well-resolved diffraction peaks that can be indexed as the

(100), (110), (200), (210), and (300) diffractions associated with  $p6mm$  hexagonal symmetry. The SAXS pattern of the as-synthesized LAS material confirmed the periodic mesostructure, however, the peaks at higher angles are missing showing that the mesostructure was not as ordered as the starting Al-SBA-15 material, which is consistent with nitrogen sorption data. The (100) peak in the SAXS pattern of as-synthesized LAS is at higher angle than the (100) peak in Al-SBA-15. The unit cell parameter ( $a$ ) was calculated from the SAXS pattern, which is 11 nm for Al-SBA-15 and 10.2 nm for LAS, which suggested a smaller pore size of LAS compared with Al-SBA-15. The smaller pore size in LAS could be caused by the smaller sizes of carbon support than the pores. During the crystallization, some pore walls collapse, and smaller pores form based on the sizes of carbon supports. The wider pore size distribution of the as-synthesized material (Figure 5-7) could be explained by the uneven size distribution of carbon support.

TEM images of as-synthesized LAS material were also taken to examine its pore structure. As shown in Figure 5-9, the well-retained ordered mesopore structure can be easily observed.

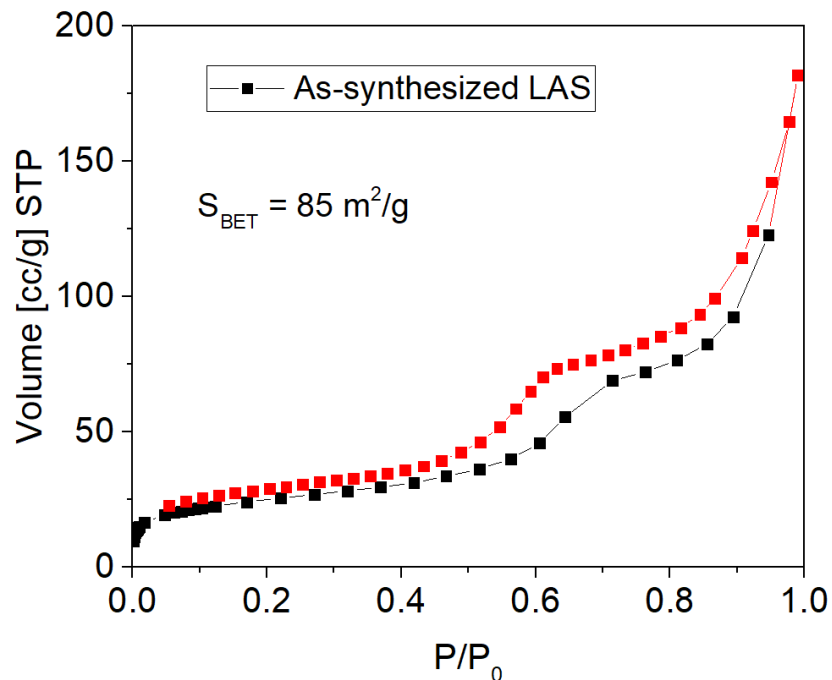


Figure 5-6. Nitrogen adsorption isotherm of as-synthesized LAS material.

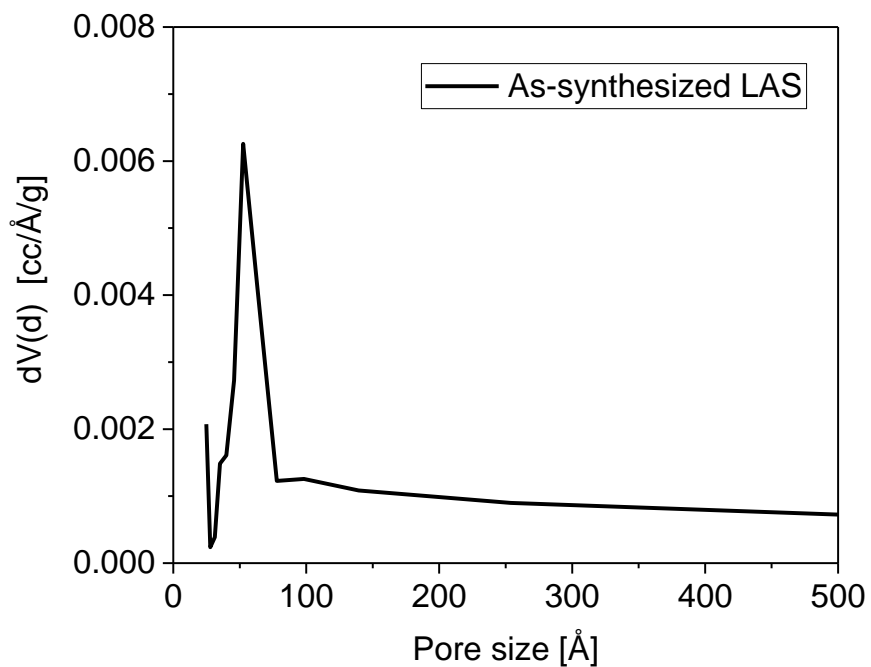


Figure 5-7. BJH pore size distribution of as-synthesized LAS calculated from the adsorption branch.

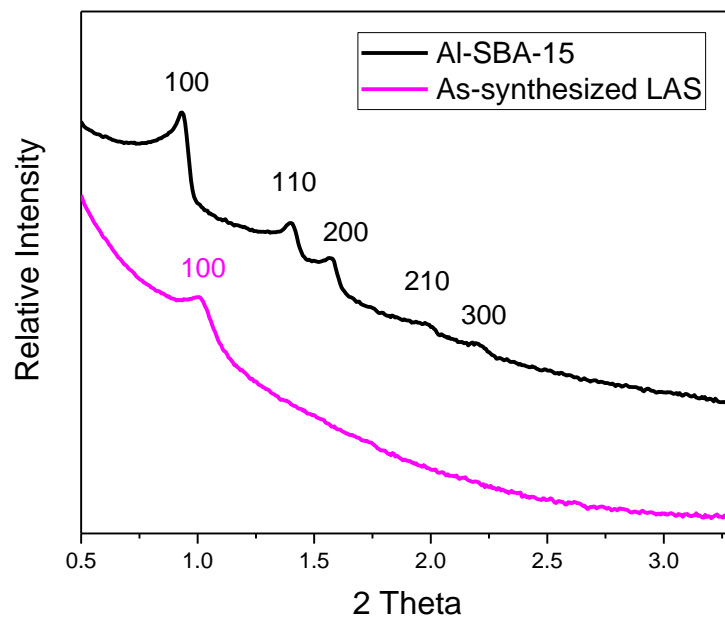


Figure 5-8. SAXS patterns of Al-SBA-15 and as-synthesized LAS material.

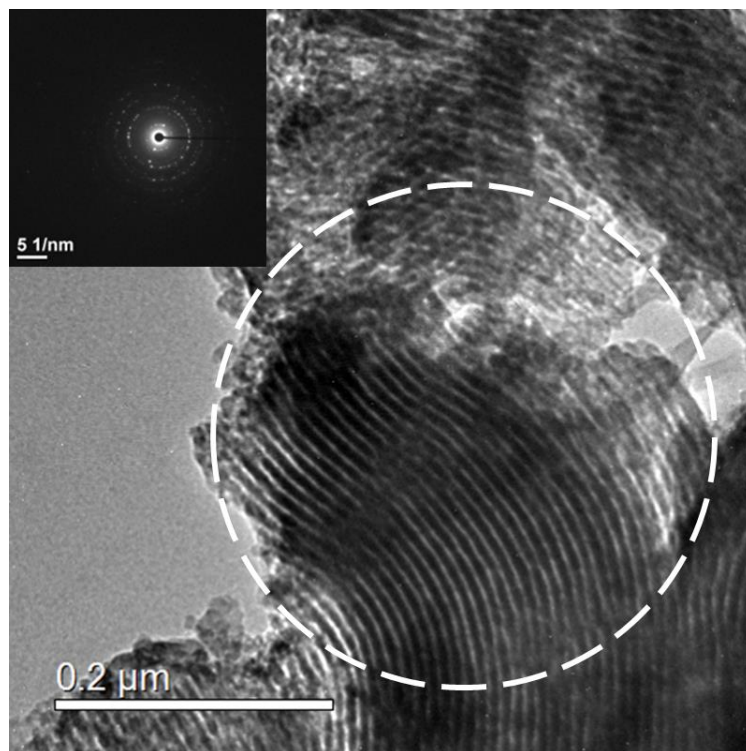


Figure 5-9. TEM image of as-synthesized LAS (inset shows corresponding SAED pattern collected from the encircled area).

The  $^{29}\text{Si}$ ,  $^{27}\text{Al}$  and  $^7\text{Li}$  solid state NMR spectra were used to characterize the as-synthesized LAS material. As shown in Figure 5-10, the chemical shift of the  $^{29}\text{Si}$  NMR signal in Al-SBA-15 is centered at -118 ppm. While the as-synthesized LAS has two major peaks at -75 ppm and -103 ppm. The peak at -75 ppm can be assigned to  $\text{Li}_2\text{SiO}_3$ ,<sup>5</sup> which shows a composition of about 30% from XRD data. The signal of  $\text{Li}_4\text{SiO}_4$ , which should be at -65 ppm,<sup>6</sup> is probably covered by the peak of  $\text{Li}_2\text{SiO}_3$ . The peak at -103 ppm can be assigned to hexagonal spodumene. The  $^{29}\text{Si}$  NMR chemical shift value of hexagonal spodumene is not reported in the literature, but it is probably comparable to the chemical shift of beta-quartz because hexagonal spodumene is a high quartz solid solution (space group  $P6_222$ ).<sup>7</sup> The  $^{29}\text{Si}$  NMR chemical shift of beta-quartz resides at -102 ppm,<sup>8</sup> which is similar to the observation in Fig. 5-10.



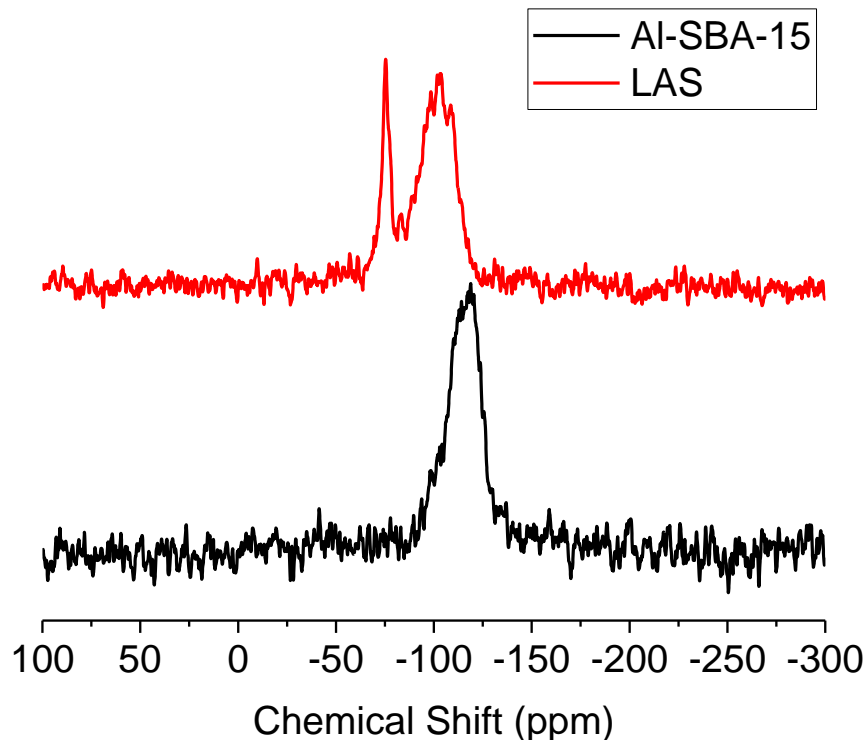


Figure 5-10.  $^{29}\text{Si}$  solid state NMR spectra of Al-SBA-15 and as-synthesized LAS.

The  $^{27}\text{Al}$  solid state NMR spectra of Al-SBA-15 and as-synthesized LAS material is shown in Figure 5-11. Significant differences in  $^{27}\text{Al}$  chemical shifts in LAS as compared with the starting material can be observed from the spectra. The major peak in Al-SBA-15 is located at 4 ppm, which represents octahedrally coordinated  $\text{AlO}_6$  species. Relatively broad and small components were found at  $\sim 30$  ppm and  $\sim 60$  ppm. These peaks are possibly due to  $\text{AlO}_5$  and  $\text{AlO}_4$  species, respectively. As shown in Figure 5-11, the main peak in the  $^{27}\text{Al}$  spectrum of as-synthesized LAS is found to be at 60 ppm, which means that after the crystallization the majority of Al atoms in the material have a coordination number of 4. This result is desired because it proved the existence of a large amount of

[AlO<sub>4</sub>] species, which can potentially act as Brønsted acid sites. In zeolites the latter are the key active sites for a number of catalysis processes in the petrochemical industry. The <sup>7</sup>Li NMR spectrum of LAS confirmed the presence of Li<sup>+</sup> ions in the material (Figure 5-12).

Raman spectroscopy was also used to confirm the formation of hexagonal spodumene. As shown in Figure 5-13, the sharp signal at 480 cm<sup>-1</sup> in Raman spectrum of the LAS material is in accordance with the literature value for hexagonal spodumene.<sup>9</sup>

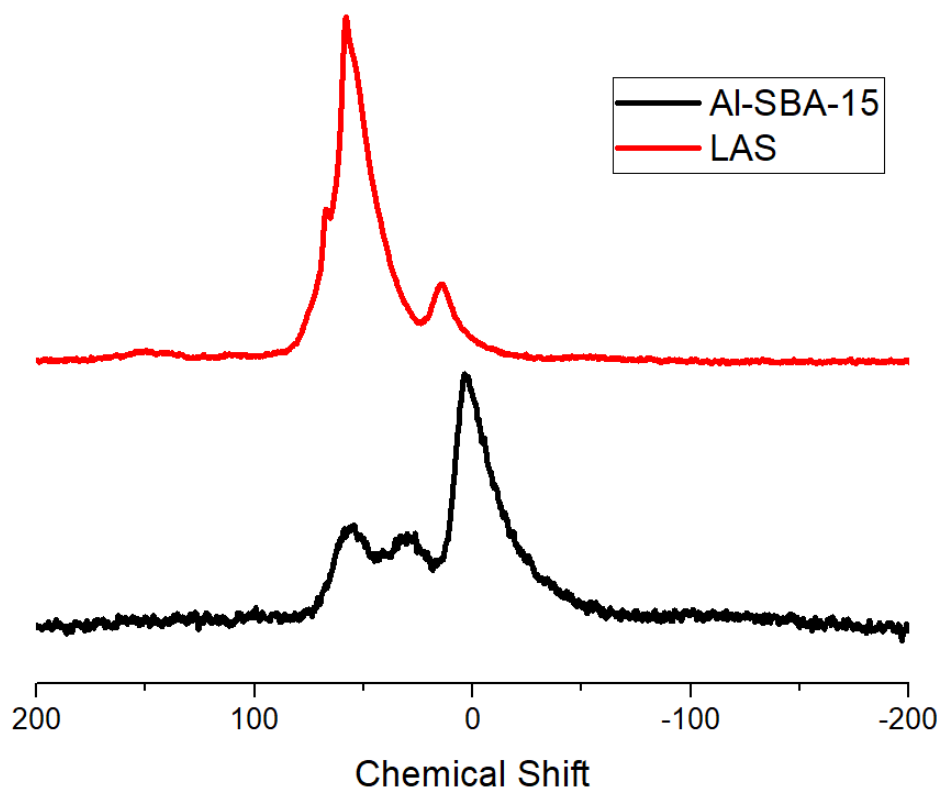


Figure 5-11. <sup>27</sup>Al solid state NMR spectra of Al-SBA-15 and as-synthesized LAS.

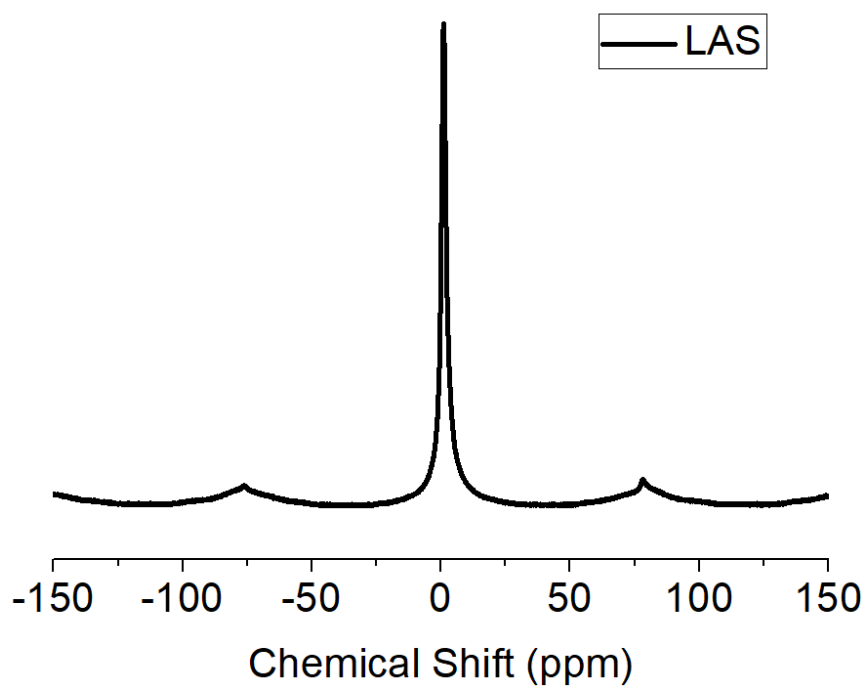


Figure 5-12.  ${}^7\text{Li}$  solid state NMR spectrum of as-synthesized LAS.

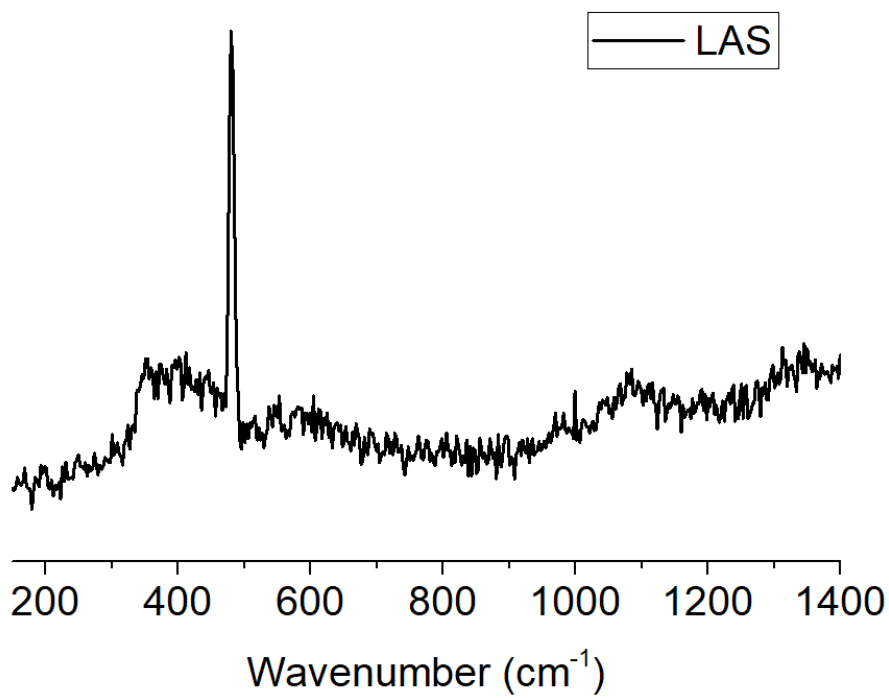


Figure 5-13. Raman spectrum of as-synthesized LAS material.

### 5.2.3 Treatment of LAS in acid

It is known that some alkali silicates have a considerable solubility in water, hydrolyzing to silicic acids and basic solutions.<sup>10</sup> Silicic acids exist in the forms of orthosilicic acid ( $\text{H}_4\text{SiO}_4$ ), pyrosilicic acid ( $\text{H}_6\text{Si}_2\text{O}_7$ ), metasilicic acid ( $\text{H}_2\text{SiO}_3$ ), disilicic acid ( $\text{H}_2\text{Si}_2\text{O}_5$ ), *etc.*, and readily decompose to form polymeric silica gel. In order to obtain pure hexagonal spodumene, the as-synthesized LAS material was treated with a strong acid, in the hope that the strong acid will produce the weak silicic acid, and the resulting silicic acid/silica gel may be therefore removed by filtration or centrifugation.

The treatment was carried out using the following procedures. The as-synthesized LAS material (50 mg) was stirred in 20 mL concentrated HCl solution at RT for three hours. After stirring, the mixture was centrifuged at 3000 rpm for 20 min, and the solid was separated by decanting the acid solution. This stir-centrifuge-decant process was repeated three times to assure the full removal of lithium silicates. The resulting solid was washed with DI water and acetone, dried in an oven overnight, and collected for the following characterizations.

The acid-treated material (LAS-HCl) was analyzed by X-ray diffraction. As shown in Figure 5-14, no peaks from either  $\text{Li}_2\text{SiO}_3$  or  $\text{Li}_4\text{SiO}_4$  can be found after the acid treatment, proving HCl is effective in removing lithium silicates. All the peaks in the XRD pattern can be assigned to hexagonal spodumene. Rietveld refinement of the XRD pattern was performed using PDXL software as compared with hexagonal spodumene (JCPDS card 01-073-2336). A good fit was observed with a  $R_{\text{wp}}$  value of 8.61%. A halo peak at  $20 - 30^\circ$  can be observed from the XRD pattern, which is possibly due to either the unreacted Al-SBA-15 or the amorphous silica gel formed through decomposition of silicic acids.

Because this halo peak is absent in the as-synthesized LAS material (Figure 5-4), the broad amorphous peak in LAS-HCl more likely comes from the silica gel.

The acid-treated material was also analyzed by nitrogen sorption, SAXS, and TEM. Figure 5-15 shows that the material is mesoporous after the acid treatment, with the BJH pore size still at ~5 nm (Figure 5-16). However, the BET surface area increases from 85 m<sup>2</sup> g<sup>-1</sup> to 139 m<sup>2</sup> g<sup>-1</sup>. This increase in BET surface area is probably because the acid treatment removes lithium silicates. The SAXS pattern and the TEM image show that the acid-treated material has the same mesostructure as as-synthesized LAS material (Figure 5-17 and 5-18).

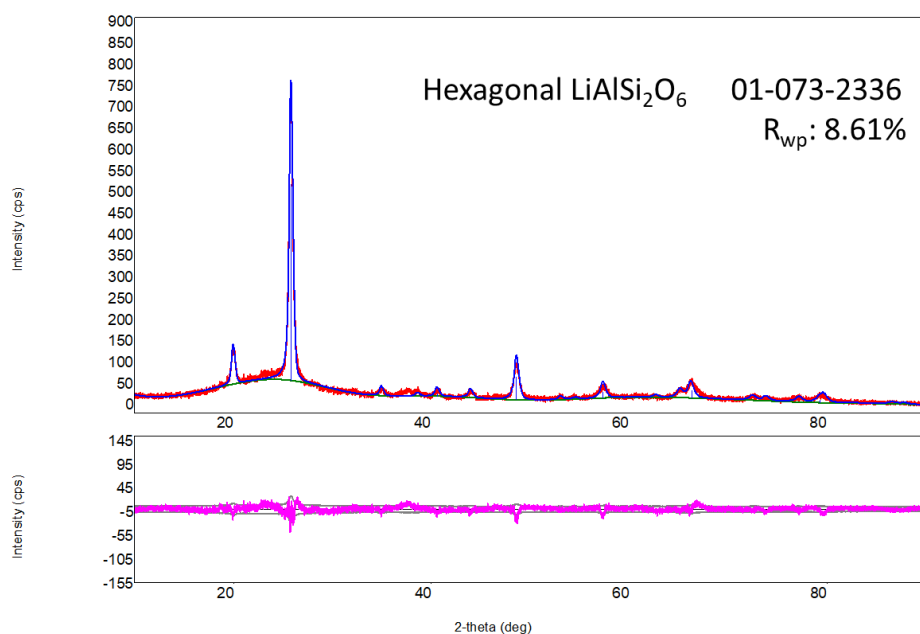


Figure 5-14. Rietveld refinement plot of LAS-HCl. The blue line is the original pattern; the red line is the calculated pattern using crystal information from JCPDS cards listed in the graph; the purple line in the lower box shows the errors. The R<sub>wp</sub> value for the refinement is shown in the upper right corner.

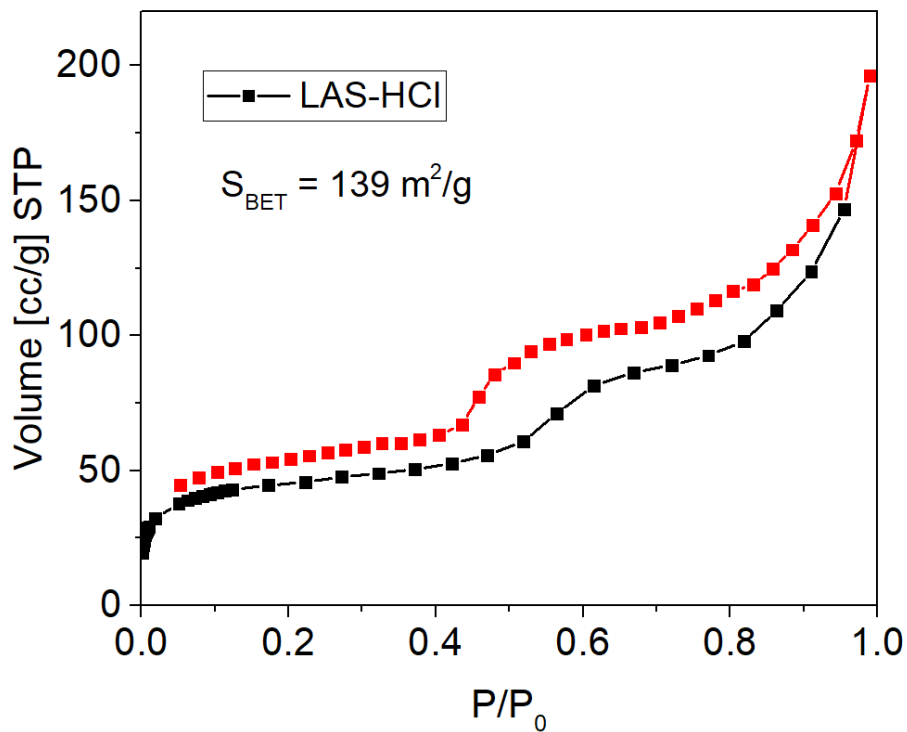


Figure 5-15. Nitrogen adsorption isotherm of the acid treated material, LAS-HCl.

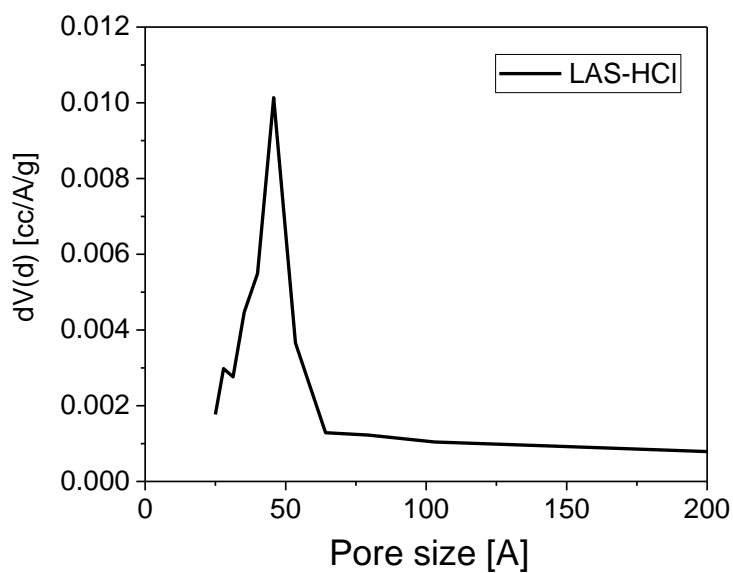


Figure 5-16. BJH pore size distribution of LAS-HCl calculated from the adsorption branch.

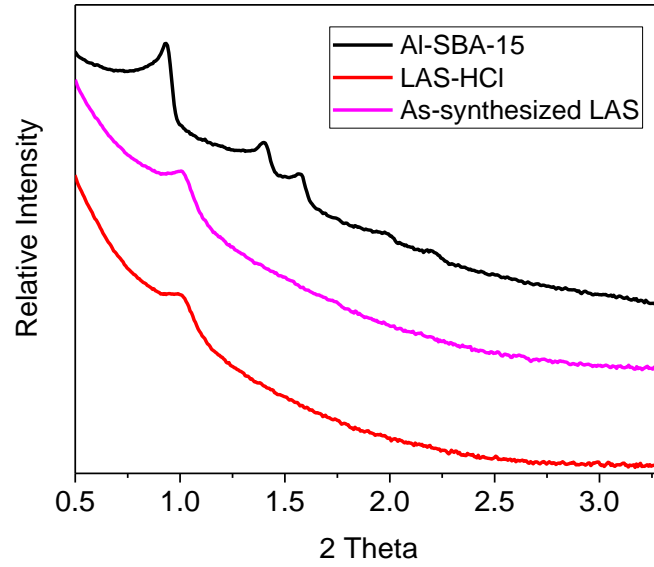


Figure 5-17. SAXS patterns of LAS-HCl as compared with Al-SBA-15 and as-synthesized LAS material.

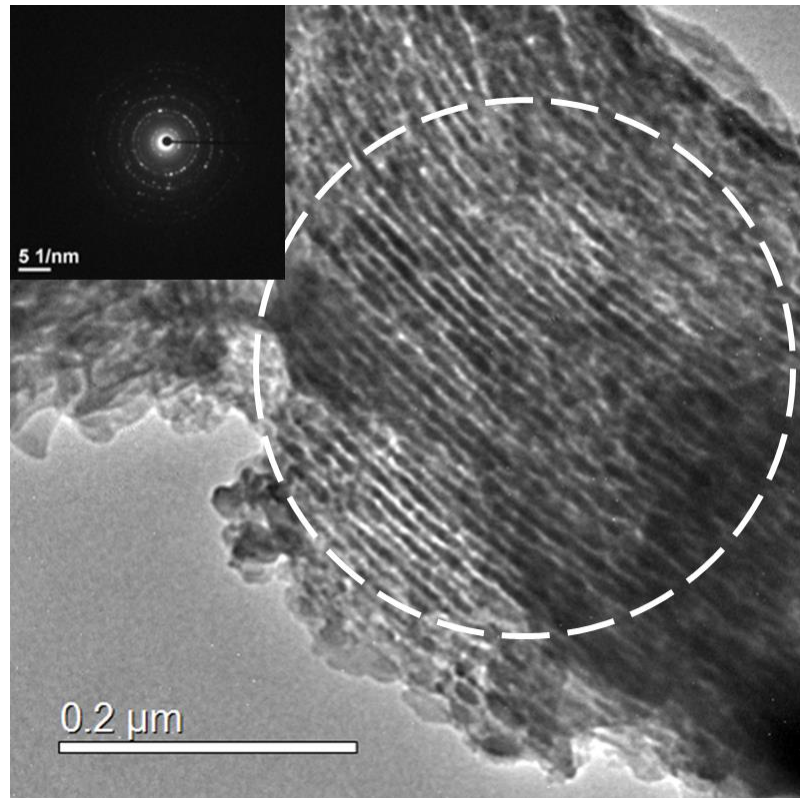


Figure 5-18. TEM image of LAS-HCl (inset shows corresponding SAED pattern collected from the encircled area).

The  $^{27}\text{Al}$  solid state NMR was also used to characterize the LAS-HCl material. As shown in Figure 5-19, after the acid wash, the relative amount of tetra-coordinated Al ( $\delta = \sim 60$  ppm) to hexa-coordinated Al ( $\delta = \sim 14$  ppm) ratio has decreased significantly, which is possibly due to dealumination in hexagonal spodumene caused by the strong hydrochloric acid. The Si/Al ratio of LAS-HCl was also determined by ICP-OES. Before acid treatment, the Si/Al mole ratio was 3.71:1. After the acid treatment, the Si/Al mole ratio in LAS-HCl decreased to 2.47:1. A smaller Si/Al ratio means that HCl did remove lithium silicates. However, it is still greater than the Si/Al ratio for pure hexagonal spodumene which is 2:1. This could be caused by either the existence of additional silica gel or dealumination. Taking both the  $^{27}\text{Al}$  solid state NMR spectrum and ICP-OES data into consideration, it is plausible to conclude that HCl has selectively removed tetracoordinated Al from the pore surfaces of hexagonal spodumene.

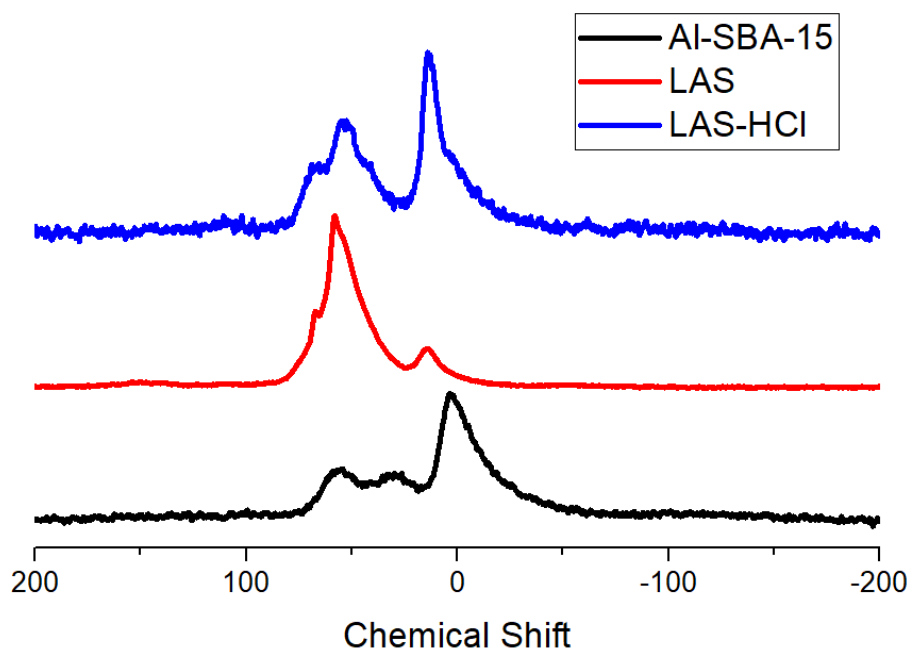


Figure 5-19.  $^{27}\text{Al}$  solid state NMR spectra of LAS-HCl in comparison with Al-SBA-15 and as-synthesized LAS.



Treatment of as-synthesized LAS material with concentrated sulfuric acid was carried out at 300 °C. The nitrogen sorption isotherm and TEM image show that sulfuric acid destroyed the mesoporous structure almost completely at this temperature. LAS-H<sub>2</sub>SO<sub>4</sub> material shows a Si/Al mole ratio of 10.98:1 by ICP-OES analysis, which shows a strong dealumination effect caused by sulfuric acid.

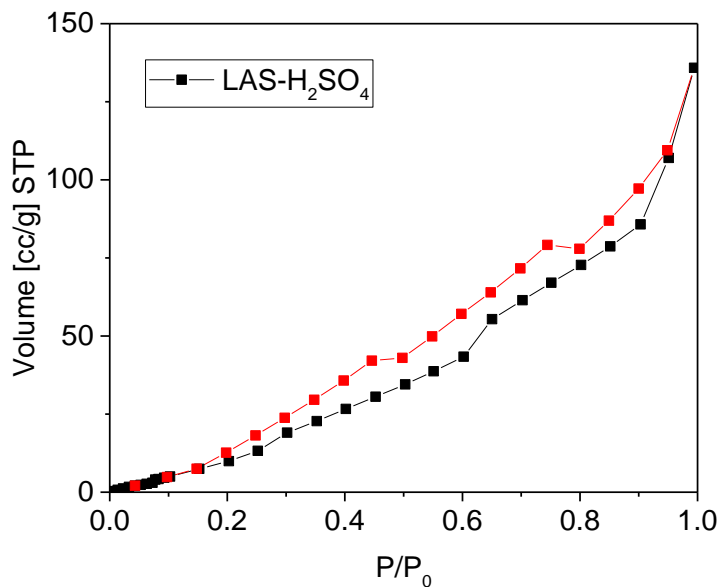


Figure 5-20. Nitrogen adsorption isotherm of LAS-H<sub>2</sub>SO<sub>4</sub>.

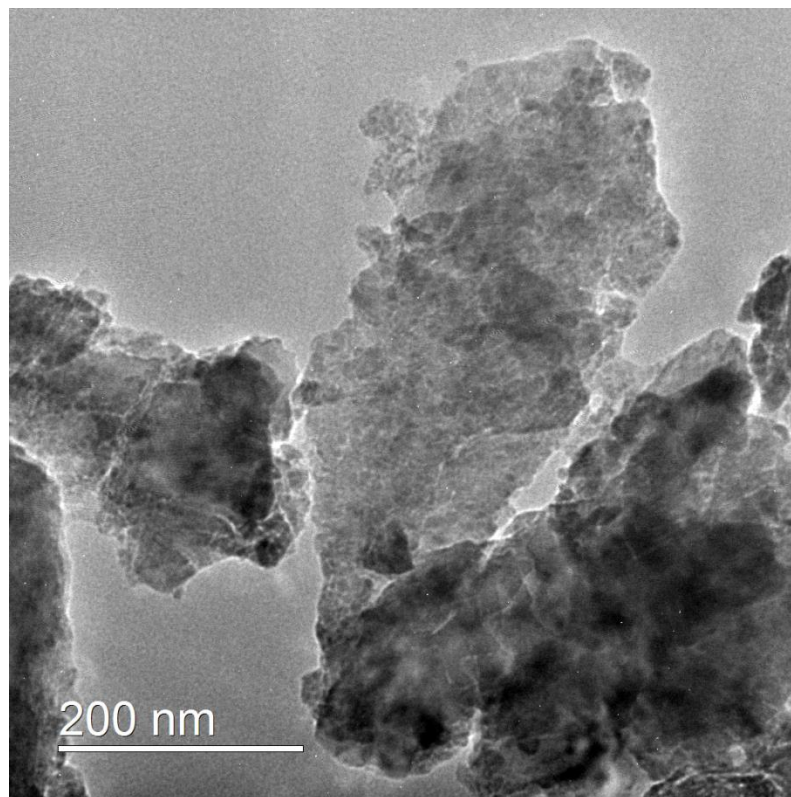


Figure 5-21. TEM image of LAS-H<sub>2</sub>SO<sub>4</sub>.

#### 5.2.4 Acidity study of LAS material

In order to investigate the acidity in the LAS material, the following ion exchange experiments were conducted on the as-synthesized LAS material. The as-synthesized LAS material (30 mg) was ion exchanged at RT (6 h) three times in 30 mL 1M aqueous solution of NH<sub>4</sub>Cl. The obtained LAS-NH<sub>4</sub> sample was dried at room temperature (RT) for 48 h and was then kept in a sealed container. Later this material was characterized by IR using temperature-programmed desorption (TPD) of ammonia.

Dehydration of LAS-NH<sub>4</sub> was carried out using the following procedures. LAS-NH<sub>4</sub> material was loaded into the Harrick Cell, 10 % O<sub>2</sub>/Ar was flowed through the cell at a rate of 30 mL min<sup>-1</sup>. The sample was then heated to 400 °C at 10 °C min<sup>-1</sup>, and maintained at

400 °C for 1 hr under flowing 10% O<sub>2</sub>/Ar. Subsequently, the sample was cooled to 115 °C under flowing 10 % O<sub>2</sub>/Ar. Ammonia TPD was then conducted using the following procedures. After the temperature of the dehydrated sample stabilized at 115 °C, the flowing 10% O<sub>2</sub>/Ar was turned off, and replaced by flowing Ar (30 mL min<sup>-1</sup>; 15 min). Subsequently, the Ar flow was stopped, and replaced by flowing 2000 ppm NH<sub>3</sub>/He (30 mL min<sup>-1</sup>; 30 min). At the end of this time, the NH<sub>3</sub>/He flow was shut off and replaced by flowing Ar (30 mL min<sup>-1</sup>; 15 min at 115 °C). With continued Ar flow (30 mL min<sup>-1</sup>), the temperature of the cell was increased to 150 °C, and an IR spectrum recorded. If needed, the temperature of the cell was again increased by 50°C and an IR spectrum recorded. This procedure was repeated until no changes in successive IR spectra were observed (maximum temperature = 450 °C).

Figure 5-22 shows the FTIR spectra collected during the above steps. The obtained LAS-NH<sub>4</sub> at ambient conditions (black curve) before dehydration shows a weak peak at 3750 cm<sup>-1</sup> which represents non-acidic terminal silanol groups,<sup>11</sup> a broad peak at about 3500 cm<sup>-1</sup> corresponds to adsorbed hydrates, and the ~1620 cm<sup>-1</sup> peak which is associated with NH<sub>4</sub> ions attached on Lewis acid sites.<sup>12</sup> After dehydration (red curve), the peak at ~1620 cm<sup>-1</sup> disappeared, showing the desorption of NH<sub>3</sub> by oxidative heating. The peak at 3750 cm<sup>-1</sup> became relatively stronger due to the dehydration. However, no peak at ~3610 cm<sup>-1</sup> was observed,<sup>11,13</sup> indicating that the acidic hydroxyl groups that bridge Si and Al framework atoms either does not exist in this material or is invisible using the FTIR technique (or the peak is below detection threshold). Later, after the adsorption of ammonia for 30 min (blue curve), the peak at ~1620 cm<sup>-1</sup> became larger, showing the adsorption of NH<sub>3</sub> by Lewis acid sites. Still, no peak at ~1550 cm<sup>-1</sup> shows the absence of Brønsted acid

sites.<sup>14</sup> The FTIR spectra of the material after the Argon flush for 15 min (pink curve) and the desorption at 150 °C (green curve) are almost the same as the blue curve, therefore the TPD was stopped at this stage because there is no sign of ammonia adsorption or desorption on Brønsted acid sites.

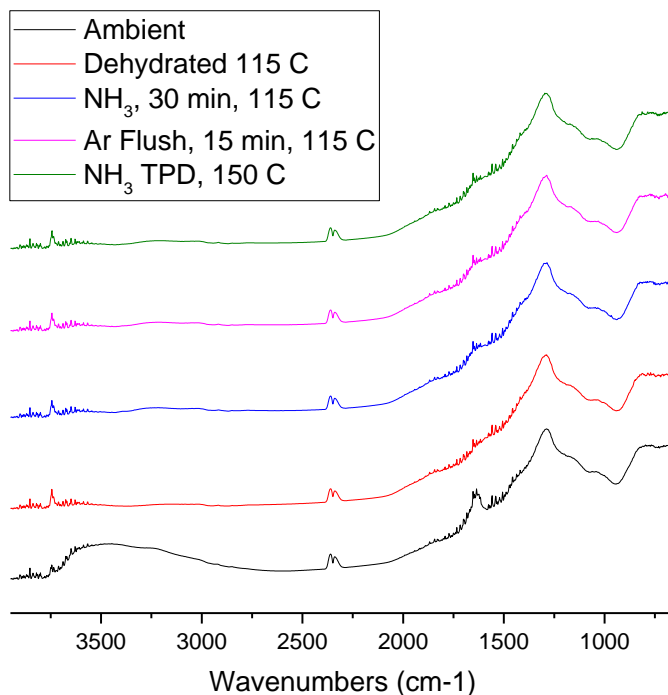


Figure 5-22. Ammonia TPD of LAS-NH<sub>4</sub>.

The ammonia TPD experiment indicates that no Brønsted acid sites are available in the LAS material. In order to examine if ion exchange can be realized for the as-synthesized LAS material, the following procedures were carried out in NaCl solution. As-synthesized LAS (30 mg) was ion exchanged at RT (6 h) three times in 30 mL 1M aqueous solution of NaCl followed by thoroughly wash with 20 mL x 3 DI H<sub>2</sub>O. The obtained LAS-Na sample was dried in an oven at 100 °C. EDS spectrum of LAS-Na is showing in Figure 5-23. A small signal of Na can be seen in the EDS spectrum, indicating the Na ion exchange was

successful. However, the small signal also means that only a very limited amount of Li was exchanged by Na. This phenomenon is probably due to the small surface area of the LAS material. Lithium ions in the bulk walls may not be very easily exchanged by another ion, and only the Li ions on the inner pore surfaces can be exchanged. This result also confirms the surface  $\text{AlO}_4$  moieties on the pores. Therefore, that the  $\text{NH}_4^+$  signal was not seen in FTIR spectra could be due to the small amount of surface  $\text{AlO}_4$  species and the low sensitivity of the FTIR technique.

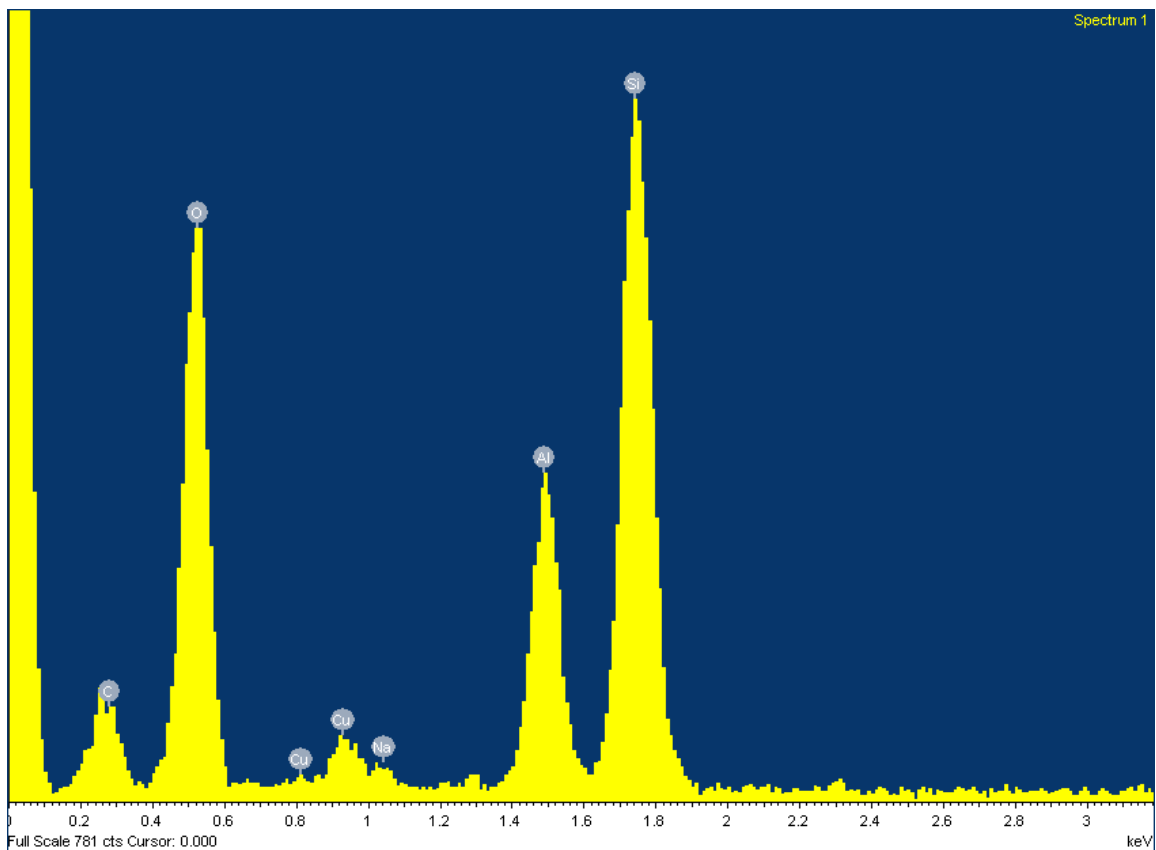


Figure 5-23. EDS spectrum of LAS-Na.

### 5.3 Conclusions

It is well demonstrated that a mesoporous lithium aluminosilicate material with crystalline pore channel walls was successfully synthesized by the flux-grown technique. This study presents the first example of a mesoporous hexagonal spodumene. The material was characterized by SAXS, nitrogen sorption, TEM to confirm its mesoporosity. The mesostructure was well retained because the pore channel walls were reinforced by carbon support.  $^{29}\text{Si}$  and  $^{27}\text{Al}$  solid state NMR spectra assured the tetra-coordinated forms of Si and Al.

The fabrication of crystalline mesoporous aluminosilica is of great scientific importance because of its potential catalytic properties to replace zeolites for long chain hydrocarbon cracking. With  $\text{AlO}_4$  moieties in the lithium aluminosilicate material, ion exchange of lithium ions by  $\text{NH}_4^+$  ions was conducted with the hope that heat treatment of  $\text{NH}_4$  replaced LAS material could create bridging OH groups on the pore surfaces. However, no bridging OH functional groups were found in the FTIR spectrum. The subsequent ammonia TPD also showed no ammonia was adsorbed to Brønsted acid sites. The Na exchange experiment proves the successful ion exchange by Na ions, but also indicates that only a small amount of surface Li ion could be exchanged. This result suggests that  $\text{NH}_4$  exchange is not visible in the FTIR spectra possibly because the amount of bridging OH is below the detection limit for FTIR. Even though the Brønsted acid sites are not detectable by FTIR, these acid sites may still be useful in catalytic processes. In the future, isomerization or hydrocarbon cracking experiments might be performed using thermally treated LAS- $\text{NH}_4$  to investigate its catalytic properties.

The flux-grown technique has proven its effectiveness in inducing the crystallization of amorphous aluminosilica. Compared with nanocasting at high pressure and high temperature, the flux-grown technique is more promising in producing lithium aluminosilicate in larger quantities. This method could also be extended to a general and flexible synthetic route for other mesoporous materials. Different mesoporous structures may have different reaction pathways which is also worthwhile for investigation.

## 5.4 References

- 1 C. T. Kresge, M. E. Leonowicz, W. J. Roth, J. C. Vartuli and J. S. Beck, *Nature*, 1992, **359**, 710–712.
- 2 T. Matsuno, Y. Kuroda, M. Kitahara, A. Shimojima, H. Wada and K. Kuroda, *Angew. Chemie - Int. Ed.*, 2016, **55**, 6008–6012.
- 3 S. Wu, Y. Han, Y. C. Zou, J. W. Song, L. Zhao, Y. Di, S. Z. Liu and F. S. Xiao, *Chem. Mater.*, 2004, **16**, 486–492.
- 4 M. Mandal, A. S. Manchanda, C. Liu, Y. Fei and K. Landskron, *RSC Adv.*, 2016, **6**, 7396–7402.
- 5 C. Bischoff, H. Eckert, E. Apel, V. M. Rheinberger and W. Höland, *Phys. Chem. Chem. Phys.*, 2011, **13**, 4540.
- 6 M. Takahashi, H. Toyuki, M. Tatsumisago and T. Minami, *Solid State Ionics*, 1996, **86–88**, 535–538.
- 7 C. T. Li, *Zeitschrift für Krist.*, 1968, **127**, 327–348.
- 8 A. Nordmann, Y. Cheng, T. J. Bastow and A. J. Hill, *J. Phys. Condens. Matter*, 1995, **7**, 3115–3128.
- 9 A. M. Welsch, D. Murawski, M. Prekajski, P. Vulic and A. Kremenovic, *Phys. Chem. Miner.*, 2015, **42**, 413–420.
- 10 R. C. Merrill, *J. Chem. Educ.*, 1947, **24**, 262.
- 11 V. L. Zholobenko, M. A. Makarova and J. Dwyer, *J. Phys. Chem.*, 1993, **97**, 5962–5964.
- 12 J. Datka, B. Gil and A. Kubacka, *Zeolites*, 1995, **15**, 501–506.
- 13 N. Cherkasov, T. Vazhnova and D. B. Lukyanov, *Vib. Spectrosc.*, 2016, **83**, 170–179.
- 14 W. N. P. van der Graaff, C. H. L. Tempelman, E. A. Pidko and E. J. M. Hensen, *Catal. Sci. Technol.*, 2017, **7**, 3151–3162.

## VITA

Yiqun Liu was born in China. In 2007, he attended the University of Science and Technology of China (USTC), where he earned a B.S. in materials science. After graduating from USTC, he joined Lehigh University to pursue his Ph.D. degree in chemistry in 2011. He currently focuses on the syntheses and applications of new porous materials.